Computational Digital Inline Holography for *In Situ* Particle Tracking and Characterization

A THESIS
SUBMITTED TO THE FACULTY OF THE GRADUATE SCHOOL
OF THE UNIVERSITY OF MINNESOTA
BY

Kevin Mallery

IN PARTIAL FULFILLMENT OF THE REQUIREMENTS
FOR THE DEGREE OF
PhD

Jiarong Hong

May, 2020

Acknowledgements

There are many people to whom I am indebted for their help and support during my time in graduate school. First, I would like to thank my advisor Professor Jiarong Hong for his support of my academic interests. I am appreciative of both the freedom he gave me to explore tangential methods and projects (some of which are now key elements of this thesis) as well as the pressure he applied to actually accomplish our stated goals.

I have been lucky to participate in a great deal of highly collaborative research with Prof. Nikolaos Papanikolopoulos, Prof. Miki Hondzo, and their students Dario Canelon and Jiaqi You. It was only with their assistance and leadership that the applications in the later half of this thesis were made possible.

Thank you to my lab mates, old and new. Mostafa and David, you helped me find my legs in this lab and laid the groundwork for my research. Santosh and Siyao, you were friends, collaborators, and sounding boards. Our frequent brainstorming sessions proved invaluable.

Finally, I am deeply grateful for my non-work friends and family for keeping me grounded throughout this. Katie and Dan, our game nights, even remotely, provided welcome relief from the stress of thesis work. Jeanette, you're the best. Thank you all.

Abstract

Digital inline holography (DIH) is a powerful single-camera 3D microscopic imaging tool that is able to digitally refocus a recorded image to reconstruct the 3D field of view. Compared to other single-camera techniques, DIH has a much larger depth of field in which objects can be seen, leading to drastically increased sampling volumes. Many particle features can be measured with DIH including size, shape, refractive index, identity, and motion. However, DIH has traditionally been limited by challenges related to the difficulty of accurately and quickly processing holographic images.

In this thesis, I present technical developments focused on the digital processing of holographic images that are intended to alleviate these challenges and enable the application of DIH to new measurements. Specifically, a new approach for hologram reconstruction – regularized holographic volume reconstruction (RIHVR) – is introduced. This method is able to produce substantially noise-free reconstructions of particle fields. A data-driven approach to predictive particle tracking is also introduced in order to enable increased particle concentrations for particle tracking velocimetry applications. Each of these developments is validated using synthetic data and experimental demonstrations.

Three applications of holographic imaging are presented to demonstrate the broad applicability of the method. The effect of temperature on the density of colonial cyanobacteria is identified by measuring the buoyant velocity and size of individual colonies. This could lead to better modelling of toxic algal blooms. Another type of algae, *Dunaliella primolecta*, is useful and can be farmed for materials used in nutritional supplements, pharmaceuticals, and biodiesel. DIH is used to identify behavior signatures that could be used as indicators of optimal lipid production. This could enable optimal harvest timing leading to improved biodiesel yield. Finally, a low-cost miniature underwater holographic microscope was developed for *in situ* field applications. This microscope is paired with a robotic platform to enable autonomous exploration of lakes or other aquatic environments. Despite its handheld size, the sensor is able to perform real-time particle concentration measurements using a deep neural network.

The recorded images can also be used to identify the type of microorganisms found in the water.

Contents

List of Figures

Part I

Introduction

Chapter 1

Introduction

1.1 Motivation and Objectives

1.1.1 Applications of Particle Measurements

Particles are ubiquitous in fields as diverse as physics, chemical engineering, and environmental science where measurements may include particle tracking velocimetry (PTV), sizing, concentration measurements, and identification. These particles may be artificial flow tracers, water droplets in clouds [9], algae that form harmful algal blooms (HABs) or cause disease [10, 11], atmospheric particles like pollen and soot [12], bubbles, oil droplets [13], snowflakes [14], sediments [15], or particles exhaled during breathing [16], among many other applications. Often, the number density of these particles may be very small. For example, the disease giardiasis can be caused by the ingestion of as few as 10 cysts of the protozoan parasite *Giardia intestinalis* [17] while swimming, an activity during which the average child ingests as much as 37 mL of water [18]. Similarly, virus-laden aerosols emitted during normal breathing and speaking may be produced at concentrations less than 0.3 particles/mL [19], yet are still considered a viable transmission pathway for many diseases including COVID-19 [20]. Conversely, 3D PTV requires accurate localization and tracking of thousands of particles, with higher seeding densities leading to higher resolution of the resulting fluid flow measurements.

1.1.2 Thesis Objective and Overview

Digital inline holography (DIH) is a powerful 3D microscopic imaging tool capable of performing measurements in each of these application domains. The objective of this research is to develop and improve tools to computationally recover the 3D information encoded in a hologram. These computational methods are accelerated through the use of graphics processing hardware (GPUs) in order to enable DIH images to be processed in a reasonable time frame. Finally, the aforementioned technological developments enable several applications for dense PTV, behavioral quantification of microbe swimming patterns, and on-board *in situ* measurements using a robotic platform.

1.2 Existing Methods

Three-dimensional (3D) microscopy is a field dominated by complex, expensive solutions such as tomography [21], scanning fluorescent microscopy [22], and other similar methods [23]. For most applications, there are specialized techniques used to perform the necessary measurements. DIH is unique in that it is can be generalized to multiple applications while improving upon the limitations of even specialized devices. The following sections summarize some common methods for three types of measurements.

1.2.1 Flow Measurements

Flow measurements are most often performed in laboratory settings but are also commonly used *in situ*. The scales of these measurements vary from many meters for atmospheric flows [24] to microscopic scales for turbulence dissipation, swimming microorganisms, or microfluidics [25]. As such, a wide variety of techniques are used.

Point measurements often use hotwire anemometry due to its high temporal frequency. However, the hotwire probe is invasive and risks flow disturbance – especially for near-wall flows. Laser Doppler velocimetry (LDV) is a non-invasive optical method utilizing the Doppler effect to measure the velocity of particle-laden flows. Sonic anemometers use variations in the time-of-flight for acoustic signals caused by bulk fluid motion. While simple, cheap, and fast, each of these methods are fundamentally point measurements while the true flow field is highly three-dimensional except in special

cases. Physical scanning of the sensor is often needed to measure time-averaged flow features needed for many engineering applications.

Particle image velocimetry (PIV) [26] is an extremely popular technique for measuring 2D velocity fields. PIV uses a light sheet (usually generated by a high-power laser) to illuminate particles in a single 2D plane of the flow. The displacement of a cluster of particles is determined using cross-correlation. Usually, an interrogation window of 32×32 pixels is used for this correlation with the inherent assumption that the window includes several particles and that those particles have the same velocity. Because of this, PIV smooths regions of high gradients. It also cannot be used in cases where particle clusters exhibit coherent motion such as when the seeding density is low or the particles behave independent of the flow. Nevertheless, PIV can be used at a broad range of flow scales, from microns to over 100 meters.

Particle tracking velocimetry (PTV) is closely related to PIV but tracks individual particles rather than clusters of particles, utilizing a Lagrangian viewpoint while PIV uses an Eulerian viewpoint [27, 28]. Because PTV individually tracks multiple objects within the PIV window size, it can achieve higher spatial resolution than PIV and can be used to measure flows with high gradients. PTV processing is usually broken into two steps: detecting the particles in the recorded images and linking the detected positions in time. Because these two steps are independent, multiple different techniques can be used to record the particle positions (including DIH). This flexibility allows the application of PTV to disciplines other than fluid dynamics including animal studies and microbiology where the objects will not exhibit coherent motion [29, 30]. PTV can also be applied for volumetric measurements. Common approaches for 3D PTV are tomography, defocusing PTV, V3V, and DIH-PTV. Tomography and V3V each require multiple cameras while DIH-PTV and defocussing PTV only require one. A special case of tomographic PTV is the shake-the-box (STB) algorithm [31] which combines the particle detection and tracking steps to improve the accuracy of each.

1.2.2 particle sizing

Methods for particle sizing include interferometric Mie imaging (IMI) [32], laser diffraction (LD), phase Doppler particle analysis (PDPA) [33], and aerodynamic particle sizers (APS) [34]. A fundamental challenge of these methods is that they assume the particles

are spherical, which is only valid for small particles. APS in particular requires sampling the particles and passing them through a nozzle in order to measure their aerodynamic properties and infer their size. This process risks disturbing the particle distribution and does not account for evaporation that may occur during the process.

1.2.3 *In situ* Measurements

Many of the above approaches can be applied to *in situ* measurements of fluid flows or particle size. However, the use of these methods for *in situ* measurements is limited by mechanical complexity and the need for multiple cameras. *In situ* applications often also require the identification of the particles to detect harmful microbes or distinguish oil droplets from air bubbles.

Specifically for lacustrine and marine particulates, current methods are unable to measure across a wide range of length scales, are restricted to small regions of the environment, often cannot differentiate between similar classes of particles, or may not have the sensitivity required for early detection. There are often trade-offs requiring the synthesis of data collected with multiple techniques in order to obtain conclusive results. Remote sensing [35, 36] is suitable for large-scale mapping of dense concentrations but has limited spatial and temporal resolution, poor sensitivity, and cannot penetrate deep below the surface. Fluorometers are often used to measure chemical components such as chlorophyll and phycocyanin which are used as proxies for biomass concentration [37]. However, these measurements are insufficient for identifying individual species and are highly dependent on the quality of their calibration. Physical sampling for laboratory analysis is still the gold standard measurement technique but is expensive, time consuming, and often infrequent.

1.3 Digital Inline Holography (DIH)

1.3.1 Fundamentals of operation

Digital inline holography (DIH) is a diffractive imaging method in which volumetric information – such as particle location, morphology, and refractive index – is encoded and subsequently extracted from a single 2D image [38]. The principle of DIH is that an

object illuminated by a coherent monochromatic light source (the primary or reference wave) emits a secondary spherical wave (the object wave) which interferes with the primary wave. Recording this interference pattern captures both the intensity and phase of the secondary wave which implicitly stores the information needed to reconstruct the 3D sampling volume through which the light propagated. This reconstruction can be treated as a refocussing of the recorded image, although the in-focus image contains information about the object refractive index and scattering properties that is not available with conventional microscopic imaging. The ability to resolve the position of objects in 3D naturally leads to tracking of the object over multiple video frames for 3D velocimetry [1, 39].

DIH has several advantages over the traditional approaches discussed in Section 1.2. The most significant characteristic of DIH is that it is a single-camera technique. This is particularly useful for PTV (collectively, DIH-PTV) which is able to capture time-resolved, volumetric three-dimensional three-component (3D-3C) velocities while using a single camera. This is in direct contrast to other single-camera methods such as microscopic particle image velocimetry (micro-PIV) which capture two velocity components in a 2D slice of the volume and other 3D-3C methods such as tomographic PTV which require at least three cameras. The use of a single camera and optical path provides for easier imaging of small-scale flows, especially in cases where optical access may be restricted. Additionally, the reported velocity resolution of DIH-PTV is generally greater than other methods [40]. The use of a single camera makes DIH-PTV substantially cheaper than tomography and other multi-camera methods which require additional expensive cameras. The use of the efficient forward-scattered light signal reduces requirements on laser power (and cost) compared to PIV which images the much weaker side-scattered light. The low cost and hardware simplicity of DIH has enabled multiple in situ applications [41, 42, 43]. DIH is also an imaging method with an extremely large depth of focus. This enables direct morphological measurement or species identification of sparse species. The non-invasive nature of DIH prevents flow disturbance and ensures the validity of *in situ* measurements.

1.3.2 Historical Background

Holography was first introduced in the Nobel prize-winning work of Dennis Gabor in 1948 [44]. The Gabor approach utilizes a coherent source that illuminates an object, producing a secondary scattered wave. The unscattered primary wave interferes with the secondary object on the sensor plane (traditionally a photographic plate). Interestingly, this work predates the invention of the laser by over a decade and used a diverging electron beam as the coherent source.

The Gabor method is now known as inline holography to distinguish it from off-axis holography in which a separate reference wave, inclined at an angle relative to the object wave, is used to produce the interference pattern (see Fig. 1.1 and Fig. 1.2). Compared to inline holograms, those taken with an off-axis system have a higher signal to noise ratio, in part because the reference beam is not contaminated by the sample and because the twin image (figure 1.4) is not formed. However, an off-axis holographic system requires several additional components (beam splitters, mirrors) that increase the cost and size of the sensor. Additionally, reconstructing an off-axis hologram requires precise knowledge of the angle of the reference beam and precise alignment of the system. In contrast, an inline holographic system requires relatively few components and the angle of the reference wave is implicit.

Early methods such as the one used by Gabor captured the interference pattern using photographic film and performed the reconstruction optically by illuminating the recorded film with the reference beam to produce an image that appears to be three dimensional when viewed by a human or conventional camera. The first applications of holographic PTV were performed with these chemical plates and optical reconstruction [45, 46, 47]. These systems required complex optical, mechanical, and chemical equipment in order to record and reconstruct the holograms with a labor-intensive process. Starting in 1994, digital cameras started replacing chemical film, with numerical processing used for the reconstruction [48]. As digital sensors and processors have improved, faster automated processing methods using computer vision and machine learning techniques can be used to extract more of the information encoded in the recorded hologram. However, the resolution of a digital hologram may be limited by the physical pixel size of the camera sensor while film holograms are diffraction limited. The pixel size of modern sensors is often smaller than the diffraction limit when magnification is used,

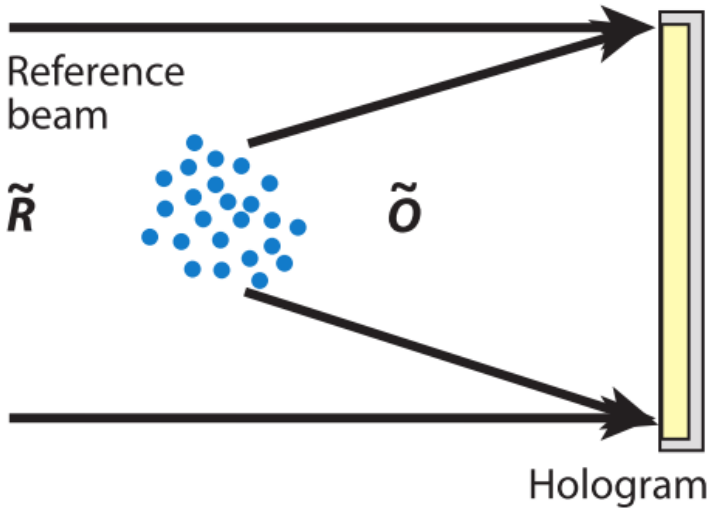

Figure 1.1: Mechanism of formation for inline holograms. Image credit: Katz & Sheng [1]

making this discretization error less important.

1.3.3 Applications

As previously discussed, DIH can and has been applied to each of the measurement categories discussed in Section 1.2. A brief summary of some of these applications follows in order to provide a better appreciation of DIH capabilities. A review of many of these applications has been published by Yu et al. [39].

Applications within the field of fluid mechanics include measurements of 3D flow fields [49], particle dynamics [50], microorganism swimming [51], and flow-structure interaction [52, 53]. Recent years have seen the increased application of DIH-PTV for various flow measurement applications where traditional methods are inadequate. Singh and Panigrahi [54] performed whole-field measurement of the 3D-3C velocity field for liquid slug Taylor flow, visualizing 3D recirculation bubbles. High-resolution velocimetry of boundary layer flow over super hydrophilic surfaces was performed with DIH-PTV by Ling and others [55]. Similarly, the boundary layer impact of roughness elements was measured by Toloui et al. [40] over a large ($5 \times 5 \times 5$ cm^3) field of view using whole-field

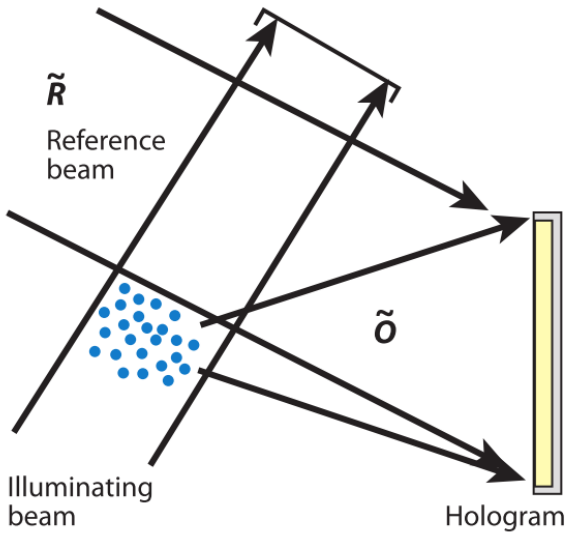

Figure 1.2: Mechanism of formation for off-axis holograms. Image credit: Katz & Sheng [1]

seeding. A full review of DIH applications to fluid mechanics is presented by Katz & Sheng [1].

Holography has been applied to *in situ* measurements for a variety of research fields including cloud formation [56], sediment physics [15], air quality monitoring [57], and fruit fly behavior [58]. Beals et al [56] measured the size and spatial distributions of water droplets in clouds, showing that the particle mixing is inhomogeneous. This discovery can be applied to weather and climate models of clouds to improve prediction accuracy. They used an inline system (Fig. 1.3a) with turning prisms to avoid flow disturbance and a large lens assembly to get a large field of view, high-resolution image [2]. Talapatra et al [3] measured the size and spatial distributions of microorganisms in a 15 m water column using a dual inline system (Fig. 1.3b) which simultaneously recorded the same volume at two resolutions and frame rates. They documented the presence of a thin layer of highly concentrated particles as well as preferential alignment of particles which can be used to model the formation of harmful algal blooms that cause millions of dollars in damage to the US economy each year. A deep sea holographic microscope described by Rotermund et al [4] and sold commercially by 4Deep Inwater Imaging

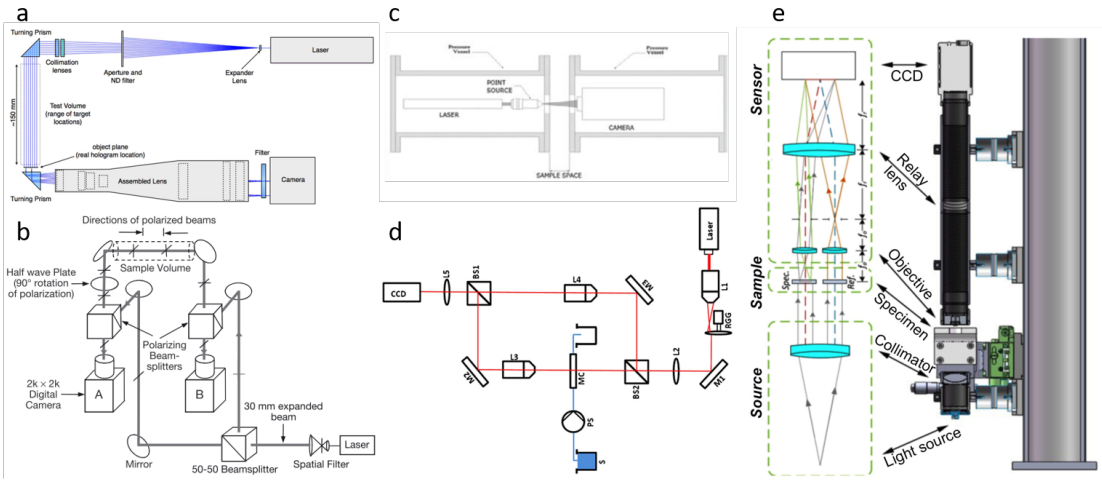

Figure 1.3: Examples of holographic systems. a) [2] b) [3] c) [4] d) [5] e) [6]

uses an inline system (Fig. 1.3c) with a spherical reference wave and is capable of identifying microorganisms at depths of up to 6000 m. The spherical wave has less background noise than a collimated wave but produces a reconstructed volume with variable resolution due to the expansion of the beam. El Mallahi et al. [5] were able to use holography to identify the parasite *Giardia lamblia* and differentiate it from similar organisms in a laboratory setting with applications to monitoring municipal water supplies. Their system (Fig. 1.3d) is designed for laboratory measurements and uses an inline setup with a separated reference beam that is not contaminated by the sample. Lindensmith et al. [6] built an off-axis holographic system (Fig. 1.3e) for detecting life in sea ice with the target of a similar system being used on extraterrestrial bodies such as Europa, Mars, and Ganymede. Atmospheric aerosols collected using a miniature 3D-printed impactor nozzle were imaged using a lensless holographic system by Wu et al. [57]. With the exception of the Rotermund and Wu systems, all of these use a large number of optical components in order to improve some aspect of the quality of the recorded holograms whether it be resolution (Beals and Talapatra) or background noise suppression (Rotermund, El Mallahi, and Lindensmith). The use of so many components for an *in situ* measurement device results in a large, expensive sensor.

In a laboratory setting, DIH has been used to examine microorganism behavior.

Chengala et al. showed that the unicellular organism *Dunaliella primolecta* preferentially aligns itself when in a flow with a high shear rate. [59] Molaei et al. found that the tumbling behavior of *Escherichia coli* was suppressed near a surface [51]. The detection and identification of potentially harmful aquatic microbes with a holographic flow cytometer has been demonstrated by numerous authors [5, 60, 61, 62]. Medical applications include red blood cell counting [63, 64, 65], sperm motility [66, 67], and cancer detection [68, 69, 70]. It is worth noting that the cancer and other medical imaging tasks are often not imaging particles, but rather thin slices of cells. In these cases, the low-cost nature and phase imaging capabilities of lensless holography are the primary benefits in comparison to traditional microscopy.

1.3.4 Detailed Operation

A comprehensive description of the mechanisms of digital hologram recording and reconstruction is necessary to understand the challenges facing holography and the computational methods used to improve performance. Applications can generally be conceptualized using the simplified refocusing description that has been used so far.

Any imaging sensor (digital or film) records the complex magnitude of the incident light. That is, $I_{rec} = \tilde{I}\tilde{I}^*$ where the tilde represents a complex value and the asterisk is complex conjugation. For holography, the incident light is the summation of the reference wave, $\tilde{R}$, and the object wave, $\tilde{O}$ [1].

$$I = (\tilde{R} + \tilde{O})(\tilde{R}^* + \tilde{O}^*) \tag{1.1}$$

Optical reconstruction of traditional film holograms is performed by illuminating the recorded image (I) with the reversed reference wave. Mathematically, this is equivalent to multiplying by the conjugate reference, $\tilde{R}^*$. The image viewed a distance z from the recording plane is the result of the product $\tilde{R}^* I$ diffracting through space. For digital holography, this is modeled as a convolution of the recorded hologram with an analytical expression for the diffraction from a point source, namely the Rayleigh-Sommerfeld or Kirchhoff-Fresnel kernels (equations 1.5 and 1.6 respectively). The convolution of two signals is defined as the integral of the multiplication of one signal with a shifted version of the other (equation 1.2).

$$g(x) = f(x) \otimes h(x) = \int_{-\infty}^{\infty} f(x)h(x-\xi)d\xi \tag{1.2}$$

An important property of convolution is that it is possible to eliminate the need to evaluate the convolution interval through the use of the convolution theorem which states that convolution in the spatial domain is equivalent to elementwise multiplication in the frequency (Fourier) domain and vice versa (equation 1.3).

$$G(\xi) = FT(g(x)) = F(\xi)H(\xi) \tag{1.3}$$

Therefore, hologram reconstruction can be performed in the Fourier space as follows for a discrete two dimensional image

$$G(m,n) = F(m,n)H(m,n) \tag{1.4}$$

Where H is either H_{RS}, the Rayleigh-Sommerfeld kernel, or the Kirchoff-Fresnel kernel H_{KF} which is a special case of the Rayleigh-Sommerfeld kernel when the object is far from the sensor (the paraxial approximation) [1, 38].

$$H_{RS}(m,n) = \exp\left(-j\frac{2\pi}{\lambda}z\sqrt{1-\lambda^2\left(\frac{m}{M\Delta x}\right)^2-\lambda^2\left(\frac{n}{N\Delta y}\right)^2}\right) \tag{1.5}$$

$$H_{KF}(m,n) = j\lambda\exp\left(j\lambda\pi z\left[\left(\frac{m}{M\Delta x}\right)^2+\left(\frac{n}{n\Delta y}\right)^2\right]\right) \tag{1.6}$$

Here λ is the wavelength of the illumination source, m and n are the discrete coordinates in the Fourier domain, M and N are the total number of elements, and s is the pixel size. It is important to note that all reconstructed planes of G will have both a real and imaginary component as it represents the object wave. The complex magnitude of G will give the intensity of the image as it would be captured with a camera.

1.3.5 Traditional Challenges of DIH

There are several challenges for DIH that can be summarizes as a loss of 3D information in the recorded hologram. As previously discussed, reconstruction of the recorded intensity image (I) is performed through multiplication with the conjugate reference wave ($\tilde{R}^*$). Expansion shows that the reconstructed wave is the sum of four components (Eq. 1.7).

$$\tilde{U}_r = \tilde{R}^*I = \tilde{R}^*(\tilde{R}+\tilde{O})(\tilde{R}^*+\tilde{O}^*) = |R|^2\tilde{R}^* + |R|^2\tilde{O}^* + \tilde{R}^*2\tilde{O} + R^*\tilde{O}\tilde{O}^* \tag{1.7}$$

The first component is a form of the illuminating wave, the second is the real image, the third the virtual or twin image, and the fourth is the cross-interference term. Critically, it is not possible to extricate the object wave $\tilde{O}$ from this expression, making a perfect reconstruction of the sample producing the object wave impossible. Compounding this problem, the true reference wave is often not known as it is contaminated by the optical components it passes through prior to reaching the sample volume such as collimating lenses, mirrors, and windows.

The loss of information can be generalized by stating that the signal to noise ratio (SNR) for holography is low. This produces several features which are sometimes described as separate problems afflicting DIH.

The Depth of Focus Problem

Since the inception of DIH-PTV, poor longitudinal (i.e., out of the plane of the image) resolution has consistently been the greatest challenge [1, 40]. Known as the depth-of-focus (DOF) problem, the apparent elongation of reconstructed particles is caused by the finite sensor extent and the intensity integration effect of physical pixels [1, 38]. Additional imaging noise further reduces the ability to resolve the critical high frequency fringes which are necessary for accurate depth reconstruction. Because of this limitation, some applications of DIH-PTV (namely [55, 40]) have primarily focused on the analysis of the much more accurate in-plane velocities.

The Twin Image Problem

Figure 1.4 illustrates the twin image problem where the reconstructed particle will appear to be in focus at two locations on opposite sides of the imaging plane [1]. This can cause ambiguity in reconstructing the object field unless the imaging plane is outside of the sample volume. The twin image is formed because only the intensity of the incident wave is recorded. The twin image is the third of the four terms in the expanded from of Eq. 1.7.

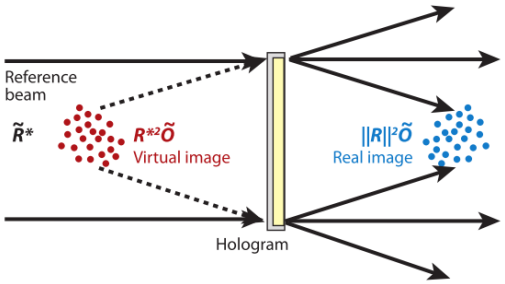

Figure 1.4: Demonstration of location of reconstructed virtual image. Image credit: Katz & Sheng [1]

Cross-Interference

Cross-interference, the fourth term in Eq. 1.7, results in further lost information. For single point-like particles or sparse concentrations this term can be ignored. However, it will be non-trivial for large objects or extremely dense particle fields. Because the emitted wave from a point-like particle is spherical, its signal is spread across the entire imaging sensor. Signals from multiple particles overlap and the ratio of their contributions is lost because only the intensity is recorded. Additionally, the light scattered by one object can be rescattered by a nearby object. This phenomenon is difficult to model but can be assumed to have very low intensity and can be treated as noise.

Particle Density Limitations

High particle density is critical for PTV applications. A high seeding density for PTV results in a high-resolution velocity field. However, when high particle concentrations are used, cross-interference and other noise sources (twin image, out-of-focus particles) result in a low signal-to-noise ratio (SNR) [71]. Malek et al. showed that the reconstruction quality depends on both the shadow density and the depth of the sample [71]. The shadow density is

$$s_d = n_s L d^2 \tag{1.8}$$

where n_s is particle number concentration, L is sample depth, and d is the particle diameter. Improving the particle density limit and the accuracy of dense particle field

measurements is one of the primary aims of this work.

Computational Cost

Another major challenge of holography is that the algorithms for reconstructing the 3D sample volume are computationally intensive. This challenge and its solutions will be discussed in more depth in Chapter 4.

Prior Solutions

Many approaches to overcoming the aforementioned drawbacks focus on hardware design to improve the recorded image quality or encode more information in the recording. The most common is the use of multiple viewing angles (tomographic DIH), using the lateral accuracy and some depth information from each view to more accurately localize the particles [72, 73, 74, 75]. This method requires only two cameras (or one by using mirrors [73]) compared to three or four required for conventional tomography. Other approaches specific to DIH-PTV seek to reduce the effective shadow density by illuminating only a limited volume of interest [76] or using localized particle seeding [77]. Allano et al. used a fiber-coupled diode to illuminate a narrow region of near-wall particles from within the flow in a wind tunnel [76]. Due to their mechanical and optical complexity, these methods are non-trivial to implement and care must be taken to avoid flow disturbance. Use of a hybrid side scatter inline approach enables directed illumination of a select region of the sample volume, reducing the number of particles which appear in the recorded image [78]. Off-axis holography is also commonly used as it does not have the twin image problem and separates the reference beam from the object (reducing contamination) [6, 79]. However, this requires precision alignment and higher laser coherence. Collectively, these methods negate the principle advantages of DIH-PTV – namely ease of use and hardware simplicity – by requiring multiple optical paths, viewing angles, and calibration thereof.

Many authors have focused on improving the numerical processing of DIH-PTV images. Much of this work has been focused on automatic detection of the object focal plane to address the DOF problem [80, 81]. These methods usually use a focus metric that is evaluated on each reconstructed plane and has an optimal value when the object is in focus. These metrics are reasonable for objects with little depth where

their position can be restricted to a plane However, these do not address the problem of low SNR and usually assume that accurate 2D segmentation is trivial which is only true when the particle concentration is very low. Focus metrics usually do not have sufficient accuracy for velocimetry or other applications where location accuracy is very important.

An inverse approach proposed by Soulez et al [82] avoids reconstructing the whole volume by posing particle detection as an optimization problem solved using a non-linear least squares fit to generate a synthetic hologram matching the signal of the recorded hologram. In order to reduce the scope of the optimization, it is necessary to assume a shape for the objects such as a small sphere. A similar iterative phase retrieval method has been shown to solve the twin image problem and improve the reconstructed SNR [83, 84], but has not been applied for PTV due to the dependence on *a priori* knowledge of the object depth.

Holographic deconvolution [85, 86, 87, 40] borrows a method from optical microscopy to treat the apparent blurring of point objects in the 3D reconstruction as convolution of the true object with a blurring point spread function (PSF). However, the dependence of deconvolution on a 3D Fourier transform makes this method memory intensive and windowing may be needed to process large holograms (more than 10^8 voxels). The point object assumption also limits the range of applications suitable for deconvolution.

Part II

Technical Development

Chapter 2

Regularized Inverse Hologram Volume Reconstruction (RIHVR)

The content of this chapter has been published by the author in Optics Express [88]. Content, including figures and text, has been duplicated with permission.

2.1 Introduction

A recent approach to holographic reconstruction is the inverse method [89, 90]. Inverse methods, rather than reconstructing the object from the image, instead find the optimal object that would produce the observed image while satisfying some physical constraints. Many inverse methods for iterative phase retrieval or super-resolution require multiple captured instances of the same object, often translated by a known amount [70]. These show great promise for holographic microscopy but are unsuitable for PTV due to their reliance on a static object. It is also worth noting that microscopic deconvolution can often be viewed as a type of simple inverse problem solution. However, this is not the case for holographic deconvolution which operates on the reconstructed volume rather than the recorded image.

One of the first inverse problem formulations was proposed by Soulez et al. [89] who performed a 4D parametric optimization to find the 3D location and radius of spherical particles. They first use a standard method for coarse localization and then independently optimize each particle parameter (e.g. location, size) to minimize the L2 error

over a restricted region. This method has been extended to detect particles outside the image field-of-view [82], utilize past locations to improve the initial parameter estimation [50], and improve the size and position resolution [91]. A similar approach uses a more complex Lorenz-Mie scattering model to localize colloidal particles as well as identify their refractive index [92, 93]. Both of these methods have a stated linear time dependence on the number of particles, making them unsuitable for fluid flow applications where thousands of particles must be tracked for hundreds of frames. Furthermore, the assumption of spherical particles restricts the scope of potential applications.

The use of the term "compressive holography" (CH) to refer to the inverse problem was introduced by Brady et al. in 2009 who borrowed concepts from the field of compressive sensing for holographic processing [90]. They used a total variation regularized approach to produce in-focus images of two dandelion seed parachutes recorded concurrently at two different focal planes. Denis et al. [94] used a similar approach with a simpler sparsity-based regularization. Both approaches show a significant reduction in the out-of-focus noise, twin images, and other noise. Recent work has used a set of physically meaningful constraints (including sparsity, smoothness, and non-amplification) in a unified parametric and CH framework to achieve excellent reconstructions of absorption and phase of individual evaporating particles and their evaporation tails [95, 96]. However, these methods operate on a limited number of planes and cannot reconstruct the 3D shape of complex objects.

Full inverse methods (without a spherical assumption) have only been used to reconstruct objects for which the axial location is known either *a priori* or from a conventional reconstruction method. There have been no prior applications of compressive holography for DIH-PTV of flows containing thousands of tracer particles. The primary barrier preventing such application is the high computational cost. A complete discussion of the approaches used to reduce the computational cost can be found in Chapter 4.

In this chapter, a summary of the fundamentals of CH is presented. I then introduce our recently published approach for Regularized Inverse Hologram Volume Reconcstruction (RIHVR, pronounced "river") [88]. RIHVR uses fused lasso regularization and a sparse storage structure to enable processing of very large images in a realistic time. Several synthetic and experimental evaluation cases are presented to demonstrate the quality and performance of RIHVR.

2.2 Methodology

The 3D reconstruction of the object volume is formulated as an inverse optimization problem, following the method of Brady, Endo, and others [90, 97]. The optimization problem formulation, Eq. (2.1), seeks to find the object field (x) that minimizes the difference between the observed hologram (b) and the estimated hologram produced by propagating the object to the imaging plane ($\hat{b} = Hx$). A regularization term $\lambda R(x) = g(x)$ is included in Eq. (2.1) to enforce physically realistic properties (principally sparsity and smoothness) and avoid trivial solutions. The size of the regularization parameter λ determines how strongly these properties are enforced. To ensure solution convergence, we use a linearized form of the forward model for hologram formation, Eq. (2.2), which implicitly treats any nonlinear terms (i.e., twin image and cross interference) as noise.

$$\hat{x} = \arg\min_{x} \left\{ \|Hx - b\|_2^2 + \lambda R(x) \equiv f(x) + g(x) \right\} \tag{2.1}$$

$$Hx = \Re \left(\frac{1}{N_z} \sum_{z=1}^{N_z} e^{jk_0 z} x_z * h_{-z} \right) \tag{2.2}$$

Here k_0 is the wavenumber, h_z is the Rayleigh-Sommerfeld diffraction kernel, and convolution is performed in the Fourier domain. The discrete Fourier domain representation of h_z is given by Eq. (2.3) [1] where m and n are the discrete coordinates, M and N are the total number of elements, and s is the pixel size.

$$FT\{h_z(x,y)\} = \mathcal{H}_z(m,n) = exp\left[-jk_0 z \sqrt{1 - \left(\frac{k_0 m}{2\pi M s} \right)^2 - \left(\frac{k_0 n}{2\pi N s} \right)^2} \right] \tag{2.3}$$

The only difference between forward propagation (hologram formation) and back-propagation (reconstruction) is the sign of the depth, z. Note that Eq. (2.2) models the object field as a series of discrete planes in z. The true object must fall on one or more of these planes in order to be correctly modeled.

We solve the inverse problem using FISTA (Fast Iterative Shrinkage-Thresholding Algorithm) [98] as implemented for FASTA [99]. This method is selected due to its high convergence rate, relative simplicity, and similarity to prior work [90, 97]. FISTA has two steps: a shrinkage step using the proximal operator (Eq. (2.4)) and an accelerated

update using the previous estimate (a simple element-wise operation not included here for brevity).

$$x_k = prox_{\lambda L}\left(x_{k-1} - L\nabla f(x_{k-1})\right) \tag{2.4}$$

In the context of holography, the gradient term $\nabla f(x_{k-1})$ is the reconstructed volume from the residual hologram $(\hat{b} - b)$. The scalar factor L is determined automatically using backtracking [98]. The proximal operator (Eq. (2.5)) can be interpreted as a gradient descent step with step size L [100]. The reader is referred to the references for further details on FISTA.

$$prox_L(v) = \arg\min_x \left(g(x) + \frac{1}{2L}\|x - v\|_2^2 \right) \approx v - L\nabla g(x) \tag{2.5}$$

The form of the regularization function $R(x)$ determines which properties of the solution will be enforced. The ℓ^1 norm (Eq. (2.6)) enforces a sparse solution (i.e., one with few non-zero elements) which for DIH-PTV means that the object volume fraction is low. This sparsity-based regularization has been demonstrated for holography by Denis et al. [94] and Endo et al. [97].

$$R(x) = \|x\|_1 = \sum_{i=1}^{N} |x_i| \tag{2.6}$$

The Total Variation (TV) norm (Eq. (2.7)) is the sum of the first-order gradients over the image (size $N_x \times N_y$). These gradients are computed using a circular boundary condition (i.e., $x_{0,0} = x_{N_x,N_y}$) which is valid when the image is zero-padded to ensure no objects are near the borders. TV regularization enforces a smooth solution (small gradients) and is naturally extensible to higher dimensions.

$$R(x) = \|x\|_{TV} = \sum_{i=1}^{N_x} \sum_{j=1}^{N_y} \sqrt{(x_{i,j} - x_{i-1,j})^2 + (x_{i,j} - x_{i,j-1})^2} \tag{2.7}$$

The TV approach has been used by Brady et al. [90] and Endo et al. [97] who demonstrate that it is superior to the ℓ^1 regularization for sufficiently large objects. The reason for this benefit is that the smooth solution enforced by the TV regularization results in reconstructed objects that are not over-segmented. However, we will see that TV regularization is substantially more computationally demanding that the ℓ^1 method.

We propose using the Fused Lasso (FL) regularization method (Eq. (2.8)) which is a combination of the TV and ℓ^1 norms ("fusion" and "lasso" being alternative terms for TV and ℓ^1 respectively) [101]. Solutions to the FL problem are both smooth and sparse while having some characteristics that make it less computationally demanding than TV.

$$g(x) = \lambda R(x) = \lambda_{\ell^1} \|x\|_1 + \lambda_{TV} \|x\|_{TV} \tag{2.8}$$

The shrinkage step of FISTA (Eq. (2.4)) is by far the most computationally complex and depends on the choice of $R(x)$. As such, the computational cost of FISTA is closely linked to that of evaluating the proximal operator. For the ℓ^1 regularizer, the proximal operator has a simple closed-form solution as soft thresholding:

$$prox_{\lambda L}(v) = \left(1 - \frac{\lambda L}{|v|}\right)_+ sign(v) \tag{2.9}$$

However, the proximal for the TV function does not have a closed-form solution and requires an iterative solution, for which we use the gradient projection method of Beck & Teboulle [102]. This method requires storage of each directional derivative for the duration of the iterations which may require a substantial amount of memory. The FL regularization function has the useful property that it is separable and can be computed by soft thresholding the solution to the TV problem (i.e., with $\lambda_{\ell^1} = 0$). Because the non-sparse TV solution must first be computed before soft thresholding to produce the sparse FL solution, high memory requirements of the TV proximal still apply within each FISTA step even though the result is sparse. We limit our TV regularization to 2D planes which can be computed independently, reducing the memory requirements to those of a single plane. It is worth noting that prior compressive holography methods using TV regularization have reported only the 2D variant.

Because FISTA is an iterative solution method, the computational time required to process a single image may be relatively high. PTV requires processing thousands of large, well-resolved volumes. Therefore, it is crucial to reduce the processing time to a manageable level to enable application to real flow studies. A detailed discussion of the CUDA/C++ GPU implementation of this algorithm is provided in Chapter 4.

The primary advantage of the compressive holography approach is that it produces very high SNR reconstructions that are more easily segmented for particle localization. In one sense, the sparsity regularization inherently separates objects (non-zero voxels)

from the background (zero voxels), negating the need for complex volume normalization and SNR enhancement such as that used by Toloui et al. [40]. While these directly thresholded results are reasonable, we have found that two additional filters greatly reduce the instances of over-segmentation. The first is a very low intensity threshold on the order of $1/256^{th}$ the maximum intensity of the image. This value is selected as any values below it are indistinguishable from zero when using a min-max scaling and 8 bit discretization for visualization. The second filter is a minimum object volume. This must be adjusted slightly depending on the size of the particles, noise level, and apparent elongation length. At this time, it is not directly linked to the true particle volume. Usually, objects of 5 voxels or fewer are treated as noise. While crucial for counting the number of particles in a single hologram, these parameters have minimal effect when applied to a sequence of images for which the particles are tracked because over-segmentation noise rarely persists for multiple frames.

Because inverse approaches depend on matching the recorded image using a model, any image features that are not modeled (e.g., background intensity variations, imperfections in the optical path) will reduce the quality of the fit. To rectify this, we preprocess the recorded images by removing the constant background using the method of [50] (subtraction followed by division by the square root). The background is computed as the mean of a time sequence of holograms in which the objects of interest have significant motion.

While compressive holography and inverse methods have existed for over a decade, this is the first application to 3D PTV. Previous uses of a parametric inverse method for particle tracking have tracked fewer than 10 particles concurrently [89, 103, 104, 91]. Furthermore, CH is usually used with a small number (~ 10) of reconstruction planes with a large spacing (~ 1 mm) between planes. Here we demonstrate the ability to reconstruct volumes with over 1000 planes with both cubic and elongated reconstructed voxels. The largest volume reconstructed by Endo et al. [97] contained 10^7 voxels while our sparse representation enables reconstruction of volumes containing more than 10^9 voxels on a desktop computer. The use of the fused lasso regularization to enforce both smoothness and sparsity has not been previously demonstrated for compressive holography. To emphasize these distinctions, we refer to our method as a Regularized Inverse Holographic Volume Reconstruction (RIHVR, pronounced "river"). RIHVR

dramatically increases the SNR of the reconstructed volume. This enables processing of high noise and high particle concentration holograms (both traits are common in DIH-PTV applications) that could not be reliably processed using existing methods. Because RIHVR does not assume a size or shape of the object, it can be used when the imaged particles are polydisperse or non-spherical. We next present several practical examples to demonstrate these capabilities.

2.3 Demonstration cases

To demonstrate that the proposed method is applicable to a variety of DIH-PTV cases, we present the results for processing four classes of holograms: an isolated nanowire, simulated tracer particles in isotropic turbulence, swimming microorganisms, and an experimental T-junction flow seeded with microfibers. The first case, the isolated nanowire, demonstrates improved 3D reconstruction of a continuous object with a significant 3D shape. Simulated holograms then provide a realistic flow case for which ground truth exists for the particle locations. The RIHVR method is evaluated against deconvolution (with inverse iterative particle extraction where applicable) which has been previously validated against conventional PIV and shown to provide substantial improvement over other DIH-PTV approaches [40]. A simple reconstruction method following the approach of Pan & Meng [105] (global thresholding followed by peak intensity depth localization) is also shown for comparison. Experimental holograms of swimming microorganisms and microfibers in a T-junction flow represent real measurement domains for which some flow behaviors are known from prior studies. These later cases demonstrate that RIHVR can be applied to broad measurement domains where other DIH-PTV methods fail.

2.3.1 Isolated nanowire

A qualitative evaluation of the proposed inverse reconstruction method uses a silver nanowire in suspension. This is an example of a continuous object with significant extent in all three reconstruction dimensions. The length of the wire is not known *a priori*. As such, a parametric inverse model such as the one used by Soulez et al. [82] is unsuitable. The sample is a suspension of 90 nm diameter Ag nanowires in isopropyl alcohol. The

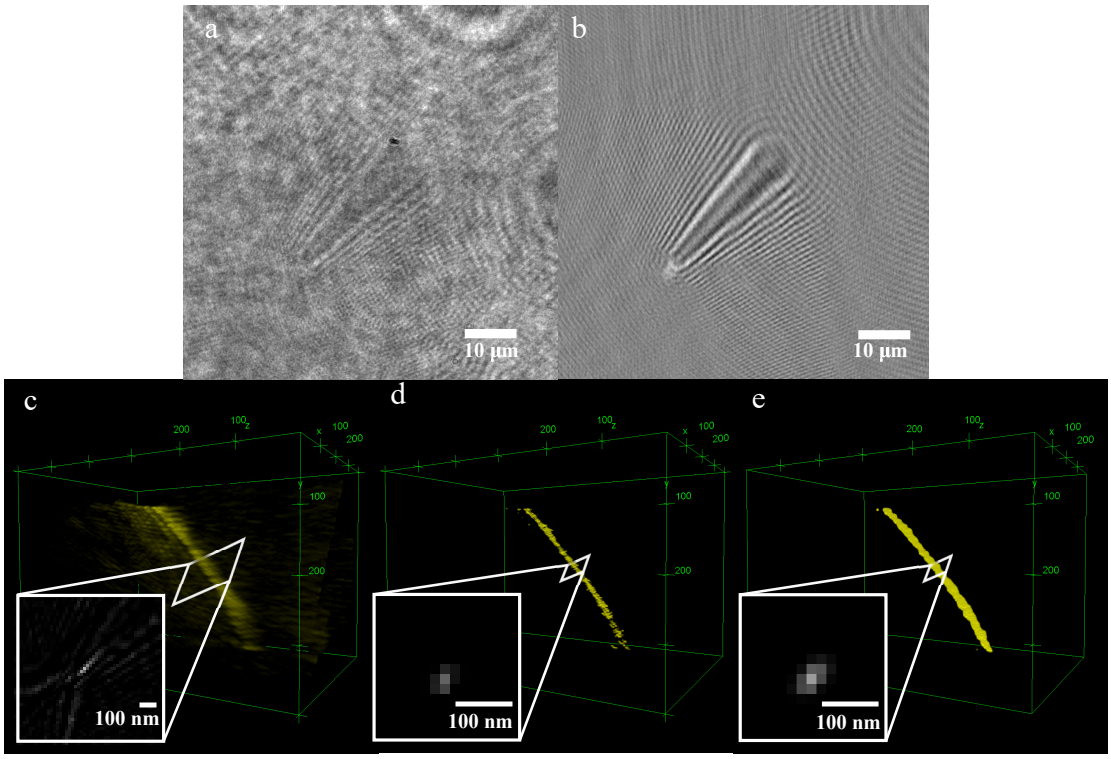

Figure 2.1: (a) Recorded holographic image of a 90 nm Ag nanowire. (b) Hologram after image enhancement. (c) Volumetric reconstruction of the sample using the deconvolution method. (d) Reconstruction using RIHVR with sparsity (ℓ^1) regularization. (e) Reconstruction using RIHVR with fused lasso (FL) regularization. For visualization, (c) uses the intensity as the transparency alpha value while (d) and (e) show all non-zero values at equal intensity.

illumination source is a 450 nm fiber-coupled laser diode (QPhotonics QFLD-450-10S), collimated using a Nikon CFI Plan Fluor 10X objective lens. A Nikon CFI Apo TIRF 100X oil immersion microscopic objective and video camera (Andor Zyla 5.5 sCMOS) are used to image the sample. The recorded pixel size is 70 nm. The recorded image (2560×2160 pixels) is cropped to a 1024×1024 pixel region around a selected nanowire to ensure that only a single object is in the image and to reduce unnecessary computational cost. Reconstruction is performed at 70 nm intervals (equal to the lateral pixel pitch) for a depth of 42 μm (600 planes). Measurement of similar samples using DIH has been undertaken by Dixon et al. [85] who measured the diffusion of nanowires and Kempkes et al. [106] who demonstrated a 2° accuracy for the orientation of microfibers.

Unlike the prior methods, our approach does not assume a linear fiber and is suitable for measuring non-rigid wires.

The raw and enhanced holograms are shown in Figs. 2.1(a) and 2.1(b) respectively alongside renderings of the reconstructed volumes produced using deconvolution, RIHVR with sparsity regularization ($\lambda_{\ell^1} = 0.27$), and RIHVR with fused lasso regularization ($\lambda_{\ell^1} = 0.15$, $\lambda_{TV} = 0.12$). Figures 2.1(c)–2.1(e) show that both regularization methods substantially reduce the DOF of the reconstruction. Measured as the width at half the measured intensity averaged along the wire length, the DOF decreases from 1.97 μm using deconvolution to 0.63 μm and 0.89 μm using the sparsity and fused lasso regularization methods respectively. Similarly, a 99% decrease in the segmented volume and 90% decrease in the segmented cross-sectional area is observed between deconvolution and RIHVR (with similar reduction for both RIHVR regularizers).

When comparing the results generated using the sparsity and fused lasso regularization methods in Figs. 2.1(d) and 2.1(e), the smoothing effect of the fused lasso is apparent. The fused lasso regularized results show fewer gaps in the wire profile and an overall more contiguous object. However, this comes at the cost of some expansion of the object and a slightly larger DOF. Interpolated cross-sections normal to the wire axis (insets in Fig. 2.1) illustrate that both RIHVR approaches approximate the true circular shape of the wire. Conversely, Fig. 2.1(c) shows that deconvolution produces an X-shaped cross-section characteristic of simple holographic reconstructions. RIHVR also demonstrates robustness to image noise. The raw image in Fig. 2.1(a) has a substantial amount of background noise and even enhancement via background removal does not produce a noise free image. Additional fringe patterns – caused by vibrations, fluctuations in illumination intensity, and out-of-view objects – are visible in Fig. 2.1(b) (the enhanced image) but do not result in artifacts in the reconstructed volume when using RIHVR.

2.3.2 Synthetic turbulent flow

Turbulent flows represent the most challenging case for 3D flow measurements as they are highly three-dimensional and involve velocity fluctuations across a broad dynamic

range of scales. Here we assess the accuracy and limitations of our method using simulated holograms of a homogeneous isotropic turbulent flow. The simulated tracer particle trajectories are determined by querying the forced isotopic turbulence data from the Johns Hopkins Turbulence Database with Lagrangian particle tracking [107, 108, 109]. The simulation domain is scaled to $5 \times 5 \times 5$ mm^3 and sampled with a nondimensional time step of 0.012 (60 DNS time steps) to capture 100 instants (image frames). The Reynolds number based on the domain size is 23,000 and the Kolmogorov length and time scales (smallest scales of turbulent fluctuations) are 67 μm and 3.7 frames respectively. The RMS velocity is 6.7 μm/frame. Maintaining the Reynolds number and using a low viscosity fluid ($\nu = 10^{-7}$ m^2/s), this corresponds to a frame rate of 75 kHz which is achievable with modern cameras. One thousand particles with a diameter of 7.5 μm are initially randomly spatially distributed throughout the 3D domain and their positions at subsequent time steps are determined using a Lagrangian tracking method [109]. A periodic boundary condition is applied to the particles to ensure that the number of objects in the field of view is constant (this is ignored during processing). The simulated holograms are 512×512 pixel images with a 10 μm pixel size and 632 nm illumination wavelength. A sample hologram is shown in Fig. 2.2.

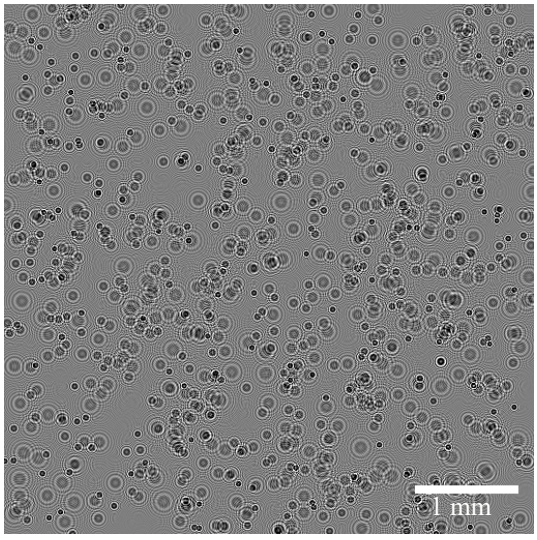

Figure 2.2: Sample simulated hologram containing 1000 particles

The reconstruction plane spacing is equal to the lateral pixel spacing (10 μm). The

total size of the reconstructed volume is $512 \times 512 \times 700$ voxels (1.8×10^8). 100 FISTA iterations are used with regularization parameters $\lambda_{\ell^1} = 0.5$ and $\lambda_{TV} = 0.2$. For segmentation, the minimum intensity threshold is set to $2/256^{th}$ the maximum and the minimum volume is 5 voxels. The particle positions are estimated using the weighted centroid of each connected component and the particles are tracked using the method of Crocker & Grier [110] with a maximum per frame displacement of 70 μm and a minimum tracked duration of 10 frames. Two alternative hologram reconstruction methods are presented for comparison. The first is a simple reconstruction method following the approach of Pan & Meng [105]. The second is the deconvolution method of Toloui & Hong [87] with two passes of the inverse iterative particle extraction step. The particle trajectories for all methods are smoothed with a total variation filter. The tracked results using RIHVR are shown in Fig. 2.3(a).

To evaluate the localization error, extracted particles are matched to their true location using a nearest neighbor method [110]. The resulting error distributions in each dimension are summarized in Fig. 2.3(b). For all three methods, the error in x and y is very small (smaller than the pixel size). However, the error in z is substantially greater, demonstrating the DOF problem. Comparing the three methods, the 75^{th} percentile decreases from 11.5 voxels using reconstruction to 6 voxels using deconvolution and 3.5 voxels with RIHVR. The same trends are seen at the other percentiles as well. Thus, RIHVR produces a 40% improvement in longitudinal localization over the prior best method and a 70% improvement over simple reconstruction. These trends also hold when evaluating the mean error of the unfiltered instantaneous velocity measurements. The error in the axial velocity, w, decreases from 13.4 voxels/frame with reconstruction to 3.8 voxels/frame with deconvolution and 2.4 voxels/frame with RIHVR.

For turbulence measurements, it is common to measure Reynolds stresses, which are velocity fluctuation statistics [49]. Here we present measurements of the root-mean-square (RMS) velocity in Fig. 2.3(c). This is comparable to Reynolds stress when the mean is zero (as it is for this flow) while maintaining intuitive meaning for applications other than flow measurement. For this flow in the period during which particles are simulated, the true RMS velocities averaged over the whole volume are (6.3, 7.6, 6.2) voxels/frame in the u, v, and w directions respectively. The trajectory smoothing produces a 3% error in the u_{RMS} and v_{RMS} measurements but significantly reduces

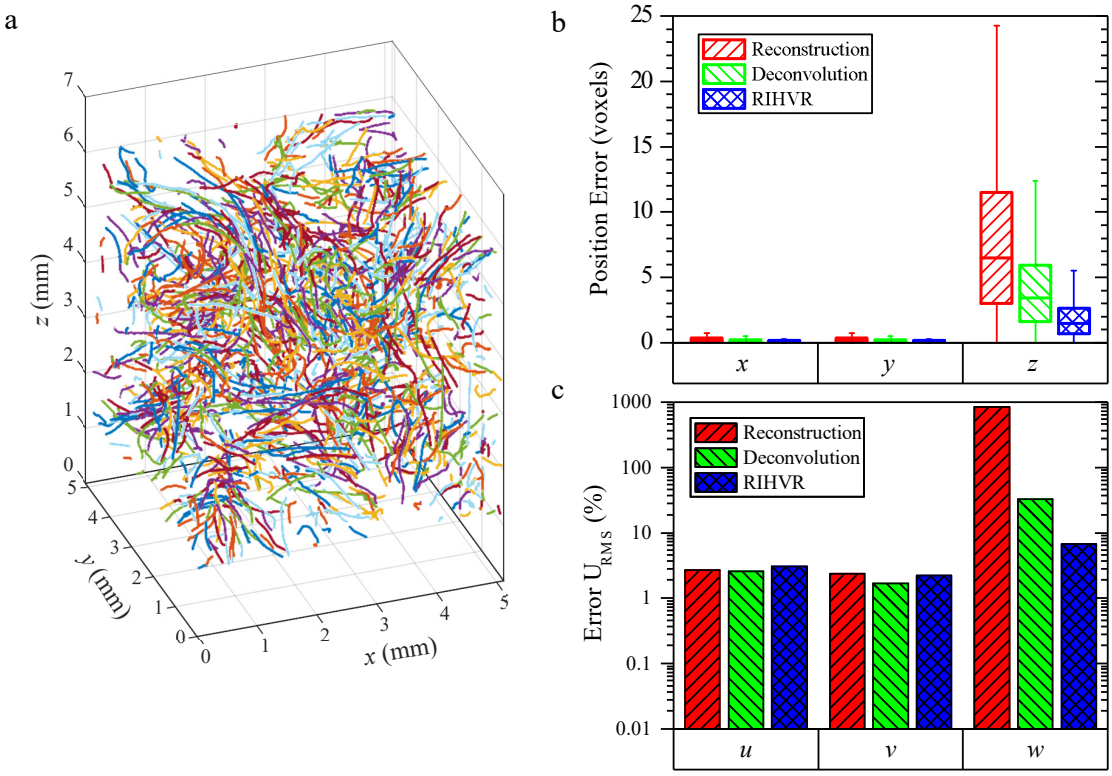

Figure 2.3: (a) Smoothed 3D particle trajectories extracted from a synthetic hologram using RIHVR. (b) Localization error of tracked particles relative to their true locations. (c) Error in the RMS velocity components of the three test methods compared to ground truth.

spurious fluctuations in z. Using reconstruction, the measured w_{RMS} differs from the true value by over 800%. This is reduced to 30% using deconvolution. However, this is still unacceptably high for real measurements. The error using RIHVR is only 7% which is substantially better and only 2× greater than the error in the u and v measurements.

As the velocity vector spacing in PTV is directly related to the particle spacing, the maximum particle concentration is a critical concern for many PTV measurements. The quality of recorded holograms depends on several factors including the particle concentration, size, volume depth, wavelength, magnification, and numerical aperture. Here we focus on only the particle concentration to compare the tested methods. Note that the results may vary with changes to the other parameters but the relative comparisons between the methods should remain consistent. In general, the extraction rate

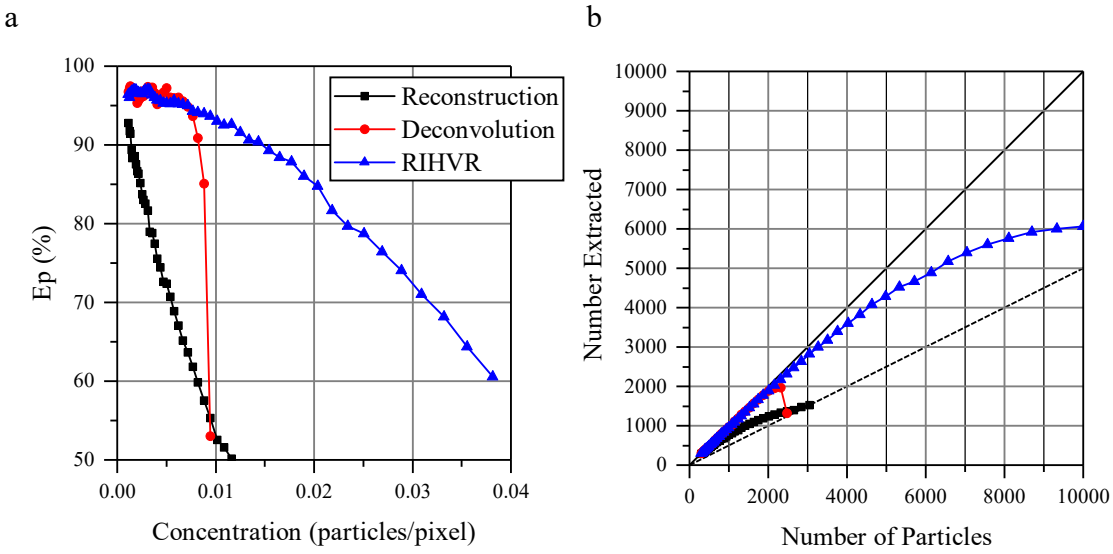

Figure 2.4: (a) Extraction rate for each method for increasing particle concentrations. (b) The number of particles which can be accurately extracted is higher for RIHVR than the other methods. Solid line is 100% EP, dashed line is 50%.

(*Ep*, number of correctly extracted particles divided by true particle count) decreases with increasing concentration. we use the number of particles per pixel to scale the concentration because it allows for the most direct comparison with the literature. It has previously been shown that the commonly used shadow density (Eq. (1.8)) does not completely explain the extraction rate in all situations [71, 87]. For comparison, Toloui et al. [40] performed measurements with a concentration of 0.0035 particles/pixel while other sources used significantly lower concentrations. Figure 2.4(a) shows that concentrations of up to 0.035 particles/pixel can be processed using RIHVR while maintaining $Ep > 60\%$. The increased number of extractable particles enabled by RIHVR, as shown in Fig. 2.4(b), enables increased resolution in velocimetry applications and higher particle concentrations in other applications including studies of biological flows and fluid-particle interaction where high concentration may be crucial for the sample being studied. An example of such a case is given in section 2.3.3.

2.3.3 Swimming algae

One practical application of DIH-PTV is the study of microorganism swimming behaviors. Previous studies have used small sample volumes ($\sim 0.05\mu$L) in order to measure the large cell concentration present in cultures ($\sim 10^6$ cells/mL) [51, 79]. Here we demonstrate that RIHVR is superior to prior DIH algorithms for these experiments. We also demonstrate the ability to record and process much larger sample volumes ($\sim 1\mu$L) which could enable new scientific studies.

The alga *Dunaliella primolecta* is a unicellular species which can be used for biofuel production [111]. Cells have a length of 10 μm and swim using two flagella [112]. In this study, *D. primolecta* is grown at 37°C in a growth medium. Manual concentration measurements using a microscope indicate that the sample has a concentration of 1.8×10^6 cells/mL. The sample container is a $10 \times 30 \times 1$ mm^3 glass cuvette. Holograms are recorded at 100 Hz using a 2048×1088 pixel sensor (Flare 2M360-CL). The sensor pixel size is 5 μm and the exposure time is 50 μs. A 5x microscopic objective is used, resulting in a recorded sample volume of $2.05 \times 1.09 \times 1$ mm^3. For simplicity and speed, the recorded image is cropped to a size of 1024×1024 pixels (1×1 mm^2). The light source is a 532 nm diode laser (Thorlabs CPS532) which is expanded and filtered with a spatial filter, as shown in Fig. 2.5(a). While the number of particles per pixel is relatively low for this sample (0.002), the particles are large enough that the shadow density (Eq. (1.8)) becomes significant, $s_d = 18\%$. The maximum shadow density used by Toloui et al. [40] was 10.5% using deconvolution, while Malek et al. [71] achieved an extraction rate of only 20% for $s_d = 10\%$. Reducing the measurement depth can enable holograms to be processed using conventional methods [112], but risks introducing wall effects that influence the behavior. Similarly, we have found that dilution of the sample changes the cell swimming behavior. Therefore, high concentration holograms – which can only be processed using RIHVR – are important to these microbiological studies. Studies of microorganism behavior using non-holographic methods are challenging because their 3D motion leads to low residence time in a microscopic depth of field and size constraints make multi-camera imaging difficult.

The holographic volume is reconstructed with 270 planes, separated by 3 μm, with the volume confirmed to include both walls of the cuvette. The regularization parameters are $\lambda_{\ell^1} = 0.1$ and $\lambda_{TV} = 0.1$ with 100 FISTA iterations and 5 gradient projection

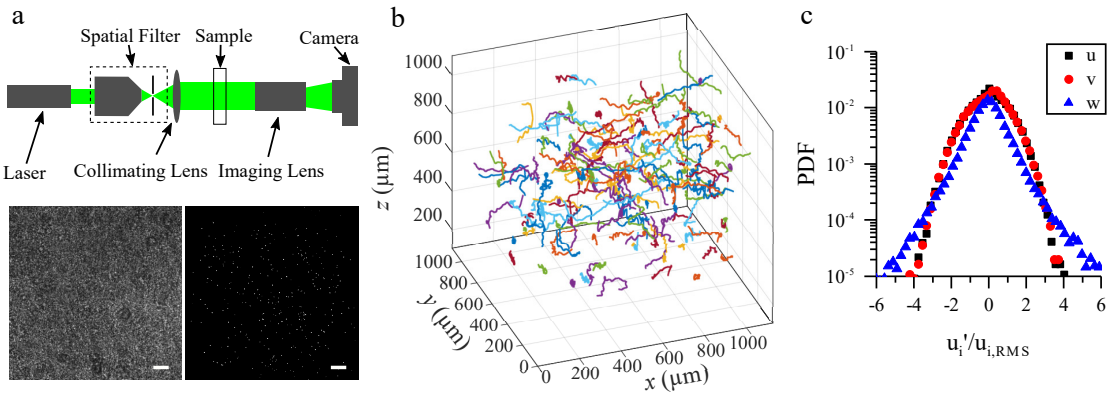

Figure 2.5: (a) DIH imaging system, recorded hologram, XY projection of processed reconstruction. Scale bars are 100 μm. (b) Subset (25%) of tracked particles. (c) PDF of velocity fluctuations in each direction. The w distribution has longer tails and a sharper peak but is not substantially wider than the other two components.

steps to evaluate the TV proximal operator. A sequence of 2000 frames is analyzed. A sliding window of 151 images (1.5 sec) is used to compute the mean background in order to reduce the effect of cells starting or stopping their motion. Because RIHVR uses a complex object model, it is equally suited to measuring amplitude objects (e.g., nanowire and synthetic objects) as well as phase objects such as the *D. primolecta* cells. More complex regularization methods (with associated higher computation cost) could be used to further enhance phase objects [95].

RIHVR detects and tracks an average of 294 objects per frame. This is dramatically lower than the expected count of 2000 cells/frame from the concentration measurement. However, a substantial number of particles are seen to remain stationary on the two walls. These are treated as background noise and are removed during the image enhancement. A selection of 3D tracks is shown in Fig. 2.5(b). For clarity, only a subset of 25% of the tracked data is shown in Fig. 2.5 while the full density is shown in Fig. 2.6. The cell trajectories have been smoothed using a Savitzky-Golay filter of 20 frames. The frame rate is sufficiently high that this filter does not suppress any real motions. Under the assumption that cell swimming motions are isotropic, the probability density functions (PDF) of velocity fluctuations (normlized by the RMS velocity) are expected to coincide for each component. Figure 2.5(c) shows that while the u and v velocities are in good agreement, the same is not true for w, even after smoothing. This indicates

that the DOF problem is not entirely eliminated for this extremely noisy case. However, gross motions in the longitudinal direction are visible and fine scale complex behaviors such has helical swimming can be seen from an enlarged view of the sample in Fig. 2.6.

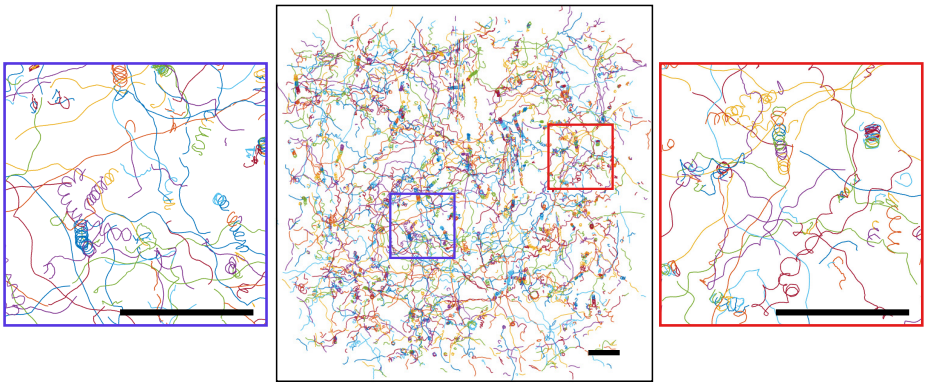

Figure 2.6: 2D view of the reconstructed cell trajectories showing complex behaviors Also illustrates the true cell concentration of processed volume. Scale bars are 100 μm.

2.3.4 Rotating rods in flow

In addition to improvements to the measurement accuracy and seeding density limits, RIHVR enables the measurement of complex shapes as previously illustrated in Fig. 2.1. Here we present a flow case where the seeding particles are rods rather than the usual spherical tracers. Using RIHVR, we are able to extract both the location and orientation of each rod and track their evolution in the flow. This type of multimodal measurement using a single camera has not been previously reported.

To demonstrate this measurement, we use the T-junction flow of the type studied by [113] which occurs frequently in industrial and biological flows. The rotation and alignment of fibers in flow have been extensively studied for target applications including paper manufacturing and microorganism alignment (see for example [114, 115, 116]). The fibers used for the present study are marketed as an additive to strengthen composite materials, where the alignment of the fibers may have an impact on the material properties. Prior experimental work has either been restricted to 2D measurements [115, 114] or multi-camera 3D measurements of individual fibers [116]. Holography is a valuable alternative when the motion is three-dimensional, seeding density is high, or

optical access is restricted.

The experimental channel has a square cross-section with a side length of 1 mm. The junction is at a right angle and all three branches (inlet and two outlets) have the same geometry. The inlet flow rate is 1000 mL/hr which corresponds to a Reynolds number $Re = 290$. The seeding particles are 7 μm diameter SiC ($\rho = 3$ g/cm^3) microfibers (Haydale Technologies) with an aspect ratio of 10. The response time of the particle, computed using the equivalent diameter, is $\tau_p = 14$ μs. The characteristic time of the flow is $\tau_f = 1.9$ ms. The resultant Stokes number is $St_k = 0.007$ indicating that the particles will trace the flow. A high speed video camera (NAC Memrecam HX-5) is used to record the holograms at 6000 Hz with an exposure time of 50 μs. A microscopic objective (Edmund Optics, 10x, NA=0.45) is used to image the sample, resulting in a 1024×1024 image with a pixel size of 0.91 μm. The light source is a spatially filtered HeNe laser ($\lambda = 632$ nm). The FL regularization method is used with $\lambda_{\ell^1} = 0.1$ and $\lambda_{TV} = 0.12$. 110 reconstruction planes are used with a spacing of 9.1 μm (10$\times$ the pixel pitch). An intensity-weighted principle component analysis is used to determine the orientation of the fibers (similar to the method of [106]).

For validation of the flow field, the flow (absent any particles) is simulated using ANSYS Fluent (ANSYS, Inc.), with the results found to be in agreement with the simulations of [113] and the experimental particle pathlines. The fiber rotation rate is modeled using the Jeffery equation in the limit where the particle aspect ratio is $\gg 1$ [117]:

$$\dot{p}_i = \boldsymbol{\Omega}_{ij} p_j + (\boldsymbol{S}_{ij} p_j - p_i p_j \boldsymbol{S}_{jk} p_k) \tag{2.10}$$

Here $\boldsymbol{p}$ is a unit vector aligned with the particle axis, $\boldsymbol{\Omega}$ is the rotation tensor, and $\boldsymbol{S}$ is the strain rate tensor. Because the particle rotation rate is coupled to the orientation, the rotation rates for the simulation in Fig. 2.7(c) assume that the particles are initially aligned with the inlet flow direction.

The experimental fiber orientations are shown in Fig. 2.7(a) along with vorticity isosurfaces from the simulation which illustrate that the principle flow features predicted by the simulation (two vortices aligned with x) are present in the experiment. A 2D projection of the fibers is shown in Fig. 2.7(b). The optical reconstruction direction corresponds to the crossflow (z) axis in Figs. 2.7(a)–2.7(d). The clear appearance of the two counter-rotating vortices demonstrates that RIHVR sufficiently reduces the DOF

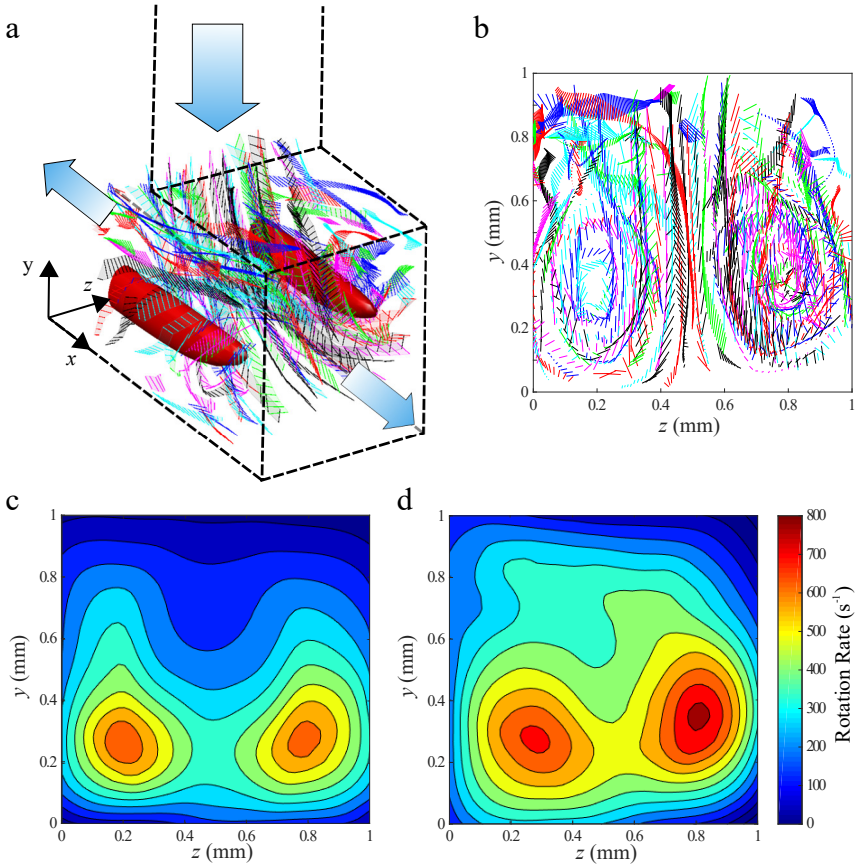

Figure 2.7: (a) Visualization of the measured rod trajectories. Solid lines show the measured 3D orientation of the rods. Colors indicate individual particles. Vorticity isosurfaces ($\omega = 3000s^{-1}$) are from the CFD simulation. (b) View of the experimental fiber orientations in the yz plane. (c) Contour map of the particle rotation rate (s^{-1}) expected from the simulation. (d) Measured 3D particle rotation rate.

to enable the recovery of this 3D flow feature. Additionally, changes in the orientation of the fibers can be seen. The measured rotation rate ($|\dot{p}|$) is higher near the centers of the vortices in Fig. 2.7(d) which matches the expected behavior from the simulation shown in Fig. 2.7(c). The peak rotations rates are accurate to 30% while the location of the peaks are accurate within 0.1 mm. Some discrepancies between the measured and predicted rotation rates can be attributed to misalignment between the two domains. Because the rotation rate is dependent on the velocity gradients (which have substantial variation) and on the particle location and orientation (which have some measurement uncertainty), even small misalignment of the two domains would cause deviations between the two results. Non-ideal flow conditions, including unsteadiness and geometrical imperfections, could cause differences in the locations of the vortices and the peak rotation magnitude. The accuracy of the machining process used to make the channel is ± 0.05 mm which is comparable to the peak location error. Since the flow rate is constant, uncertainty in the channel geometry also produces uncertainty in the inlet flow velocity. Finally, the Jeffery equation (Eq. (2.10)) used to predict the particle rotation rate assumes non-inertial ellipsoidal particles in Stokes flow. The true particle motion is expected to deviate slightly from this idealization. Given these uncertainties, we conclude that the agreement between the simulation and experimental results is adequate for demonstrating that RIHVR enables direct 3D particle rotation rate measurements.

2.4 Discussion and conclusions

The processing speed of RIHVR is suitable for many applications. Further adjustments by the user can enable even faster processing for specific cases. If axial uncertainty is less important, the number of reconstruction planes can be reduced, provided the planes are still sufficient to model the object field. The use of pure sparsity (ℓ^1) regularization further improves speed at the cost of poorer SNR. Finally, the number of solution iterations can be reduced at the cost of a less converged solution.

While RIHVR is broadly applicable, there remain some limitations. The enhancement approach using a time-averaged background is only suitable for moving objects. The solution to the minimization problem (Eq. (2.1)) depends on the choice of the

regularization parameters λ_{ℓ^1} and λ_{TV} which are user-specified. For most experimental cases, parameter values near $\lambda_{\ell^1} = 0.1$ and $\lambda_{TV} = 0.1$ are appropriate. These can each be increased (or decreased) to reduce noise (λ_{ℓ^1}) or increase the smoothness (λ_{TV}) of the result. Automatic selection of these parameters is an area of ongoing research. The assumption of a sparse and smooth object field may not be true in all cases, for example if the medium has fluctuations in the index of refraction. Finally, FISTA assumes that the regularized minimization problem is convex. This assumption breaks down for large objects when a large number of reconstruction planes are used. These restrictions generally do not apply to PTV applications.

We have demonstrated the application of CH techniques to volumetric reconstruction, using the presented RIHVR approach for the reconstruction and tracking of 3D particle fields.T he reconstructed volumes are both sparse and smooth, assumptions that apply equally for most particle tracking applications. The use of GPU processing and sparse storage enable the reconstruction of volumes containing over 10^9 voxels which is orders of magnitude larger than previously reported for any CH method. RIHVR provides a substantial improvement in the longitudinal position and displacement measurement accuracy in addition to an increase in the particle concentration limit. These improved capabilities have allowed the extension of DIH-PTV to the tracking of a dense culture of microorganisms and measuring the orientation of microfibers in 3D flow. RIHVR is a broadly applicable approach capable of enabling low-cost 3D measurements for wide-ranging applications.

Chapter 3

Dense Particle Tracking using a Learned Predictive Model

The content of this chapter is under review for publication by the author in Experiments in Fluids.

3.1 Introduction

The Lagrangian particle tracking paradigm used for particle tracking velocimetry (PTV) enables high resolution 3D flow field measurements. However, a major limitation of traditional PTV applications is that the particle displacement must be small relative to the spacing between particles. Malik et al [28] defined the particle displacement ratio $p \equiv s/u\Delta t$ where s is the mean distance between neighboring particles, u is the particle speed, and Δt is the time between images. Malik states that PTV is only possible when $p \gg 1$. However, practical considerations often lead to a smaller p. For flow measurements, the particle spacing must be small in order to resolve small flow features. For biological studies, a large sample size is desirable but also leads to a small s if the field of view is fixed. Finally, the camera frame rate may be limited and is inversely proportional to the field of view and recording duration. It is common in PTV applications to describe the particle concentration in terms of the number of particles per pixel (ppp) or particles per voxel. This value is closely related to the difficulty of particle localization from the recorded images [31]. However, high ppp does not

necessarily make the linking step challenging if p is large due to a high frame rate or low velocity.

There are several approaches that can be used to enable tracking of particles with large displacements. One such method uses PIV to approximate the velocity field [118, 119]. This velocity can then be used as an initial guess for particle motion, effectively changing the particle displacement ratio to be $p_1 = s/(u'\Delta t)$ where $u' = u - \hat{u}$ is the deviation of the speed from the estimated value ($\hat{u}$). This method is useful for cases such as channel flow where $\hat{u} \gg u'$. However, it is not suitable for cases without a predominant mean motion such as homogeneous isotropic turbulence or swimming microorganisms. For such cases, a linear or polynomial motion model can be used to predict the future position of a particle given its history. This method is dependent on the quality and applicability of the model being used and it will fail if unexpected motion such as large acceleration or a sudden change in direction occurs. These events are rare for flow measurements [120] but are common in biological samples [51, 58]. Furthermore, this method relies on sufficient initialization of the particle tracks in order to fit the model. Some particles must be tracked initially in order to make inferences. Finally, the popular Shake-The-Box (STB) method [31] combines the localization and tracking steps, reducing localization errors and false detections (which complicate tracking) by using feedback from the tracking step. STB generally requires an initialization period of up to 40 frames, which is not achievable for high-speed flows where double-pulse measurements are required. An iterative approach has been presented which enables STB for multi-pulse measurements by using a time-averaged velocity field from tomographic PIV as a velocity predictor [119]. Crucially, STB requires a calibrated optical transfer function (OTF) to project the 3D particle positions to a 2D image. More generally, the OTF is an image formation model which must account for complex object geometry (common in biological applications) or non-linear image formation (coherent imaging such as holography). This makes it difficult to implement STB for these cases.

Machine learning approaches have previously been demonstrated for PTV. Grant & Pan [121] trained a neural network to identify the most likely candidate particle in a double exposure image. This method is only suitable for 2D flows with sufficiently low concentrations. It also only utilizes two frames while more complex motions may only be apparent with many more frames. Labonté [122] trained a neural network to identify

a continuous function for the fluid velocity with respect to position. This velocity is then used as an estimate like the PIV approximation method previously discussed and the method suffers from similar limitations: mainly that there must be a mean flow and minimal unsteadiness. Beyond fluid measurements, learned tracking methods have been used to aid in the multi-camera tracking of fish [123] and plasma science [124]. It is also important to distinguish between the two elements of particle tracking: localization and linking. Localization is the identification and quantification of particle locations in an image (or set of images), usually producing an unordered set of position vectors. Linking identifies which positions in the set belong to unique objects. In the machine learning literature, it is common to refer to only the localization problem as tracking.

In this chapter, I focus exclusively on the linking problem, as the detection problem has already been discussed in Chapter 2. I demonstrate that machine learning can be used to drastically increase the particle density and velocity resolution limit for PTV applications. Our data-driven approach learns particle motion patterns present in the data and uses these to accurately predict future motion. This leads to a decrease in the u' component of p_1, enabling higher particle concentrations. I present simulated and experimental results for flow measurement applications to demonstrate that this learned predictor is superior to other tracking methods. In particular, comparisons are made to the open-source trackpy python library [7] which is an implementation of the Crocker & Grier [110] method for particle linking. This library was selected considering its popularity in the field (i.e. highly cited) and the fact that it has proven to be applicable to a broad range of particle tracking applications [125, 126, 40, 127]. The library includes several predictive tracking methods and allows the implementation of custom predictors such as the proposed learned predictor.

3.2 Methods

The linking problem is re-posed as that of predicting the velocity of each particle as has previously been suggested by Wang et al. [123]. Conceptually, if the velocity of each particle can be predicted exactly, then $u' = 0$ and the linking problem becomes trivial. While such accurate prediction is not possible, any improvement compared to simpler predictors will lead to increased tracking capability. Figure 1 shows three cases where

some predictive linking methods could fail but a learned motion predictor would succeed. Without prediction, even simple linear motion (Fig. 3.1a) would produce incorrect tracks. A predictor modeling the flow field can perform well when the particle velocity is closely related to position (Fig. 3.1b). However, turbulence or other uncertainties may invalidate this assumption. For cases with highly complex motion (Fig. 3.1c), highly specialized models are needed to predict the motion. One such motion is helical motion which has been observed in swimming microorganisms [127]. The proposed learned motion model is suitable for any of these situations. The motion prediction is performed using a neural network which takes the (variable length) history of an object as the input and predicts the future velocity. The model architecture is summarized in Fig. 3.2.

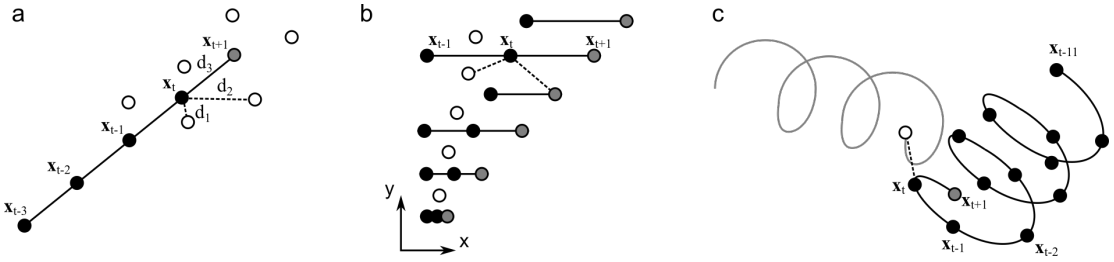

Figure 3.1: Toy examples to illustrate the challenges associated with solving the linking problem in different cases. Black lines indicate particle paths. Filled black circles indicate historical linked positions. Gray circles indicate correct future links. White circles are available positions in the future frame. Dashed lines show potential incorrect links. (a) Linear motion. Simple nearest-neighbor or null predict pairing would incorrectly choose the link d_1 instead of d_3 as $d_1 < d_3$. A simple motion model (such as linear) may be suitable. (b) Shear or channel flow. There is a functional relationship between position and velocity that can be used for prediction even when there is no history for the trajectory (upper-most trajectory). (c) Complex helical motion. A linear or polynomial model would choose an incorrect link. A complex motion model such as the proposed learned predictor would be needed to correctly predict the particle location.

The predictive model uses the Long Short-Term Memory (LSTM) recurrent neural network architecture as it is specialized for timeseries applications such as handwriting and speech recognition and musical prediction [128, 129]. LSTM consists of a number of memory blocks (units) that operate recurrently on a time-series of N-dimensional data. The blocks take as input the data at a single timestep and the output of the

previous timestep and transform that into a scalar output (for each block) using a set of weights and gate functions. These gates allow LSTM to retain long-term memory about a sequence while reacting appropriately to short-term changes. LSTM has been applied to problems related to the present work. The future path of a single pedestrian was predicted by Hug et al. [130] who focused on improving destination inference for security applications. Tsaris et al. [131] used LSTM to identify particle trajectories from streak images for high energy particle experiments. Wang et al. [123] used LSTM to improve the cross-view association for multi-camera tracking of fish.

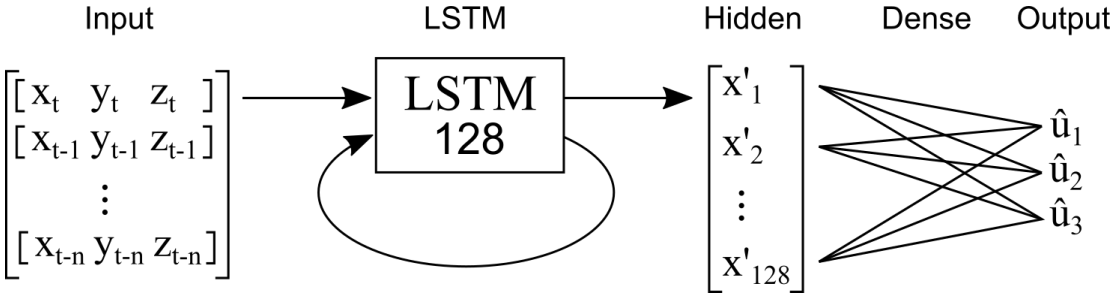

Figure 3.2: The learned predictor model architecture showing the LSTM and Dense layers used to produce a predicted velocity vector from a sequence of positions.

The proposed learned predictor model uses 128 LSTM units which are fed the position history of a single trajectory. The LSTM outputs are then passed through a densely connected layer (where each input-output pair are weighted and summed) to produce the velocity predictions. A hyperbolic tangent activation function is used for this final layer to produce outputs in the range $\hat{u} \in (-1, 1)$. The input to the model is a $T \times D$ matrix where D is the dimensionality of the object position data (usually 3 or 2) and T is the number of timesteps used for prediction. The choice of T depends on the complexity of the motion being observed. A small T (such as 2) will result in a relatively simple model while a large value such as 20 will be able to learn more complicated behaviors such as helical motion. An increased T comes with increased computational cost to train the model and requires higher quality training data as the training trajectories must have a longer duration over which they are reliable. Usually, $T = 5$ is suitable for flow tracking applications and there is minimal sensitivity to the precise value chosen provided it is not extremely long or short for the requirements of the desired application. A good rule of thumb is that T should be chosen to be large

enough that a human could manually predict the future location from the trajectory history. The input positions are normalized using the min and max dimensions of the measurement domain. This normalization ensures that $\hat{u} \in (-1, 1)$ which is the output range of the hyperbolic tangent activation function on the output. Note that unlike Wang et al. [123], we use the positions rather than the velocities as the model input. This enables the model to implicitly learn the spatial velocity field of the flow if it is useful to the case for which it is trained. While the proposed model architecture is extremely simple, it has proven capable of excellent performance on each of the test cases to be subsequently discussed. The model simplicity means that it can be both trained and evaluated quickly, with negligible increase in the cost of tracking when compared to the other predictors in the trackpy library. For some situations (such as the highest concentration synthetic test cases), the learned predictor actually increases the speed of tracking.

Because the model learns to predict the expected motion of particles, it must be separately trained for each application. It is unreasonable to expect a model trained to predict the motion of swimming microorganisms to produce accurate predictions for tracers in a turbulent channel. Therefore, we use a data-driven approach to train a model specialized for each case. Model training requires collecting a set of training data – accurate trajectories exhibiting the motion patterns expected in the target data. We propose two methods for acquiring these data for experimental measurements. The first is to use an existing tracking method with manual intervention to identify exemplary and representative trajectories (i.e., those that demonstrate all the motions seen in the flow) to be used for training. The second method is to run a supplemental experiment in which tracking is trivial ($p \gg 1$) but the experimental conditions remain the same. This could include using a low tracer concentration or high frame rate even when these are not suitable for the target experiment due to resolution or duration requirements. This is preferable for cases when experimental replication is simple and cheap (as with many fluids measurements). While collecting training data does require additional experimental effort, the level of user expertise required is reduced compared to conventional linking approaches which require the user to carefully select and tune a model for complex cases.

The lengths of the trajectories used for training are generally greater than T. These

trajectories are separated into segments of length T that are then used for training. This ensures variety in the locations of the training points to enable the model to learn the flow field if applicable. To allow the model to predict accurately even when complete history is not available (e.g. for new particles entering the field of view), the $T \times D$ input data matrix is randomly augmented through truncation to contain $n < T$ timesteps and padded with zeros to return to the necessary $T \times D$ size.

The model is implemented using Keras [132] and trained using the Adam optimizer [133] with the default learning rate. The batch size is 32 and the model is generally trained for 400 epochs (i.e., 400 passes over the training data set). The batch size was chosen in part because it is a commonly used value in the literature. The number of epochs was chosen based on the loss curve. A loss curve that converges to an asymptotic value indicates that the number of epochs is sufficient. It is worth noting that the number of *iterations* (the number of epochs multiplied by the number of batches per epoch) is more useful than the number of epochs when extending to a new dataset. If the dataset is substantially smaller, more epochs would be needed to achieve the same number of iterations. The total training time is approximately 20 minutes on a system with a single Nvidia GTX 970 GPU.

Each of the experimental validation cases is acquired using digital inline holography (DIH), a single-camera 3D particle measurement technique [1]. Except when noted, the holographic images are processed using RIHVR (Chapter 2) to obtain the 3D object positions.

3.3 Validation

Five validation cases are presented to demonstrate the efficacy of the proposed method. The first is a synthetic channel flow to demonstrate accurate tracking even at extremely high tracer concentrations. The second is a standard synthetic PTV dataset through which the proposed approach can be readily compared to the literature. Third, an experimental turbulent channel flow is used to show that the learned predictor is suitable for experimental flows even without supplemental experiments. The fourth case is an experimental T-junction with high tracer concentration and a complex mean flow. Finally, a biological case of swimming algae is presented as an example where conventional

flow-based assumptions cannot be applied. In each of these cases, the proposed learned predictor method links more objects with fewer errors compared to baseline methods.

3.3.1 Synthetic Channel Flow

A synthetic flow case is used to evaluate the accuracy of the proposed approach and assess how this accuracy changes with increasing tracer concentration. The flow used is a direct numerical simulation (DNS) of a turbulent channel from the Johns Hopkins Turbulence Database [134, 107, 108] with a friction Reynolds number of $Re_\tau = u_\tau h/\nu = 1000$ and a bulk Reynolds number of $Re_b = U_b 2h/\nu = 39998$ where h is the half-channel height and U_b is the bulk velocity. Ideal flow tracer trajectories are simulated by randomly initializing the particles uniformly in the domain and incrementing their position with the instantaneous velocity at that location. Particles leaving the volume are reinitialized entering the opposite side. Only a $2 \times 2 \times 2$ region of the full $8\pi \times 2 \times 3\pi$ simulation domain is studied (dimensions are streamwise (x), wall-normal (y), and spanwise (z), respectively). This does include the entire wall-normal domain meaning that the streamwise velocity will depend on the wall-normal position. To prevent the model from overfitting the data, a test dataset is created at different streamwise and spanwise locations than the training data. The training data consist of 10 randomized particle fields, each containing on average 3100 trajectories lasting 20 frames with a timestep of 0.05. The model is trained for 100 epochs with a batch size of 32.

The test data is a sequence of 20 frames containing particles located in an unseen upstream region of the simulated channel. The number of particles (N_p) in the volume is varied from $N_p = 320$ to $N_p = 6.3 \times 10^4$ in order to evaluate the effect of concentration on tracking accuracy. The mean displacement is 0.05 non-dimensional length units per frame which leads to a displacement ratio between 0.38 and 3.5. Figure 3.3 shows a comparison of the proposed learned predictor (Learned) to several baseline predictive tracking methods found in the trackpy library [7]. Two metrics are used to evaluate the performance of each linking method: extraction rate and spurious rate. The extraction rate (E_p) is the fraction of true position links that are found by the linking method while the spurious rate (S_p) is the fraction of identified links that are incorrect. A high E_p enables high resolution on an extracted flow field while a low S_p ensures confidence in the results The simplest baseline predictor (Null) uses a velocity of zero as the initial

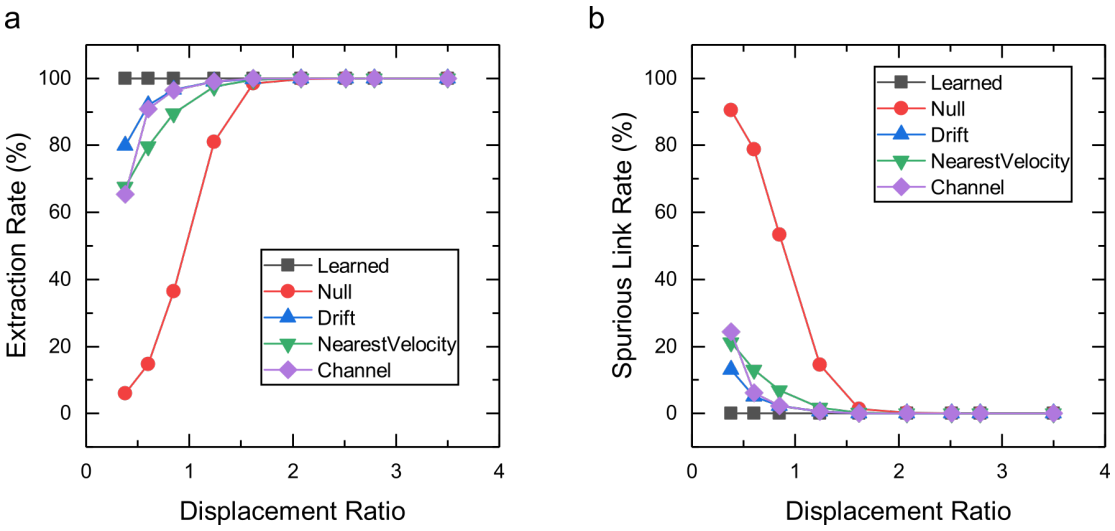

Figure 3.3: (a) The extraction rate for various linking methods is strongly dependent on the displacement ratio (p). For traditional methods [7], the extraction rate begins to decay when $p < 2$. The proposed learned predictor method has an extraction rate of nearly 100% at low displacement ratios. (b) The rate of spurious links shows that the learned predictor produces substantially fewer incorrect links.

guess and does not use any motion model. A slightly more advanced predictor (Drift) assumes a uniform mean velocity in the flow. which is automatically computed during tracking. For fluid flows, particles can be assumed to have a velocity similar to that of their neighbors (NearestVelocity). Finally, a predictor specially designed for channel flows (Channel) uses the modelled functional relationship between streamwise velocity and wall-normal location for prediction. The execution time for each of these methods is similar and strongly dependent on the particle density. For the case with $p = 0.6$, Null takes 110 minutes, NearestVelocity takes 84 minutes, and Learned takes 80 minutes. These times increase to over 7 hours for $p = 0.38$ but are only 2 minutes for $p = 1.2$.

For each of the baseline methods, E_p and S_p begin to worsen once the displacement ratio is less than one and they become completely extremely poor below $p = 0.5$ with $E_p < 80\%$ and $S_p > 15\%$. The proposed method retains $E_p > 0.9999$ and $S_p < 0.0001$ even at extremely low displacement ratios below $p = 0.38$. An illustration of this case is shown in Fig. 3.4. By comparison, the minimum displacement ratio at which Shake-the-Box was tested is $p = 2.3$ [31] while further experiments with dense tracer concentrations

have achieved $p = 1.5$ [135].

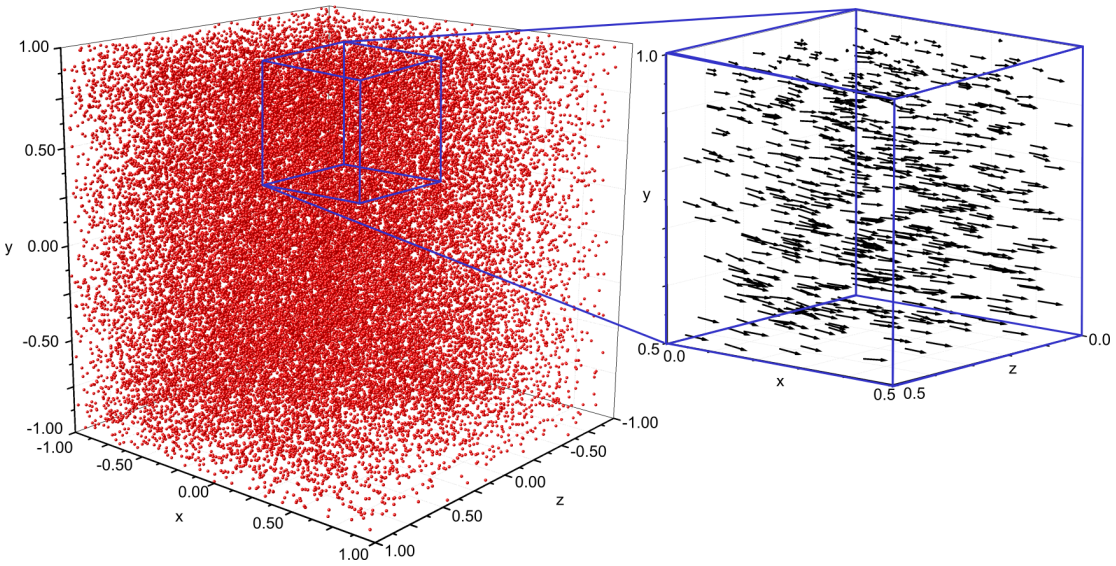

Figure 3.4: Illustration of the particle concentration for the $p = 0.38$ case. Displacement vectors for a small region near the upper wall are shown in the inset.

The improved performance of the learned predictor can be attributed to several factors. First, the predictor accounts for spatial dependencies of the velocity. The Channel and NearestVelocity methods are the only baseline methods with this capability. However, the Channel method is only suitable for a specific class of flows and NearestVelocity requires particle spacing to be small enough that spatial variations can be locally ignored. Another factor affecting tracking capability is the dependence on initial tracks. With the exception of MeanVelocity, each of the baseline predictive methods require some valid tracks to be present before predictions can be made. In the absence of these tracks, a null velocity assumption must be used and the predictive method reverts to the non-predictive Null method. If enough reliable tracks are identified with the null prediction, they can be used to aid prediction in future steps. However, when spurious links are identified with the null prediction (as is the case with increasingly high concentrations) they will lead to poor predictions. This could explain why the performance of the NearestVelocity, Channel, and Drift predictors is worse than Null in Fig. 3.3. By contrast, the proposed learned predictor method can make spatially dependent predictions even in the absence of history or neighboring particles. Because

the training data contains artificially truncated trajectories, predictions can be made with trajectory lengths $n_t < T$. While accuracy may decrease in the absence of trajectory history, an estimate can still be made using only $n_t = 1$. For cases with spatially dependent velocities, this estimate is equivalent to estimating the mean flow field. In cases where particle position cannot be used to estimate velocity (such as swimming microorganisms), the model will implicitly predict a null velocity in order to minimize the error.

3.3.2 Standard Synthetic Shear Jet Flow

In order to facilitate comparisons of the performance of the proposed learned predictor and other particle tracking algorithms, we present results on a standard and freely available particle tracking dataset. The PIV standard images (PIV-STD) produced by the Visualization Society of Japan (VSJ) include ground truth particle locations and trajectories for a turbulent jet flow [136]. These data have been frequently used to evaluate the performance of particle tracking algorithms [27, 137, 138, 139]. The image set #301 is used to evaluate the proposed learned predictor here. This case is a 2D projection of the 3D jet shear flow and includes 145 images with an average of approximately 4000 particles. The maximum displacement is 10 pixels/frame with an image domain of 256×256 pixels leading to a displacement ratio of $p = 0.4$. Prior approaches have had differing levels of success on these images. The relaxation approach of Ohmi & Li [137] only tracks 20% of the particles in the first two frames, although this includes losses due to both the localization and tracking steps. Of the extracted links, 98% were correct. The variational approach of Ruhnau et al. [139] is able to extract 96% of the true links but requires over 700 tracking iterations per frame which introduces a substantial computational cost. The variational approach also assumes there is a global velocity field, which would not apply to particles moving independent from the surrounding fluid such as swimming algae. Unfortunately, open source implementations of these algorithms are not available so they cannot be compared to the trackpy implementation of the learned predictive tracker on other cases. However, it is worth noting that these tracking algorithms can include a prediction step which could be replaced with a learned predictor model to further improve their performance. The key contribution of this paper is the predictor itself which could be utilized by several tracking algorithms.

In addition to these literature comparisons, we compare the learned predictor to the Null and NearestVelocity predictors in trackpy. Note that the other predictors (Channel, MeanVelocity, Drift) are unsuitable for this case as the assumptions they rely on are not valid. The learned predictor is trained using an 80:20 split of the PIV-STD #301 dataset, with the first 29 frames used as the test set and the remaining 116 used for training. The learned predictor was able to extract 87% of the correct links while NearestVelocity was only able to extract 65% and the Null predictor extracted only 31%. This again demonstrates the improvement of the learned predictor over other predictive methods.

3.3.3 Experimental Channel Flow

To show that the learned predictor method can be applied to experimental flows without the need for additional experimentation, we present a reanalysis of data first presented by Toloui et al. [40] examining flow in a smooth-wall turbulent channel with DIH and validated with conventional PIV. The flow velocity is 0.6 m/s, the channel width is 50 cm. The centerline Reynolds number is $Re_c = 25000$ and the measured friction Reynolds number is $Re_\tau = 1750$. The recording rate is 3080 Hz ($\Delta t = 0.32$ ms) with a pixel resolution of 10.2 μm. A total of 3000 frames were recorded in 20 frame bursts. Further details on the experimental setup and hologram processing approach can be found in the paper. Figure 3.5a shows the flow facility used for the experiments while Fig. 3.5b shows a sample hologram illustrating the seeding density used for this experiment.

For this case, the experimental data is historical and there is no supplemental experiment available for training. To produce training data, we use the multi-pass tracking method [40]. This tracking approach consists of multiple passes tracking the particles and using a polynomial fit of the streamwise velocity with respect to the wall-normal position for prediction on the next pass. This tracking approach produced time-averaged velocity and Reynolds stress profiles matching those of PIV measurements. However, the mean trajectory length was only 5.3 frames compared to a video duration of 20 frames indicating that not all positions are linked. Manual evaluation also indicates that there are a small number of spurious links present. Improving this tracking will increase the resolution and accuracy of the velocity measurements. Additionally, the

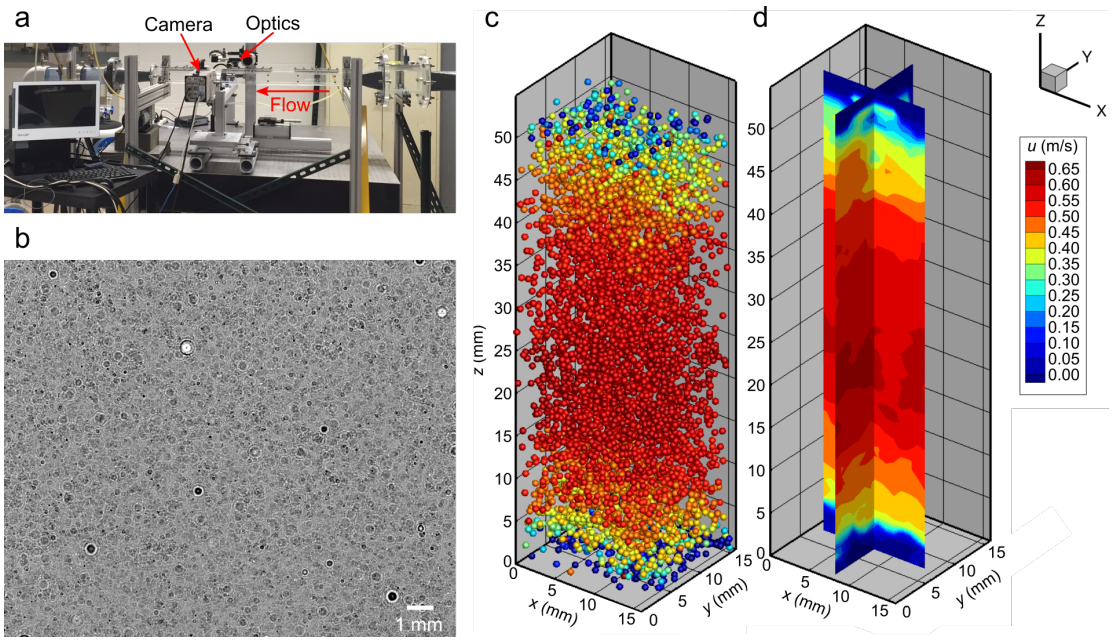

Figure 3.5: (a) The turbulent channel experimental flow facility. (b) A sample hologram illustrating the experimental seeding density. (c) Positions of each particle tracked in a single frame using the proposed learned predictor. Colors indicate the instantaneous streamwise velocity. (d) Slices of the instantaneous velocity field interpolated to a grid.

iterative nature of the multi-pass tracking approach means it is computationally expensive and the learned predictor should increase tracking speed. For training the learned predictor, the highest quality trajectories were selected with duration used as a proxy for quality. 10000 trajectories with a minimum duration of 15 frames were randomly selected from the data and randomly partitioned into train and validation sets with a 9:1 split. These trajectories were manually examined to ensure they contained no obvious linking errors and were representative of the spatial distribution of the particles.

The proposed method increased the total number of links by 31% compared to the prior multi-pass tracking approach. This directly leads to an improvement in the velocity vector spacing in the extracted flow field. The linking cost also improves; linking takes approximately 7.5 seconds per frame with the learned predictor while the multi-pass tracking requires 15 seconds per frame. An instantaneous flow field is presented in Figs. 3.5c and 3.5d after automatic outlier removal. The extracted particles are colored by their streamwise velocity in order to illustrate the velocity profile.

3.3.4 Experimental T-Junction Flow

When assumptions can be made about the flow (such as the channel flow assumption), simple models can be used to give reasonable motion prediction. Conventional linking methods are generally acceptable in these cases. However, more complex flows are challenging to model and would depend on user expertise to design an accurate model. On such flow is a T-junction where an inlet channel is split into two outlets (often with the same cross-section as the inlet and perpendicular to the inlet). Such flows occur often in nature and industry and have been studied experimentally and computationally [140, 113]. A key feature of these flows is the formation of twin vortices in the outlets. Thus, the flow is highly three-dimensional and difficult to model.

The T-junction used for this evaluation has a square cross-section with a 1 mm width and height. The flow rate is 1000 mL/hr corresponding to a bulk Reynolds number of $Re_b = U_b 2h/\nu = 290$ (where U_b is the bulk velocity, h is the half-channel width, and nu is the kinematic viscosity). Note that this is the same channel and flow channel and conditions as used in [88]. The illumination source is a HeNe laser (λ=632 nm) and a 5X microscopic objective (Mitutoyo, NA=0.14) was used to image the sample. The camera (NAC Memrecam HX-5) frame rate is 3000 Hz ($\Delta t = 0.33$ ms) with an image size of 1536×608 pixels and a calibrated magnified pixel size of 2.17 μm. The measured volume of the imaged region is 2.6 mm^3.

Training data for the learned predictor model is obtained using a supplemental experiment with the same experimental conditions but a lower seeding density. The low concentration data consists of 2000 frames with an average of 330 extracted particles per frame while the high concentration test data consists of 1300 frames with an average of 3600 extracted particles per frame. These correspond to displacement ratios $p = 2$ and $p = 1$, respectively. Thus, the simple Null predictor can be used to track the low concentration results but is unsuitable for the high concentration, necessitating the use of the learned predictor. Manually identified wall locations are used to normalize the extracted positions, reducing the impact of minor movement of the channel between the training and test experiments.

The learned predictor has superior performance on the high concentration test case compared to the other predictors. Because some ghost particles are extracted near the walls, a minimum trajectory length of five frames is used to remove spurious tracks.

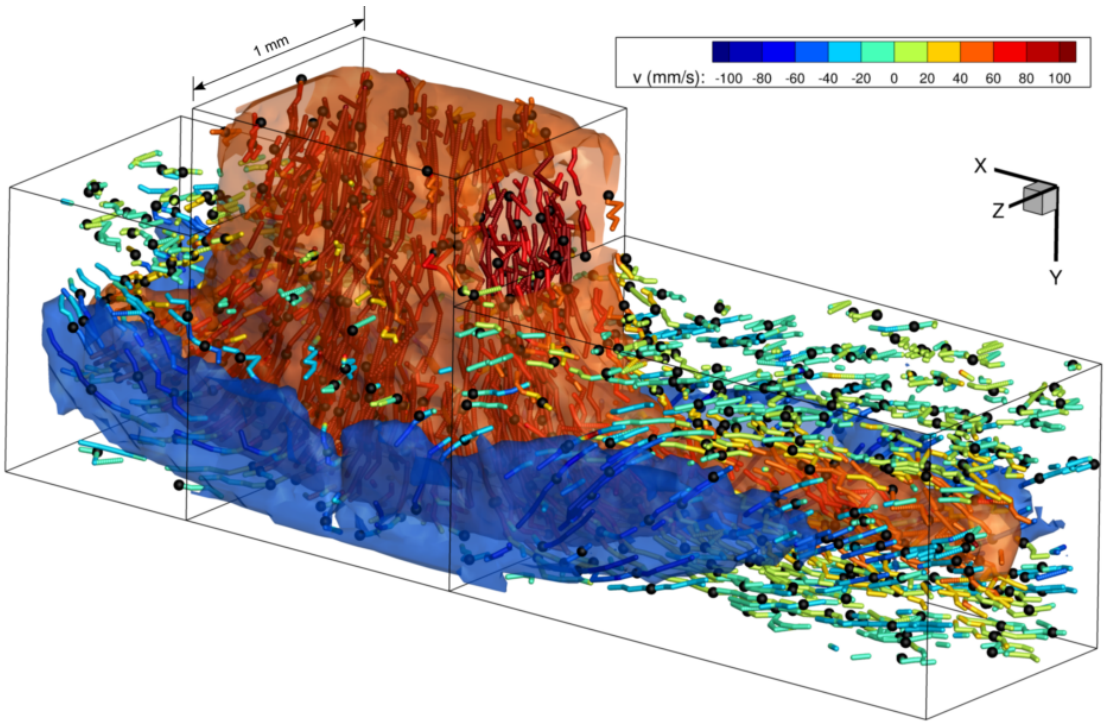

Figure 3.6: Visualization of the flow field and tracked particles in a T-junction. Black markers show the instantaneous location of particles. Trajectories are shown for a period of 10 frames and are interpolated. Colors of the trajectories and isosurfaces represent the vertical (inlet) velocity. The velocity isosurfaces are drawn at ±50 mm/s to illustrate the twin vortices which form in each outlet channel.

The learned predictor tracks an average of 600 particles per frame while the nearest velocity predictor tracks 370 particles per frame and the null predictor tracks only 93. Ghost particles near or outside the channel walls and trajectories lasting less than 5 frames account for the difference between the extracted and tracked particle counts. A visualization of the tracked particles is shown in Fig. 3.6 and a comparison to other predictors is given in Fig. 3.7. The instantaneous particle positions are shown as black spheres with the trajectories in a 10 frame window which are colored by the vertical velocity. For visualization, the trajectories were linearly interpolated. Note that some trajectories that appear short may not last the full 10 frames or may extend past the window limits. Isocontours of vertical velocity are computed using a 40 frame average velocity field. The isocontours show the expected twin vortices in each outlet arm. The

vertical position of the vortices changes with x; the vortex raises from the base of the channel towards the center with increasing x. This feature can be seen in the simulations of T-junction flow presented in [113].

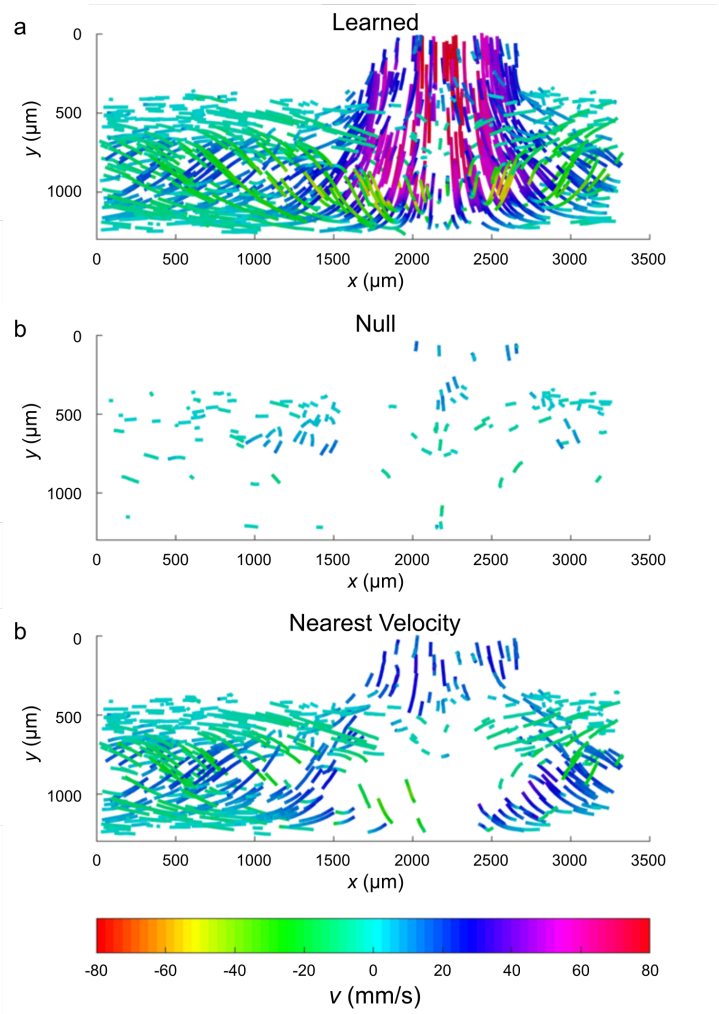

Figure 3.7: Visualization of the trajectories extracted using (a) the proposed learned predictor, (b) Null predictor, and (c) the Nearest Velocity predictor. The learned predictor clearly shows the most trajectories, especially near the higher-velocity inlet.

3.3.5 Experimental Swimming Algae

Finally, we present an application of PTV that is not related to flow measurements – that of quantifying the behavior of swimming microalgae. The green alga Dunaliella primolecta is known to produce lipids which can be used for biofuel production and recent work has shown that the lipid production can be correlated with changes in swimming behavior [127]. These studies are complicated by the high concentration of algal cells in the measured cultures which can exceed 4×10^6 cells/mL. Dilution of the sample risks altering the behavior of the organisms and decreasing the depth of the sample volume can also restrict their motion. Because of the variability inherent to biological studies, it is also desirable to have a large sample size (number of recorded cells) and record over a sufficient duration to ensure that the sample is representative. These factors lead to a large image size and moderate framerate such that increasing the framerate to reduce p may not be possible or desirable. Common assumptions used for flow tracking such as continuity, coherent motion of nearby particles, and a steady mean flow do not apply to this situation as the particles move independently and do not behave as flow tracers. Despite these difficulties, humans are able to identify the motion of individual cells even at high concentration, suggesting that a machine learning approach will be successful.

The data presented here are a subset of the data recorded by You et al. [127] who evaluated the change in organism behavior as the population size increased. Holograms were recorded at three different cell concentrations (approximately 9×10^4, 1×10^6, and 3×10^6 cells/mL). The mean swimming speed is 60 μm/s and the maximum is 120 μm/s – although the distribution is dependent on the concentration. The holograms are recorded with a Flare (2M360-CL) CCD camera at a rate of 20 Hz ($\Delta t = 50$ ms) and a 50 μs exposure. The image size is 1024×1024 pixels with a pixel size of 1.1 μm. The sample is illuminated with a spatially filtered and collimated 532 nm diode laser (CPS532, ThorLabs) and imaged with a 5X microscopic objective (Mitutoyo, NA=0.14). Samples of the cell culture are placed in a 1 mm thick glass cuvette for imaging and are recorded for a duration of 20 s. Holograms are processed using the RIHVR method [88].

For training, the null predictor is used, resulting in the trajectories used for the

prior study [127]. Trajectory duration is used as a proxy to identify the 1000 best trajectories which are randomly split with an 80:20 ratio into training and validation data sets, respectively. These trajectories are selected from all experimental trials regardless of sample concentration or other experimental factors. However, the tracks are biased towards the lower concentrations due to the tracking difficulty associated with the highest concentration case. Because the complex motion of the cells is only apparent for longer sequences, the history used for the model input (T) is set to 20 frames. In order to demonstrate the flexibility of the learned predictor to apply to 2D and 3D tracking, only the in-plane position components are utilized for prediction while velocity in the third dimension is assumed to be zero.

The learned predictor is evaluated on the highest recorded concentration of cells (3×10^6 cells/mL). Figure 3.8 shows the trajectories of cells passing through a small region of the full field of view with colors indicating unique trajectories. The full field of view is a composite of 10 frames after processing with RIHVR. Even though the displacement ratio in this case is not extremely low ($p = 3$ for 2D tracking), this case is difficult to track with traditional methods. This is because the high particle concentration makes the holographic particle extraction more challenging resulting in a higher rate of ghost particles and particles that are undetected for one or more frames. In order to obtain the long duration trajectories needed for behavior analysis (> 20 frames), the tracking algorithm must allow missing frames which increases the complexity. For further information on the behavior classification of individual trajectories, see Chapter 6 and the paper by You et al. [127].

Compared to the baseline assumption of zero velocity, the proposed method is able link 110% more objects. A manual assessment has shown that only 1% of these links are incorrect. The manual assessment examined 950 links in a region of interest (Fig. 3.8), finding 10 spurious links for a 95% confidence interval of $(0.5\%, 1.7\%)$. This represents a drastic increase in the number of objects that are tracked, leading to increased sample sizes for biological experiments. Additionally, the average length of trajectories increases by 25% from 38 frames to 47 frames (excluding tracks with < 20 frames), further improving the ability to classify the behavior of each cell.

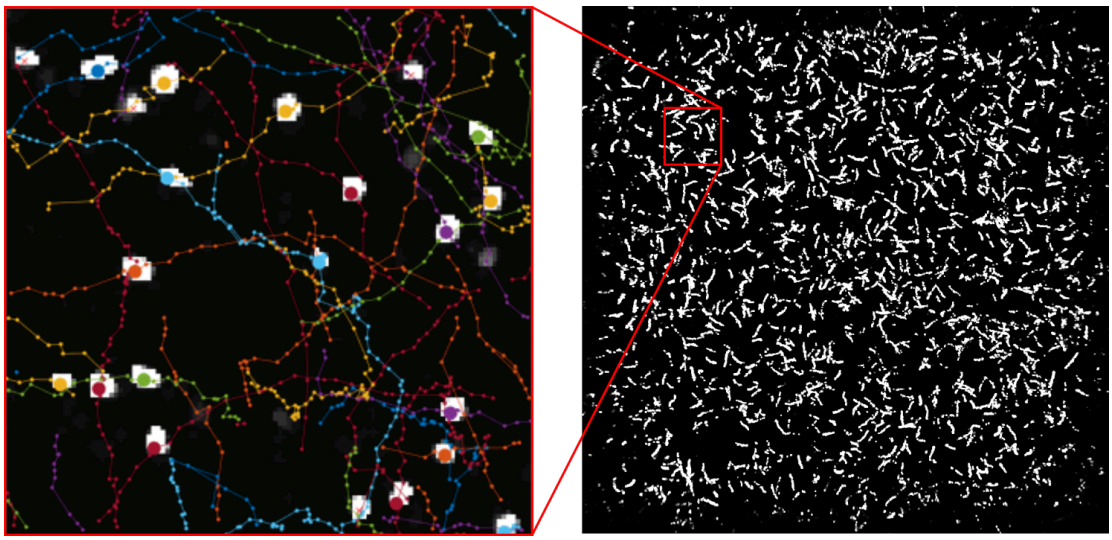

Figure 3.8: Plot of algal cell swimming trajectories. The full field of view (right) is shown as a 2D projection for a 10 frame duration. The inset (left) shows the unique trajectories (for the full 200 frame duration) passing through a small region of interest. The colored trajectories are superimposed on a grayscale image that is a 2D projection of a single frame from the sequence on the right. Colors indicate unique trajectories. The large colored markers indicate the detected particle positions at the current frame while small markers indicate positions at other frames. The grayscale (mostly white) shapes are the results of hologram processing and illustrate the size and shape of the tracked cells.

3.4 Conclusions

We have demonstrated a data-driven approach for learning a predictive model to aid in the particle linking task in particle tracking velocimetry. The method uses a simple LSTM model that is capable of learning to predict using the position and history of a particle. Simulations and experiments have demonstrated the capabilities of this method. Multiple approaches can be used to collect training data including prior methods which produce only partially complete results and supplemental experiments for which the linking problem is substantially simpler. In each of the validation cases, the learned predictor demonstrates superior performance compared to baseline methods in terms of the total number of linked objects and the accuracy of the links.

While not necessary for the cases presented here, performance could be improved

by including additional inputs into the model. For periodic flows it may be useful to include time or phase as an input. The motion of neighboring particles could also be included by appending the histories of neighboring particles to the input matrix. However, this would limit the extensibility of the model to different concentrations as the distance between neighboring particles would need to be the same in the training and target flows in order for the learned relationship to be valid. The learned predictor is most powerful when sufficient history is available, as in time-resolved measurements. However, it could be also applied to multi-pulse PTV which is often needed for high-speed flows [141]. In this case, the predictive model would primarily serve to learn the average flow field.

While we have presented applications utilizing digital inline holography, the proposed method could be applied to any other PTV method. In cases with complex flow and high tracer concentrations, the learned predictor can achieve superior performance without the need for substantial user tuning or assumptions.

Chapter 4

Implementation and GPU Programming

4.1 Introduction

Holographic processing is highly computationally intensive due to the large images and volumes used ($1024 \times 1024 \times 1024$ voxel volumes are common). Reconstruction also requires multiple Fourier transforms with a computational complexity of $O(N \log(N))$ where N is the number of pixels in the hologram. For iterative methods such as RIHVR, a MATLAB implementation could take more than one day to process a single hologram. Particle tracking velocimetry requires the processing and analysis of thousands of images. Thus, it is necessary to develop efficient implementations of the methods discussed in the preceding chapters.

Graphics processing units (GPUs) are a class of processor distinct from the more common central processing unit (CPU) in that the architecture is optimized for low latency, high throughput operations following a single instruction, multiple data (SIMD) structure that can often be used in image processing tasks. Elementwise matrix operations are examples of this sort of operation. The number of compute cores on a GPU is approximately two orders of magnitude higher than the number found in a typical CPU. For example, an Nvidia GeForce GTX1080 GPU has over 2500 processing cores compared to 4 cores in an Intel i7 CPU. This leads to speed increases of up to $100\times$ for some applications [8]. The CUDA parallel computing platform is an interface for the

C programming language to utilize GPU processing with Nvidia hardware. Nvidia provides libraries with efficient GPU implementations of many algorithms and operations including the three-dimensional fast Fourier transform (3D FFT).

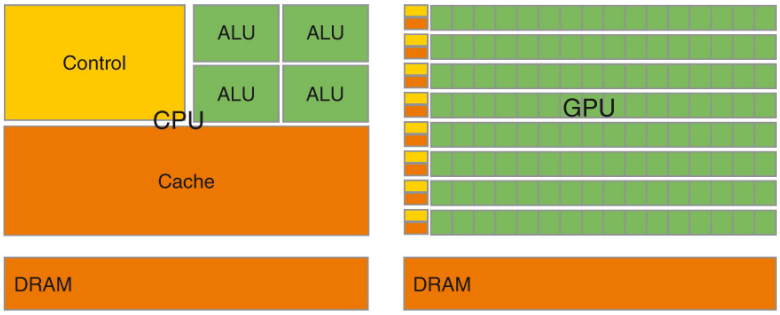

Figure 4.1: Architectural differences between CPU (left) and GPU (right). Image credit: Kirk & Hwu [8].

The GPU architecture (Fig. 4.1) is designed to optimize throughput of low latency operations by increasing the number of processing units (shown in green) and decreasing the space used for control and cache. Because of this, each gpu processor in a unit (warp) must process the same instructions at the same time, the SIMD structure. Thus, dynamic program flows (i.e. if statements, while loops) perform poorly on GPUs while simple local operations (those that only reference a single voxel or small neighborhood) perform well. The GPU (device) and CPU (host) do not share memory. As such, any substantial computations require explicit copying of data from the host to the device and vice versa. There is also an overhead associated with starting a GPU kernel function. A good algorithm will be designed to limit the amount of memory transferred between the host and device and reduce the number of kernel calls. However, even the best algorithm cannot eliminate these costs entirely. The result is that not all processes can be accelerated by a GPU and the load may dictate whether a GPU or CPU implementation will execute faster. The location where this tradeoff occurs will depend on the processing being performed and the hardware so it may be necessary to dynamically determine whether to process on the GPU or CPU depending on the local hardware and the size of the data being processed (e.g. size of a hologram or number of objects).

The use of GPUs to accelerate scientific applications has become increasingly popular

since the release of CUDA in 2007. However, most applications of GPU acceleration to holography are currently restricted to numerical reconstruction [142, 143, 144] and the creation of computer generated holograms [145, 146, 147]. Orzo et al did implement both reconstruction and segmentation on a GPU [148, 149]. However, their object detection and segmentation methods were primarily limited by the reconstruction step and little discussion is given to the details of how segmentation was implemented on the GPU.

Memory concerns play a critical role in determining the efficiency of GPU operations. Desktop GPUs such as the RTX2080 commonly have only 8 GB or less available device memory while the main RAM (host memory) can exceed 64 GB. Passing memory between the host and device is relatively slow and transfer time can exceed computational time if sufficient care is not taken. This is especially true for iterative operations where the same data may need to be accessed many times. When possible, it it best to store frequently accessed data on the device and only transfer to the host at the begining and end of processing.

4.2 Methods

4.2.1 RIHVR

Inverse methods similar to RIHVR (Chapter 2) have only been used to reconstruct objects for which the axial location is known either *a priori* or from a conventional reconstruction method. There have been no prior applications of compressive holography for DIH-PTV of flows containing thousands of tracer particles. The primary barrier preventing such application is the high computational cost. For illustration, we consider a case with 1000 particles per image and 100 images each sized 1024×1024 pixels with 1024 reconstruction planes (10^9 voxels). The best reported speeds for parametric inverse methods is approximately 4 seconds per particle, which would lead to a processing time of 4.6 days for our example [91]. A previous GPU-accelerated compressive holography implementation can reconstruct a volume up to $1024 \times 1024 \times 10$ voxels in 7.6 seconds (22 hours assuming a linear scaling to the size of our example) [97]. Other methods have much longer extrapolated times including 1000 days [95] and 400 days (on modern hardware) [90]. In addition to the time required for processing, memory requirements for CH place severe restrictions on the size of hologram that can be processed. Storage

of the hypothetical test case hologram would require approximately 8 GB to store in memory (complex floating-point values, 8 bytes each). Several additional variables of this size are needed for CH algorithms. However, contemporary GPU memory is limited to approximately 12 GB for consumer hardware and memory transfers from the GPU to RAM are slow. Therefore, current applications of CH must either limit the volume size to take advantage of the speed increase of GPU-acceleration or rely on the much larger RAM available on most desktop computers but use much slower CPU processing.

Because the FISTA optimization algorithm used in RIHVR is an iterative solution method, it requires a single hologram to be reconstructed hundreds or thousands of times before converging to the optimal solution. Therefore the computational time required to process a single image may be relatively high. PTV requires processing thousands of large, well-resolved volumes. Therefore, it is crucial to reduce the processing time to a manageable level to enable application to real flow studies.

A CUDA/C++ GPU implementation of the RIHVR algorithm is used to accelerate the processing. Key components already have efficient GPU library implementations. In particular, the fast Fourier transform (FFT) accounts for a substantial portion of the processing load for a CPU implementation and has already been optimized to run much faster on a GPU using the CUDA library. Most other RIHVR operations such as the reconstruction kernel and proximal operator largely use pixel-wise operations which are embarrassingly parallel and can readily be implemented using CUDA.

In order to circumvent the memory limitation, we exploit the sparsity of the ℓ^1 and FL regularized solutions to dramatically reduce the memory requirements. The coordinate (commonly, COO) sparse matrix format is used to store all volume data during iterations. The COO format stores the indices (row and column) and value for only the non-zero elements in a plane. Because data is accessed per plane for both the forward and reverse propagation as well as the 2D TV proximal operator, each plane is independently indexed. The total storage for each non-zero element is thus 24 bytes (8 bytes per index, 8 bytes for complex floating-point value) compared to 8 bytes per element for a non-sparse structure. Thus, memory usage should be reduced as long as the data sparsity (number of zero elements divided by total) exceeds 67%. Experience suggests that most PTV holograms have sparsity exceeding 99% [87, 71].

Some operations are not performed on the GPU either because there is insufficient

parallelization to make such an implementation efficient or because the CPU implementation does not account for a sufficient proportion of the execution time to justify the effort needed to create a GPU implementation. One such operation is the connected component labelling (CCL) step used to identify individual objects from a thresholded volume. Normal CCL algorithms are heavily serialized and thus inefficient on a GPU. Modifications can be made to allow for iterative parallel operation, although this may require redundancy in some cases. For example, a small object will require fewer steps to converge than a large one but efficient GPU utilization requires the same steps be performed on each. Extra complexity is presented by the use of the COO sparse storage format which means there are no library functions capable of performing this operation. Ultimately, while these issues could be resolved, the CCL step accounts for $< 5\%$ of the total execution time and improved efficiency in that operation alone will not produce significant performance improvements overall.

4.2.2 Machine Learning

Over the past decade, machine learning has become an increasingly popular tool for data analysis in applications as varied as predicting musical sequences [128] and medical image analysis [150]. Due to this extreme popularity, there are many tools such as Keras [132] and Tensorflow [151] that have been developed to facilitate the development and operation of these algorithms, particularly dense neural networks (DNNs). These libraries are highly optimized for high GPU performance. As such, minimal effort is needed on the part of the user when implementing these algorithms.

Part III

Applications

Chapter 5

Temperature Effects on the Migration of *Microcystis aeuruginosa*

The content of this chapter is the result of strong collaboration with Prof. Miki Hondzo and Jiaqi You and has been published in the Journal of Plankton Research [152]. Some aspects of this paper have been excluded from this chapter in order to avoid confusing the work of collaborators with that of the author. The contributions of the author relate to the construction, operation, and processing of the holographic microscope. The algae cultures were grown and counted by Jiaqi You. Content, including figures and text, has been duplicated with permission.

5.1 Introduction

Harmful algal blooms (HABs) have become significant worldwide problems in lakes and reservoirs influencing municipal, agricultural, and industrial water sources. HABs may result in damage to the ecological communities by causing deoxygenation leading to mass mortalities of fish and producing toxins that can pose serious health threats to animals and humans. *Microcystis* is a cosmopolitan genus of toxic cyanobacteria often present in eutrophic lakes which frequently dominates HABs and toxin production

within them [153, 154]. Water temperature is believed to play a roll in cyanobacteria blooms. Cyanobacteria are able to proliferate at high temperatures, out competing other species of algae during summer blooms [155]. Many prior studies have suggested that warming temperatures as a result of climate change could lead to an increased prevalence of cyanobacteria blooms [153, 156, 157]. Studies have indicated that *Microcystis* has a greater growth rate at higher temperatures [158, 153, 159].

Some *Microcystis* strains contain gas vesicles, enabling them to change their cell density and buoyancy to form blooms at different depths in the water column [160]. This helps *Microcystis* outcompete other algae by forming a thick layer on the surface, increasing its access to light while shading other species [161, 153, 157]. Studies (often simulations) exploring the vertical distribution of *Microcystis* have investigated the mechanisms used for buoyancy regulation [162, 163, 164, 165, 166, 167]. A few studies have examined the effects of temperature on the distribution of *Microcystis* colonies [164, 168]. However, these studies have not directly measured the buoyant velocities of individual colonies or measured the associated change in density. This study seeks to use a digital inline holographic microscope to directly measure the changes in buoyant or settling velocities of *Microcystis aeruginosa* colonies in response to changes in temperature.

5.2 Methods

5.2.1 Holographic Measurement

Holographic measurements were conducted at two different temperatures, $17.5 \pm 1.0°\text{C}$ for the cold experiment and $28.0 \pm 1.0°\text{C}$ for the hot experiment. The only experimental variable was the water temperature and all other environmental variables including the cell culture, light, and nutrient conditions were maintained constant. For the holographic measurements, water samples were collected in July 2016 from Powderhorn lake ($44°56'29.6''\text{N}$, $93°15'29.4''\text{W}$), an urban lake in Minneapolis, Minnesota. For each experiment, a culture sample of *Microcystis aeruginosa* (*M. aeruginosa*) was isolated manually from other organisms in the water and acclimated in an incubator at the test temperature for 24 hours prior to the experiment. The digital inline holographic microscope (DIHM) (see Fig. 5.1) consists of a Thorlabs CPS532 laser (4.5 mW with 3.5

mm beam diameter), an Azzota 1 mm Pathlength Optical Glass Cuvette with 0.35 ML volume, an Edmund Optics 5X M plan objective with 34 mm working distance and 0.14 NA, and a Mitutoyo 1X MT-4 tube lens connected to a Flare 2M360-CL camera with maximum image size of 2048×1088 pixels, 5.5 μm pixel size, 13 μs shutter, and a frame rate up to 337 frames/s (fps) at full sensor size. The laser wavelength (532 nm, green) was selected because the major pigments found in *Microcystis* have a low absorption at this wavelength, reducing the influence of the laser on the behavior of the sample [169, 170]. A T5 growth light system with two 24W bulbs (Milliard MIL-GLS24W2, 36 μmol/m^{2}s) was placed over the sample cuvette simulating the 14/10 hr day/night cycle. The culture sample was gently shaken for 30 seconds before a 0.3 mL sample was transferred to the cuvette. Images were recorded by a 1 TB Digital Video Recorder (DVR) Express Core (IO Industries Inc.) at a rate of 5 fps continuously for 10 minutes every hour, with each experiment lasting for 28 hours. Similar holographic systems have been utilized by Hong et al. [171] and Kumar et al. (2016)[58] to exam the behaviors of copepods and fruit flies, respectively.

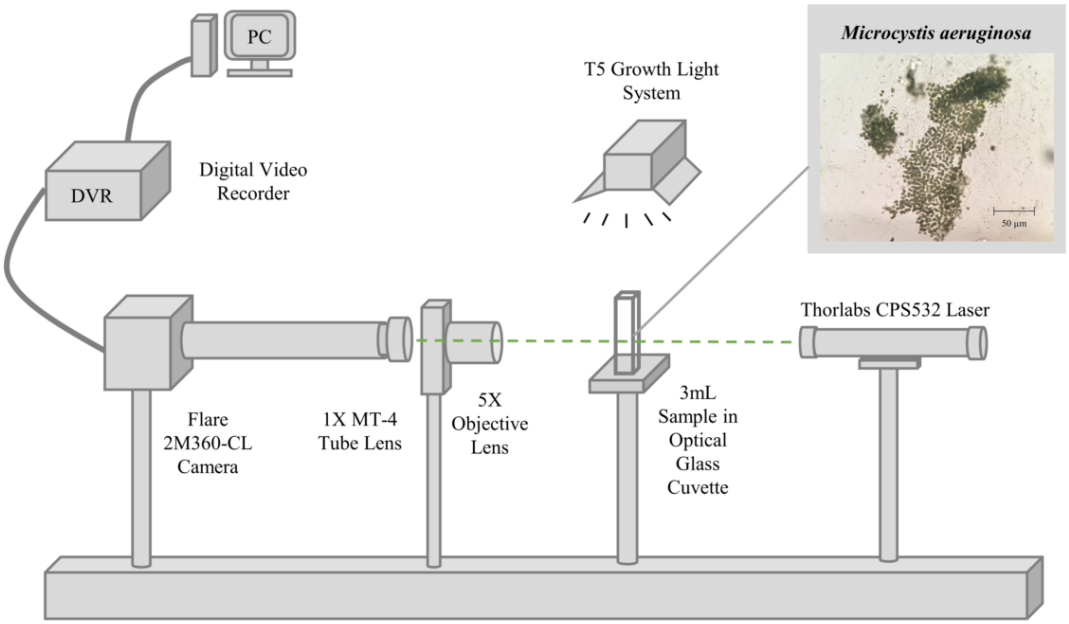

Figure 5.1: The digital inline holographic microscope setup

The recorded holograms were enhanced by dividing by the time-averaged background of each recording and normalizing such that the image contained 99.7% of the intensity information. The enhanced holograms are digitally reconstructed by convolving them with the Kirchoff-Fresnel diffraction kernel (Eq. 1.6). The projected images were thresholded using a constant threshold calculated as 60% of the mean threshold calculated using Otsu's method for a random subset of 100 images. Morphological filtering consisting of opening with a circular structuring element of radius 2 pixels followed by closing with an element of radius 5 pixels was performed to reduce noise. These sizes were selected based on the observed sizes of the projected *M. aeruginosa* colonies. Finally, the area and centroid of each connected component were extracted. The colony tracking was performed using the method of Crocker and Grier [110] to build trajectories from the centroids and find the average velocity for each colony. To further remove noise particles, only trajectories lasting for 20 seconds (i.e. 100 frames) or longer were included in the analysis.

5.2.2 Vertical Migration and Velocity-Density Model

The vertical migrations of *M. aeruginosa* colonies due to their buoyancy change during photosynthesis and biosynthesis were measured using the holographic microscope. The method used to model the vertical migration of the colonies was similar to that for modeling the settling velocity of particles except that the positive velocity direction is reversed. The use of this model and the analysis thereof was proposed by Jiaqi You. It is included here to provide context for the DIH measurements which were the author's contribution.

Modelling a *M. aeruginosa* colony as a sphere, the equation of momentum of a colony in quiescent fluid includes the gravity, buoyant force, drag force and an added mass term, which can be expressed as

$$\rho_{col} V_{col} \frac{dW_b}{dt} = \rho_{col} V_{col} g - \rho_w V_{col} g + \frac{1}{2} \rho_w C_D A_p W_b^2 - \rho_w C_m V_{col} \frac{dW_b}{dt} \tag{5.1}$$

where ρ_{col} is the colony density, ρ_w is the water density, V_{col} is the volume of colony, W_b is the buoyant colony velocity (upward vertical velocity), A_p is the projected area of colony, C_D is the drag coefficient, g is the gravitational acceleration, and C_m is the added mass coefficient ($C_m = 0.5$). In a moving fluid, relative colony velocity is given

by $W_r = W_b - W_f$ where W_f is the fluid downward velocity. Our DIHM set up was designed to minimize the W_f in the cuvette and therefore $W_f \approx 0$, which implies that $W_r = W_b$. Inspection of W_b over time revealed minimal change and therefore $\frac{dW_b}{dt} \approx 0$. Thus, Eq. 5.1 simplifies as

$$(\rho_w - \rho_{col})V_{col}g = \frac{1}{2}\rho_w C_D A_p W_b^2 \tag{5.2}$$

The drag coefficient depends on the particle Reynolds number ($Re_p = W_b D/\nu$, where D is the diameter of *M. aeruginosa* colony and ν is the kinematic viscosity of water) and is estimated in the results section after the velocity and sizes of the colonies are measured.

5.3 Results

5.3.1 Trajectories and Velocities

The spatial position data of each colony were obtained from the holograms and moving trajectories were tracked over time. Figure 5.2 shows the first 20 seconds of trajectories for experiments at hot and cold temperature respectively. To avoid noise and ensure accurate particle tracking, only the particles that have trajectories lasting for 20 seconds (i.e. appearing in 100 frames) or longer were selected. In total, 6579 particles for the hot experiment and 3453 particles for the cold experiment are plotted as trajectories. Since each of these trajectories is of the same duration, the physical length of the trajectory is a surrogate for the velocity. It is evident from Fig. 5.2 that the *M. aeruginosa* colonies in the high temperature (hot) environment (28.0 ± 1.0°C) exhibit higher velocities than those in the cold environment (17.5 ± 1.0°C). Mean vertical velocities of all the particles in each hour after the beginning of each holographic measurement were calculated and are shown in Fig. 5.3. The mean vertical velocity of *M. aeruginosa* colonies at the hot temperature is greater than colonies at the cold temperature all the time during the 28 hr measurement period, while the spread of velocities at the hot temperature is also greater than that at the cold temperature.

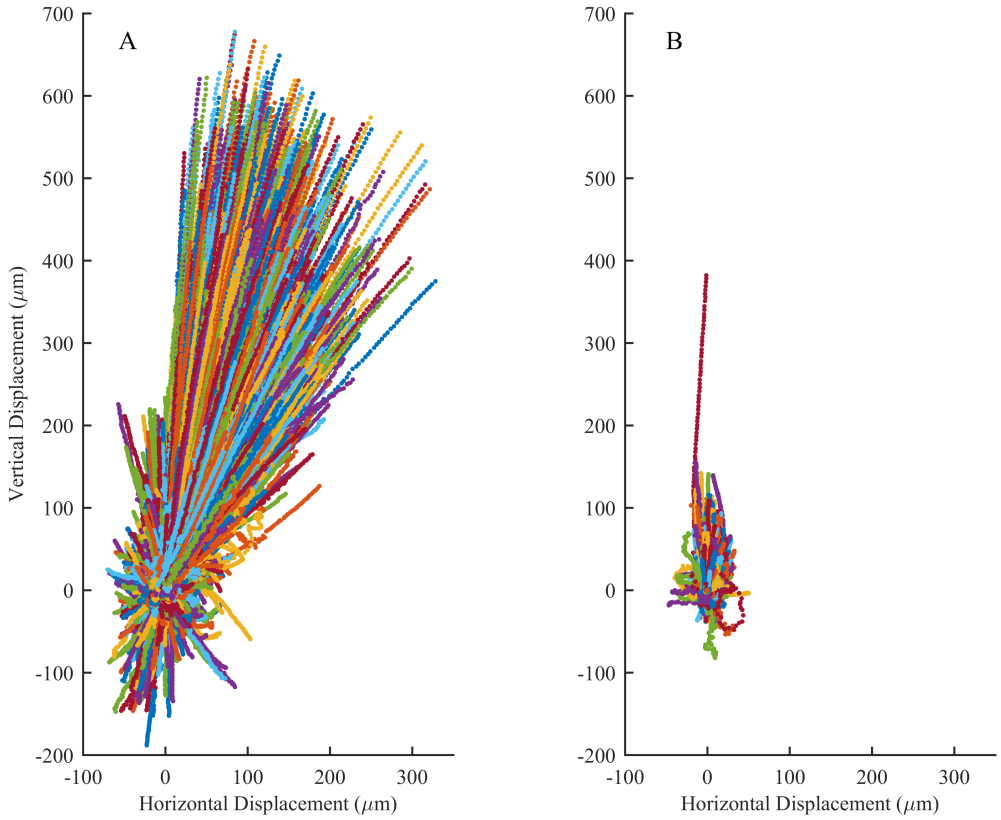

Figure 5.2: First 20 seconds of trajectories of M. Aeruginosa colonies at (A) hot temperature and (B) cold temperature. Only the particles with trajectories lasting for 20 seconds or longer were selected. The trajectories were normalized to the origin, and each trajectory represents a particles tracked in the holographic measurement.

5.3.2 Velocity-Density Model

The vertical velocities of *M. aeruginosa* colonies were averaged over all the data points in each experiment, which provides an averaged velocity for the cold temperature and one for the hot temperature. Projected areas for colonies estimated from the holographic measurement were converted to equivalent spherical diameters and averaged over all data points in each experiment. Using the averaged velocities and averaged areas, a typical Reynolds number of colonies was calculated to be $Re_p = \frac{W_b D}{\nu} \approx \frac{10\times10^{-6}\times20\times10^{-6}}{10^{-6}} = 2 \times 10^{-4} \ll 1$, indicating the particles are in the Stokes regime and the drag coefficient

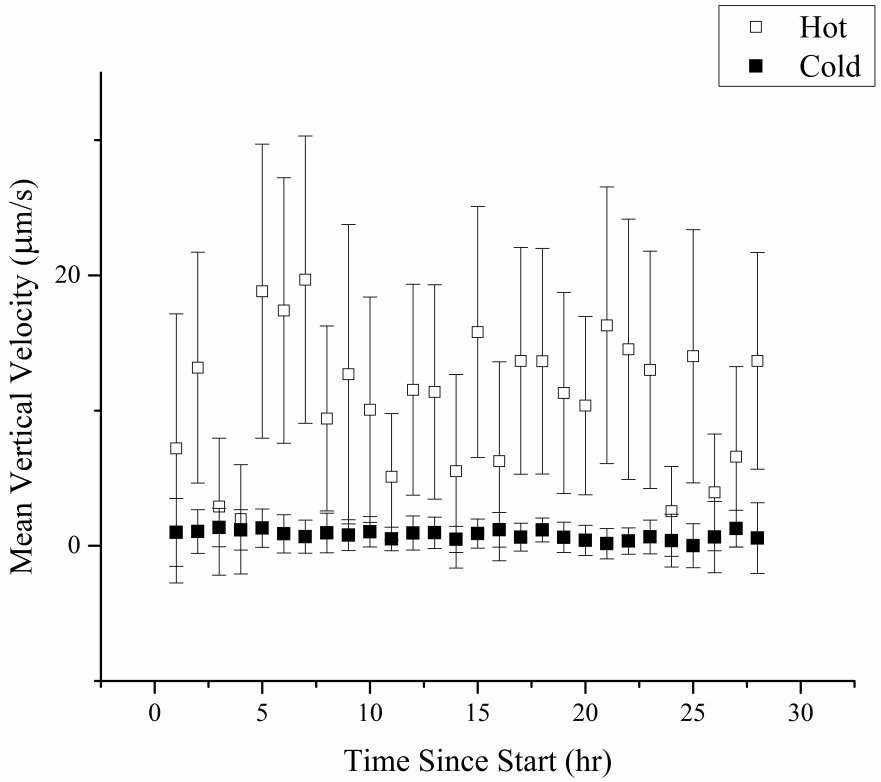

Figure 5.3: Mean vertical velocity of *M. aeruginosa* colonies in each hour from the start of holographic measurement for both hot and cold experiments.

in Eq. 5.2 can be substituted by $C_D = \frac{24}{Re_p}$. Eq. 5.2 then becomes

$$\rho_{col} = \rho_w - \frac{18 W_b \rho_w \nu}{g D^2} \tag{5.3}$$

Averaged densities of each colony for hot and cold experiments were calculated by substituting the averaged velocities and diameter into Eq. 5.3. The parameters and calculation results are shown in Table 5.1 for the hot and cold experiments, respectively. The density of colonies at high temperature is significantly smaller than that at low temperature, thereby leading to greater density difference between colonies and water. The colonies exhibit greater buoyancy due to density change in the hot environment than in the cold environment.

Table 5.1: Results of holographic measurements and conditions used for the velocity-density model

	T (°C)	W_b (μm/s)	A_p (μm^2)	D (μm)	ρ_w (kg/m^3)	ν (m^2/s)	ρ_{col} (kg/m^3)
Hot	28	11.853	312.305	19.946	996.174	0.8E-6	950.824
Cold	17.5	2.309	398.099	22.520	998.501	1.1E-6	989.953

5.4 Discussion

5.4.1 Movement Trajectories and Buoyant Velocities

The major vertical direction of the trajectories shown in Fig. 5.2 displays a deviation from the gravitational vertical direction, particularly in the measurements of the hot experiment. The deviation is due to circulation inside the cuvette, proven with additional measurements with a larger field of view using preserved *M. aeruginosa* cells (approximately neutrally buoyant) as flow tracing particles. These additional measurements also showed a very small speed (< 1 μm/s) of the tracing particles, indicating that the circulation has a minimal impact on the magnitude of colony velocities. The fan-like divergence of the trajectories is due to the geometry of *M. aeruginosa* colonies. The colonies are assumed as spherical particles while they are, in fact, irregular shapes ranging from flakes to ellipsoids. Each colony may have a trajectory departing from the reference axis (major direction), due to the theory of Stokes flow over particles in arbitrary shape [172].

In the hot experiment, 50642 out of 56179 colonies showed a positive buoyant velocity, while in the cold experiment, 44814 out of 56178 colonies showed a positive buoyant velocity. In other words, 90% colonies were floating during the hot experiment while only 80% colonies were floating during the cold experiment. This result agrees with the buoyancy recovery test run by Thomas and Walsby [168], which shows 84% recovery of non-buoyant colonies at 30°C and only 10% recovery at 7°C. The percentage difference is smaller in this study due to the smaller temperature difference. This also illustrates that the reason why *Microcystis* dominates summer blooming but starts sedimentation when autumn comes is due to worse buoyancy recovery at low temperatures.

Diurnal changes in depths, velocities, or colonial densities have been reported in

other studies [162, 163, 164], but are not shown in the results of this study. Mean velocities in Fig. 5.3 show no periodic patterns but some fluctuations in velocities at the hot temperature. One possible explanation is that the colonies were affected by more than one mechanisms of buoyancy regulation and thus were experiencing longer regulation periods. Since the experiments in this study lasted only for 28 hours, the colonies remained at the buoyant phase for the entire duration.

5.4.2 Colony Sizes

The average sizes of the colonies in this study are shown in Table 5.1. Compared to other studies, our measured colony sizes are relatively small. For example, Rowe et al. [173] reported median colony diameters of 117 μm while ours are only 20 μm. Critically, our samples are dominated by relatively small colonies, the presence of which could be caused by the methods used to sample and isolate the culture.

5.4.3 Colony Densities

The connection between rising velocity and colony density identified by this work is based on Stokes' Law. Prior studies have modelled buoyant cyanobacteria using this model [162, 163, 164, 165, 166]. Our results indicate that *Microcystis* colony density is dependent on the surrounding temperature. The factors related to buoyant velocity (Eq. 5.2) include colony size, fluid density, fluid viscosity, and colony density. In the absence of changes to the colony density, variations in the fluid density, viscosity, and the colony size could only lead to a ratio of hot to cold buoyant velocities of $\frac{W_{b,hot}}{W_{b,cold}} \approx 1.3$. The measured ratio is 5.1, indicating that a change in the colony density must occur at the different temperatures.

5.5 Conclusions

For the first time, we demonstrate that ambient temperature has strong effects on the buoyant velocities of *Microcystis*. The observations were enabled by the implementation of the digital inline holographic microscope which is low cost, highly compact, and a promising laboratory and field technology. DIHM can be readily integrated with

existing autonomous/robotic devices used in the field for long-term and large-scale in situ quantification of plankton distribution and behavior (see Chapter 7).

In addition to the DIH measurements discussed here, the effects of ambient temperature on the specific growth rate of *M. aeruginosa* were also evaluated through laboratory measurements. These measurements found that the specific growth rate increases with temperature up to the optimal growth temperature of 28.1°C. A cardinal temperature model with inflection is able to describe 95% of the variability of the *Microcystis* growth rate using temperature. Combined, the growth and density models will facilitate the prediction of *M. aeruginosa* growth and buoyant velocities at a variety of ambient temperatures in aquatic ecosystems.

Chapter 6

Swimming Signatures of *D. primolecta* as Indicators of Lipid Content

The content of this chapter is the result of strong collaboration with Prof. Miki Hondzo and Jiaqi You and has been published in Biotechnology and Bioengineering [127] where it was selected as the featured cover. Some aspects of this paper have been excluded from this chapter in order to avoid confusing the work of collaborators with that of the author. The contributions of the author relate to the construction, operation, and processing of the holographic microscope. The algae cultures were grown, maintained, and the chemical analysis performed by Jiaqi You. Content, including figures and text, has been duplicated with permission.

6.1 Introduction

Microalgae are currently farmed to produce compounds used for human nutrition and pharmaceutical products. They are also a promising potential source of biofuels due to their high lipid content. However, such biofuel production is often cost prohibitive in part due to the difficulty of identifying the optimal harvest timing for large-scale cultures [174, 175, 176, 177, 178].

Prior research has shown that lipid accumulation is tied to environmental stresses such as nutrient limitation [179, 180, 181, 182, 183]. Similarly, environmental stresses have also been shown to impact the motility of the algae. The green alga *Dunaliella* has different behavior in stagnant and moving fluids. As the flow rate increases, the swimming speed increases [184] and the cells align themselves preferentially with the flow [112]. Hansen et al. [185] showed that the swimming velocity of the alga *Chlamydomonas* increases under the effects of nitrogen starvation. Limited research has been done to directly correlate the swimming behaviors of individual cells with their lipid content.

The life-cycle of an algal culture consists of four phases: 1) initial lag growth; 2) exponential growth; 3) stationary growth as nutrients become depleted and the growth rate is limited; and 4) decline as the culture begins to die and the concentration decreases. These stages are indicators of the level of environmental and nutrient stress placed on the sample and are best identified by observing the change in cell concentration of the culture over time.

This work seeks to identify a correlation between the growth stage, lipid content, and behavior of the algal cells. DIH-PTV is used to analyze cell behavior as it provides a means to non-invasively record the 3D motion of the cells.

6.2 Methods

6.2.1 Strain Selection

The green alga *Dunaliella primolecta* (*D. primolecta*) was chosen for this study due to its high lipid content, high salt tolerance, and the amount of prior work studying this organism. *D. primolecta* is a bi-flagellated unicellular green algae with a lipid content ranging from 15% to 40% [186, 187]. The cell size is approximately 5 μm.Cultures were created with three different initial nitrogen contents: 30%, 70%, and 100% where percentage is relative to the standard content of Erdschreiber's medium. Cultures were grown in an incubator at 20°C with a 14/10 hour day/night cycle. Trial experiments were performed to identify the timing of each growth stage.

6.2.2 Chemical Analysis

In addition to the DIH-PTV measurements of cell behavior, other measurements performed by Jiaqi You were used to quantify the lipid content of the cultures. While these measurements are not the subject of this thesis, they are important for interpreting the DIH-PTV measurements. A more detailed description of the procedures can be found in the paper by You et al. [127] and the associated supplemental material.

The dry cell weight and nitrate concentration were measured for samples collected from replicate cultures at each of the initial nitrogen concentrations. The dry weight was measured by filtering the samples and weighing the filtered solids after drying in an oven. Nitrate was measured using a fluorometer and nitrate test kit.

Measurement of the intracellular neutral lipid content was performed by first staining the cells with Nile red dye. The fluorescence of the stained samples was measured using a multi-mode reader and normalized by the cell concentration. The gravimetric method adapted from Bligh and Dyer [188] and Alonzo and Mayzaud [189] was used to calibrate the Nile red fluorescence measurements.

6.2.3 Tracking of Swimming Trajectories

The swimming trajectories of *D. primolecta* were recorded using a DIH-PTV system consisting of a 532 nm diode laser (Thorlabs CPS532), an optical spatial filter and collimating lens assembly, 5X microscopic objective (Mitutoyo 10X/0.14 NA), and a CCD camera (Flare 2M360-CL) (Fig. 6.1). The holograms were recorded at a framerate of 100 Hz with an exposure time of 50 s and cropped to a 1024pixels $\times$ 1024 pixels window for processing. Measurements of replicate 30%N cultures were performed at the lag, exponential, and early stationary phases. Recordings of five samples were made for each culture with recording volume of 1 μL. Each sample was recorded for 20 seconds (2000 frames) with the exception of the lag stage samples which were recorded for 60 seconds in order to increase the total number of cells recorded at the lowest concentration. Positions of each cell in the recorded hologram were extracted using the Regularized Inverse Holographic Volume Reconstruction (RIHVR) method presented in Chapter 2. The cell positions were tracked in time using the method of Crocker and Grier [110] to produce trajectories illustrating the swimming mode of each cell.

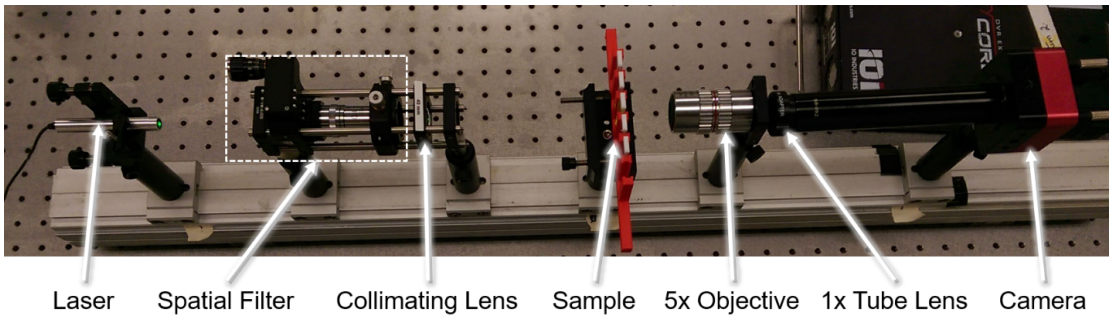

Figure 6.1: The DIH-PTV system used for analysis of *D. primolecta* swimming signatures

The swimming trajectories were classified into five behavior modes: 1) circular which rotate about a fixed point with minimal net motion; 2) helical which rotate about a moving point, forming a helix; 3) random walk which do not rotate and have minimal directionality; 4) linear which have no rotation and minimal deviation from a principle direction of motion; 5) meandering which is similar to linear but with greater deviation from the principle direction. The trajectories were automatically labeled using a binary decision tree based on a set of measured trajectory features.

To determine the significance of differences in the swimming behavior among growth phases (the lag, exponential and early stationary phases), one-way ANOVA tests were conducted for the swimming speed and fine motion frequency from the DIH-PTV results ($df = 2, \alpha = 0.05$). Similar tests were conducted to determine the statistical significance of differences in the neutral lipid content at different growth stages and with different initial nitrogen content.

6.3 Results and Discussion

6.3.1 Intracellular Neutral Lipid Content Accumulation

The intracellular neutral lipid content of *D. primolecta* was observed to be correlated with both the growth stage and the initial nitrogen content (Fig. 6.2b). For the 30%N cultures, the lipid content increased drastically and peaked in the early stationary stage (day 25), followed by a decline in the late stationary stage. By comparison, the 70%N and 100%N cultures peaked at the end of the measurement in the late stationary stage

and had a substantially lower peak lipid content than the 30%N cultures. This demonstrates the need for precise harvest timing as a delay of only a few days could lead to a 50% reduction in the yield.

6.3.2 Microalgal Swimming Speed and Trajectories

Measurements of the swimming velocities of *D. primolecta* using DIH-PTV showed that the lag phase has the lowest mean swimming speed, with increasing speeds seen in both the exponential and early stationary stages. There was no significant difference in speed among the three nitrogen levels for the lag or exponential phases. These results are consistent with supplemental experiments performed using traditional micro-PTV. Swimming trajectory measurements using DIH-PTV indicate a change in the complex behavior modes of the swimming cells (Fig. 6.3a-c). We observed five swimming modes including circular, helical, random walk, meandering, and linear. These can be further grouped into fine motions (circular and helical) and gross motions (linear and meandering) with random walk serving as an intermediate that is neither fine nor gross. We trained a binary decision tree to autonomously classify the measured trajectories into one of these classes and applied this classification to $n = 421$ trajectories from the lag phase, $n = 6306$ from the exponential phase, and $n = 7874$ from the early stationary phase. The most significant trend is the decrease in the frequency of fine motions from exponential to early stationary phase (Fig. 6.3d-f). The helical and circular behaviors are hardly seen in the early stationary stage. The fine motions account for 48% of tracks in the lag phase, 16% in the exponential phase, and only 2% in the early stationary phase.

6.3.3 Link Between Lipid Accumulation and Swimming Signatures

The changes of swimming modes identified from the *D. primolecta* swimming trajectories correspond to the intracellular neutral lipid content changes across growth phases. The statistical one-way ANOVA results indicate that the percentage of cells exhibiting fine motions are statistically different at each growth phase ($\alpha = 0.05, P < 0.01$). The variation of swimming behaviors across growth phases could be associated with the nutrient availability and chemotaxis of microalgal cells. The nutrient distribution

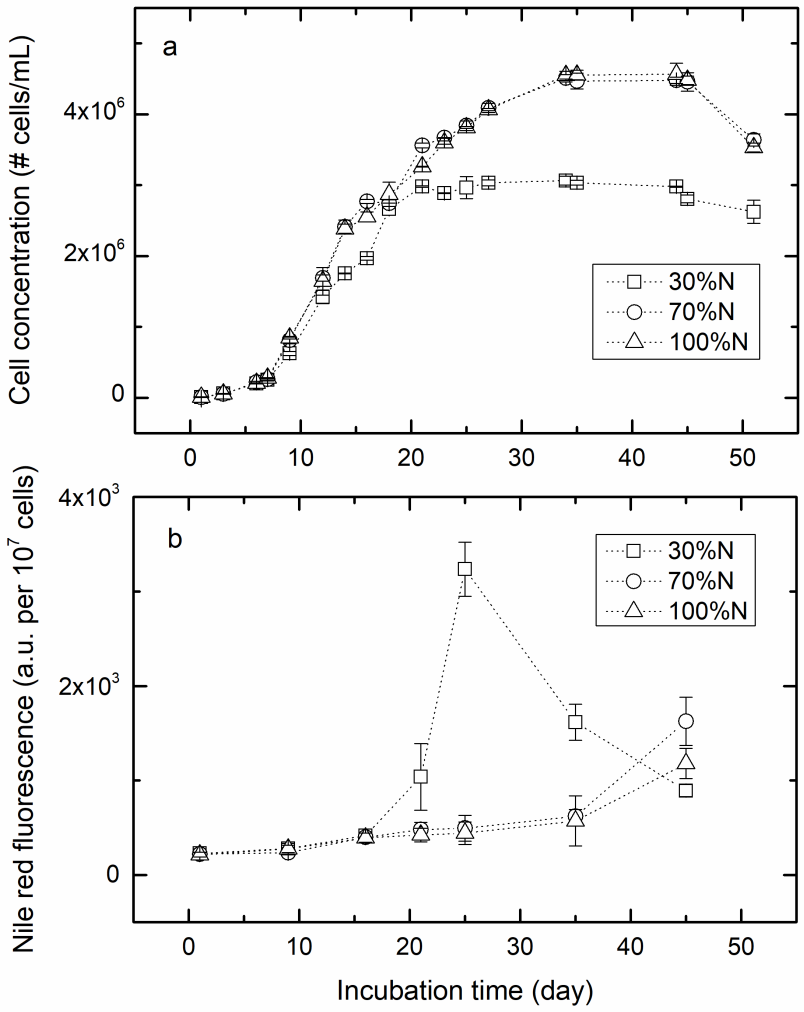

Figure 6.2: Growth curves and intracellular neutral lipid content of *D. primolecta cultures*. (a) Cell concentrations of an entire growth cycle of the three groups of cultures (b) Intracellular neutral lipid content as measured using Nile red fluorescence for the growth cycle of each culture. Image credit: Jiaqi You

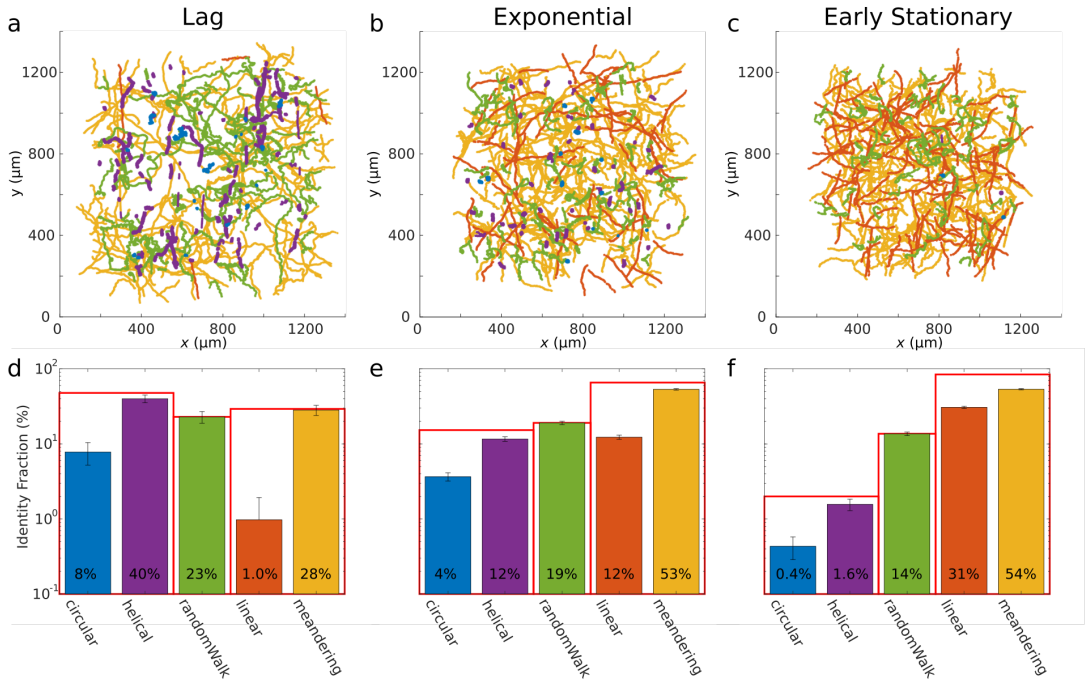

Figure 6.3: Classified swimming trajectories of *D. primolecta* cells in 30%N cultures. (a)-(c) Selection of n=400 random trajectories from each of the three stages measured with DIH-PTV. Trajectories are colored according to their assigned behavior mode. (d)-(f) The frequency of each behavior mode for each of the growth stages.

in the growth environment is hardly homogeneous – nutrient patchiness forms for many reasons. Chemotactic response of *Dunaliella* cells to the ammonium and several amino acids have been reported [190]. Akin to the run-tumble transitions of bacterial chemotaxis [191], the cells move towards a nutrient patch through the gross (linear and meandering) motions while remaining in the patch to utilize the nutrients through the fine (helical and circular) motions. At early growth phases, the nutrients are sufficient, so the frequency of fine motions is high since the shorter net displacement of helical and circular motions allow the cells to maintain in a nutrient-rich region for a longer time and maximize their nutrient uptake. When photosynthesis is limited by low local nutrient availability, the algal cells tend to become positively chemotactic which makes them travel faster in linear/meandering motions towards certain attractants [192]. At the stationary growth phase, the fine motions are significantly reduced due to nutrient scarcity and most of the cells exhibit larger net displacement with the gross motions to

explore potential nutrient sources.

The reduction of the fine motions corresponds to the accumulation of intracellular neutral lipid content as both are induced by the nutrient limitation. When the lipid content peaked in the early stationary phase, the fine motions were hardly seen. There were approximately 8-fold differences in both the fine motions and neutral lipid content between the exponential and early stationary phases for the 30%N cultures. The strength of transition suggests that the relative frequency of behavior modes could be a potential indicator for the growth phase, and by association the neutral lipid content.

6.4 Discussion and Conclusions

Our findings of the association between microalgal swimming signatures and intracellular neutral lipid content inspire a low-cost scalable sensor system utilizing DIH-PTV for high-throughput monitoring of the neutral lipid content in industrial-scale biofuel production. Such a system would improve control of cultivation conditions and harvest timing of microalgae, leading to a substantial biofuel yield and low-cost algae-based biofuels. Conventional methods for intracellular neutral lipid determination, such as lipid separation by column or thin-layer chromatography, fatty acid profiling by gas chromatography, and fluorometric determination of neutral lipids by Nile red / BODIPY [193, 194, 195, 196, 197], either require tedious extraction and/or transesterification work and expensive equipment, or test only small volume samples which are less representative for large-scale cultivations. In contrast to current lipid measurement methods, DIH-PTV has much higher throughput and better scalability. DIH sensors are low cost, small, and easily integrated with other instruments so that a network of DIH sensors could monitor multiple sites efficiently in open ponds or closed photo-bioreactors for industrial-scale biofuel production.

Exploiting microalgal swimming signatures as a possible indicator in microalgal growth and intracellular neutral lipid accumulation monitoring will potentially influence the pipeline of microalgal biodiesel production by enabling more optimal harvest timing and control of cultivation conditions.Our results showed a 3.6-fold increase in the intracellular neutral lipid content within only three days. The neutral lipid content at the early stationary phase is 20 folds higher than that at the exponential phase and

4.7 folds higher than that at the late stationary phase. Since lipid production is very sensitive to harvest timing, utilizing the drastic decrease of fine motions and increase in swimming speed to predict the timing of maximum neutral lipid accumulation can potentially enable more optimal harvest timing. This timing will also reduce the cost of consumables (including water, nutrient supplies, and electricity), which are some of the most substantial costs in biofuel production [198]. This can lower the net cost per unit biodiesel production, which is a major bottleneck inhibiting commercialization [199, 198].

These factors will together decrease the net energy ratio (NER, the energy input in cultivation and refinement divided by the energy output from the biomass), which is an indicator of environmental sustainability and the overall energetic effectiveness of the biodiesel production [177]. Achieving a lower NER will make microalgal biodiesel production more economically competitive. Besides reducing the net cost per unit biodiesel, the higher biomass and lipid yield can also result in increased beneficial by-products from the lipid extraction and transesterification processes. Appropriate use of the remaining biomass for animal feed, ethanol, or biogas, and glycerol for human nutrition, pharmaceutical applications, or personal care will contribute to the commercial viability of microalgal biofuel production [200, 201, 202]. Overall, exploiting swimming signatures in a low-cost scalable sensor system for inline high-throughput monitoring of microalgal growth and neutral lipid accumulation will potentially lead microalgae-based biofuel production to a more cost-effective and energy-effective future.

Chapter 7

Robotics

The content of this chapter is the result of collaboration with Prof. Nikolaos Papanikolopoulos and Dario Canelon. This work has been posted on arXiv [203] and is under review for publication. The elements of this chapter relating to the DIHM sensor are the contributions of the author while the development and operation of the Aquapod robot was contributed by Dario Canelon.

7.1 Introduction

Aquatic environments are challenging to monitor. Large-scale disasters such as the Deepwater Horizon oil spill or harmful algal blooms (HABs) [10] can cause millions of dollars of damage annually. While these contaminants can spread for kilometers, microscopic scales are also critically important. HABs often consist of algae such as *Microcystis aeruginosa* which has a colony size on the order of 100 μm [173]. Oil slicks can be broken into micro droplets by rain and diffused by turbulence [204]. For both HABs and oil spills, detection of these microscopic particles could enable early detection or improved mitigation of these disasters. However, the volume of water that must be monitored is vast; an optimal system must be able to perform microscopic measurements over many kilometers and thousands of liters. Furthermore, the timescales involved are relatively short with HAB formation occurring on time scales of one week or less [37, 35, 36]. Similar challenges arise when detecting waterborne parasites [5] or invasive species [205]. Rare species detection could also be applied to extraterrestrial exploration

[6].

Current methods for measuring lacustrine and marine particulates are unable to measure across a wide range of length scales, are restricted to small regions of the environment, often cannot differentiate between similar classes of particles, or may not have the sensitivity required for early detection. There are often trade-offs requiring the synthesis of data collected with multiple techniques in order to obtain conclusive results. For example, Wilkinson et al. [37] monitored HAB formation using a long-term research station augmented with more precise collection or physical samples for laboratory analysis. Remote sensing [35, 36] is suitable for large-scale mapping of dense concentrations but has limited spatial and temporal resolution, poor sensitivity, and cannot penetrate deep below the surface. Fluorometers are often used to measure chemical components such as chlorophyll and phycocyanin which are used as proxies for biomass concentration [37]. However, these measurements are insufficient for identifying individual species and are highly dependent on the quality of their calibration. Physical sampling for laboratory analysis is still the gold standard measurement technique but is expensive, time consuming, and often infrequent.

We present a novel system that allows the *in situ* measurement and quantification of various environmental particulates at both the small scales required to measure or identify individual particles (i.e. 1 μm) and also at the much larger scales of the body of water (i.e. 1 km). The system (Fig. 7.1) consists of a digital in-line holographic microscope (DIHM) integrated with an autonomous amphibious vehicle – the Aquapod – in order to make high resolution measurements including particle size, concentration, identification, and three-dimensional motion as the Aquapod moves throughout a large environment of interest. We discuss the design of the DIHM in Section 7.3.1, placing a particular emphasis on decreasing the cost of the system and addressing challenges such as the vibrations to the sensors as the robot propels itself. In section 7.3.2 we present a machine learning model that enables real-time on-board processing. Section 7.3.3 covers the Aquapod robotic platform as it pertains to this work. In Section 7.4 we describe and discuss two experiments that were carried out as laboratory validation of our methods and in-field testing of our system. Finally, in Section 7.5 we conclude possible avenues for future research using this system.

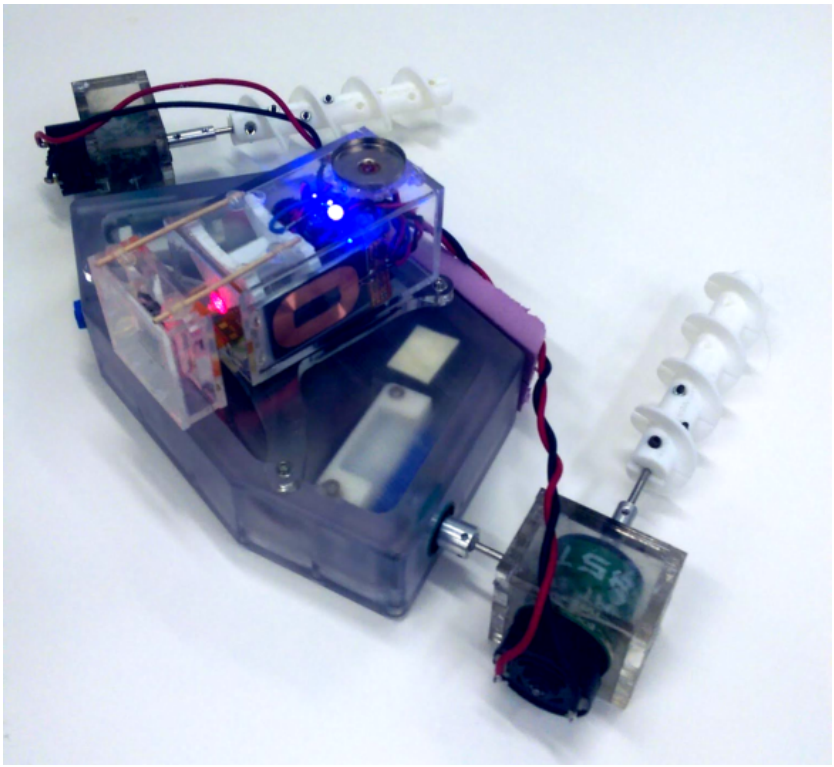

Figure 7.1: DIHM mounted on the Aquapod prior to deployment.

7.2 Background and Related Work

Employing robotic platforms to move sensors into desirable measurement locations is frequently being looked at as a way to gather data in a wider range of scenarios, better understand and gain insight on the environment through distributed and scalable deployments, and augment human capabilities by leveraging automation in tasks that were not previously feasible. In events such as the Deepwater Horizon oil spill [206] and the Fukushima nuclear disaster [207], robotic platforms have permitted environmental monitoring and the completion of vital tasks while reducing the need to place human resources in danger. In the case of environmental monitoring, the long-term objective is to deploy a number of robots to carry out sensory tasks in an automated fashion, sometimes spanning days or weeks, with occasional human interaction for maintenance or supervision.

In some cases, researchers have turned to robotic systems to deploy highly specialized

and specific sensors to strategic locations to optimally gather data of the underlying physicochemical properties of the environment [208]. Utilizing small mobile platforms that integrate proportionately smaller sensors allows the active collection of information in a way that is not available by laboratory testing of samples or by stationary sensors. Furthermore, active sensors that process data *in situ* permit a live data feedback loop to more intelligently deploy resources and gather the needed data in a more efficient and accurate manner [208].

Greenfield et al. have developed a robotic platform to perform laboratory-type measurements of algae in the field [209]. This special machine, called the Environmental Sampling Processor (ESP), is a marine surface vessel which concentrates and filters physical samples, then utilizes DNA probing to perform tasks such as species identification and particulate concentration.

Many robotic systems utilize sensors that are highly specialized to the particular task such as DNA probing. Scattering-based particle sensors such as many turbidity sensors and fluorometric cytometers utilize the spectra of light scattered from a single point and thus lack the spatial information inherent to an imaging method. They measure quantities averaged over the sample volume and are unable to quantify microscopic heterogeneity. The reduced sample volume necessary for these methods often requires some microfluidic sampling which may bias the sample composition, size distribution, or behavior in a way that ideal *in situ* methods should not. Furthermore, these methods require careful calibration to account for the variations in scattering properties of different samples and often require high sample concentrations to achieve a measurable signal. Optical microscopes are well suited for particle identification and counting as a trained operator (or algorithm) can perform these tasks directly from the recorded images without any need for calibration. However, the limited depth of focus of conventional microscopes means that they are limited to 2D measurements, limiting the measurement volume and requiring mechanical sampling. In cases of rarefied samples, a very large sample volume may be necessary to detect the objects of interest. Such situations may occur in the deep ocean or in extraterrestrial environments. 3D microscopy techniques such as scanning confocal microscopy require a complex mechanical scanning mechanism and often require sample preparation via chemical staining. In addition to the mechanical complexity, scanning methods are unsuitable for measuring dynamic

samples that change faster than the scanning speed.

A promising sensor is the digital holographic microscope (DIHM) which uses an imaging technique that records optical interference patterns which can be digitally refocused to produce a 3D image of microscopic objects from a single 2D recording. A DIHM can be used for species identification [5], sizing [13], and particle tracking [1]. The biggest advantage of holography over other imaging techniques such as traditional microscopy is that standard microscopes are limited to a narrow depth of focus (1 μm) while holography is capable of refocusing over a much wider volume (1 cm). This substantially reduces the impact of the sensor on the fluid being measured and allows for a larger sampling volume, ensuring representative samples even under low concentration conditions. DIHM requires no moving parts, can image at high speeds, and is non-destructive and non-invasive making it a very powerful measurement technique for *in situ* studies. Figure 7.2 shows a comparison between microscopic and holographic imaging of colonies of *M. aeruginossa*. The reconstructed in-focus image (Fig. 7.2d) generated from the recorded hologram (Fig. 7.2c) shows that the individual cells within a colony can be detected.

There have been numerous previous applications of holography for underwater measurements in the past two decades [210, 211, 212, 3, 4]. Talapatra et. al. [3] used a free-drifting submersible holographic device to measure the size and spatial distribution of particles in a 15 m water column. They also simultaneously measured the mean shear strain and turbulence dissipation rate by tracking the imaged particles. However, while the submersible was able to ascend, descend, or drift in a water column, it was designed to be tethered to a boat, and required offline *post hoc* processing and analysis. Deployment of a DIHM from oceanographic vessels has been described by several authors [213, 15, 211], though these experiments lacked substantial automation.

Deep sea holographic microscopes are sold commercially by 4Deep Inwater Imaging and Sequoia Scientific. Both systems produce high quality holograms and are capable of particle sizing, counting, and morphological species recognition at depths of over 100m. Despite their utility, the large size (over 70 cm long), weight (7-27 kg), and cost (40,000 USD) of these systems limit potential applications. Both the size and cost are driven by the need to be waterproof at great depths (>100 m) and acquire very high SNR holograms. In most freshwater applications, it is not necessary to image at depths

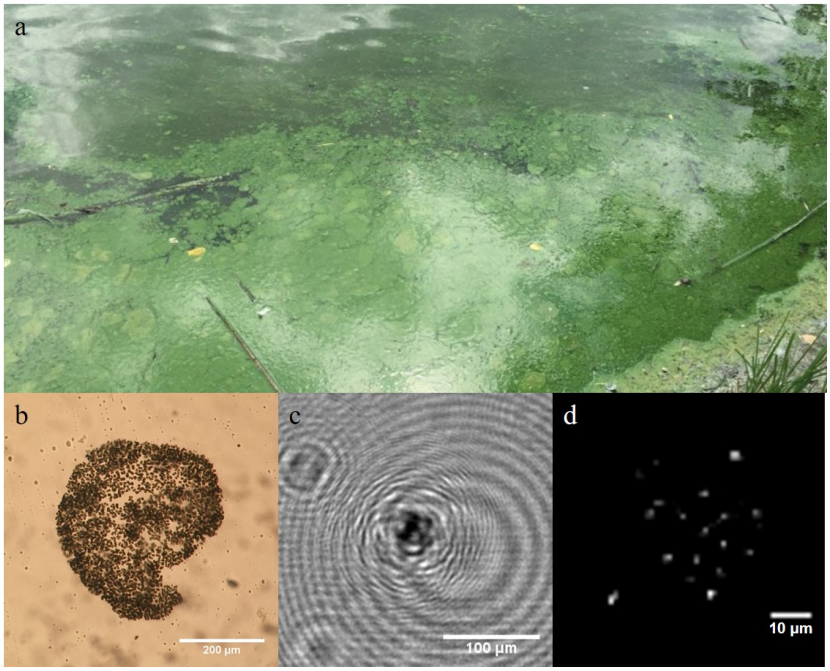

Figure 7.2: (a) Macroscopic image of HAB in Powderhorn Lake, Minneapolis, MN. (b) *M. aeruginosa* colony sampled from (a) and imaged using 400x optical microscope. (c) Recorded hologram of *M. aeruginosa* colony using a laboratory DIHM. (d) In-focus image of (c) processed using the methods of this paper showing that the colony is comprised of individual cells. Photo credit: Jiaqi You.

greater than 5 m as most microorganisms tend to live at shallower depths [37]. There have been no demonstrations of a low-cost miniature DIHM for *in situ* measurements.

In addition to the *in situ* applications, laboratory studies have shown the power of DIHM as a measurement technique. High speed DIHM can be used for particle tracking velocimetry (PTV) [1] which has applications in both flow measurement and behavior analysis. Holography has been used to examine the changes in the complex swimming behaviors of dinoflagellates in response to the presence of prey [214]. Other behavioral studies have examined the near-wall swimming behavior of bacteria [51] to relate swimming patterns to the local fluid vorticity [184]. DIHM has also been applied to automated detection and classification of organisms. El Mallahi et. al. [5] trained a support vector machine (SVM) classifier to automatically identify *Giardia labmlia*, a

waterborne parasite. Göröcs et al. [61] developed a low-cost microfluidic holographic cytometer for automatic classification of plankton samples. However, their device requires sampling from the environment. Sampling from frozen sea ice, Lindensmith et. al. [6] used a holographic microscope to detect life in the samples with proposed applications in extraterrestrial exploration.

To our knowledge, there has been no previous integration of a DIHM with a robotic system. This represents a major opportunity to leverage the powerful 3D microscopic imaging capabilities of DIHM with the mobility and autonomy of a robotic platform. Compared to prior uses of DIHM, a miniature and cost-effective sensor is particularly valuable as it would enable a fleet of small distributed robots to actively explore the environment in stark contrast with the large individual ships currently used for underwater DIHM.

7.3 Equipment Design

The proposed solution unites the autonomy of a robotic platform with the microscopic imaging capabilities of a DIHM in order to perform sensitive measurements of suspended particles over a large region. Furthermore, the system is low-cost, potentially enabling swarm measurements. The design of the system is described in two parts pertaining to the DIHM (Section 7.3.1) and the Aquapod (Section 7.3.3).

7.3.1 Digital In-Line Holographic Microscope

Of the many variants of holographic imaging, digital in-line holography (sometimes called Gabor holography [44]) is the simplest, only requiring a laser and a camera. The fundamentals of holographic imaging have been discussed in Section 1.3. For this application, it is necessary to reduce system complexity while maintaining sufficient imaging quality to produce reliable results. The quality of the results that can be extracted from a recorded hologram is strongly dependent on a number of features of the imaging system. These include the presence of scratches or dust in the optical path, vibrations of the sensor, the beam profile of the illuminating laser, and the use of a microscopic objective or other lenses to adjust the region of interest. The spatial resolution of the measurements is dependent on the pixel size of the camera (usually

1-5 μm) and will be equal to that size in the special case when no objective lens is used (lensless holography). The temporal resolution is determined by the camera frame rate and shutter speed. In order to prevent motion blurring, the shutter speed must be less than the time taken for an object to pass through one pixel. DIHM data becomes increasingly noisy as the concentration increases. The non-dimensional shadow density ($s_d = n_x L d^2$) generally should not exceed 0.1 where n_x is the number density, L is the sample thickness, and d is the particle diameter [71].

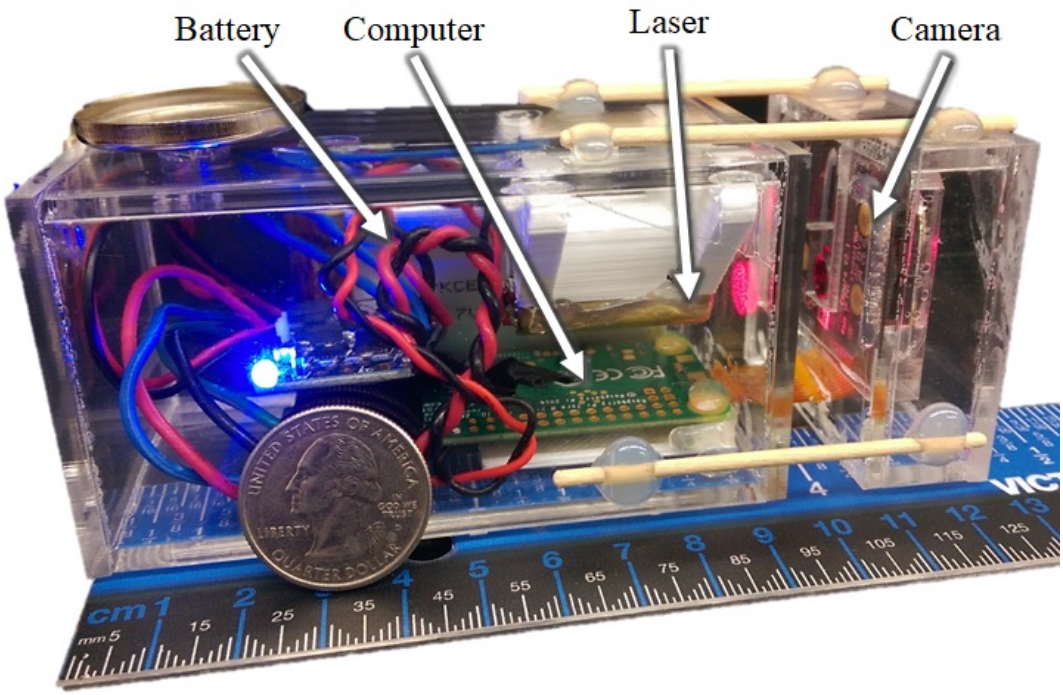

Figure 7.3: DIHM system with labeled components.

In contrast with other DIHM sensors which emphasize image quality, our sensor design emphasizes cost, size, and simplicity while recording holograms of sufficient quality for several pertinent applications. We rely on our processing approach to compensate for the higher noise resulting from the use of cheaper and smaller components. Figure 7.3 shows the complete sensor. The primary components are the laser, camera, acquisition computer, and battery.

The laser is a Quarton VLM650-11-LPA laser diode with a 650 nm wavelength and 3 mW power. The camera is a Raspberry Pi Camera Module NoIR V2 which has a maximum resolution of 3296×2512 pixels, and a pixel size of 1.12 μm. Images are captured and stored using a Raspberry Pi Zero W single-board computer which also powers the camera and laser. All components are enclosed in an acrylic enclosure which is waterproof at depths up to 5 m. In order to improve size and reliability, the enclosure is permanently sealed and cannot be accessed by a user. Charging and data transfer are performed using an Qi inductive charging pad and 802.11 wireless connection.

The frame rate and field of view are interconnected and limited by bandwidth considerations when saving images. Increasing in the field of view requires decreasing in the image capture rate. For the experiments in this paper, an image size of 2.3×2.3 mm (2048×2048 pixels) was recorded at 1 frame per second. The shutter speed was 1 μs. The depth of the sample volume (distance between imaging windows) is 10 mm, corresponding to a sample volume of 53 μL.

The total material cost of the system is $200 which is an order of magnitude reduction from previous systems and two orders less than commercial systems. The total size of this sensor is $5 \times 5 \times 13$ cm, with the majority allocated to the computer and battery. The sensor can be operated remotely via a broadcast 802.11 network signal and has a battery life of 3 hours. For underwater operation, recording is initiated via the 802.11 network prior to submerging the sensor. Image recording proceeds independent of the network connection while submerged until the trial is complete and the network connection is reestablished.

The holograms are processed using the RIHVR approach (see Chapter 2) which solves an inverse problem using an iterative algorithm to determine the 3D object that best produces the recorded hologram. Fused lasso regularization is used to ensure the result is both sparse and smooth. The GPU-accelerated algorithm takes 21 seconds to process one 2048×2048 pixel hologram with 40 reconstruction planes. Prior to reconstruction, the images are enhanced by removing a background produced by a 5 frame median. For particle counting, the 3D volume is projected to a 2D plane using a maximum intensity projection. The result is then binarized using a threshold equal to 25% of the maximum intensity. Morphological closing is then used to reduce segmentation noise followed by connected component labelling. The processing steps

are summarized in Fig. 7.4 and a MATLAB implementation of the processing code is available at github.com/HongFFIL/rihvr-matlab.

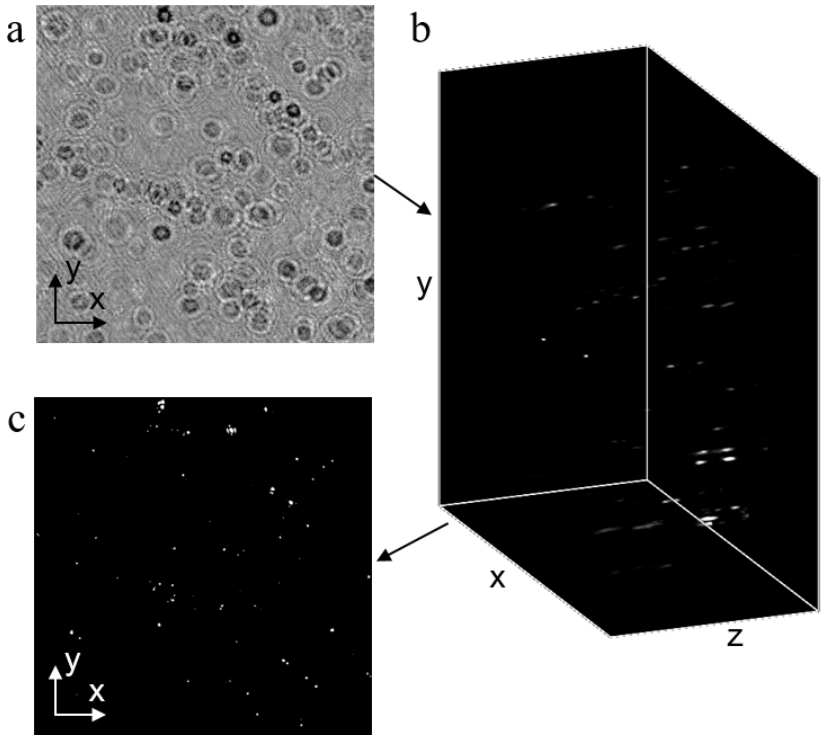

Figure 7.4: Hologram processing steps. (a) Enhanced hologram of microbubbles. (b) 3D reconstruction. (c) Binarized 2D projection.

7.3.2 On-board Processing

The RIHVR method for hologram processing is computationally demanding and requires the images be stored locally before being processed after the experiment on a computer containing a powerful GPU. This prevents the use of feedback control or intelligent path planning for the Aquapod motion. On-board processing is necessary for the system to autonomously explore the concentration map and provide real-time alerts if a hazard is encountered. Despite the increased availability of GPU processing on single-board computers such as the NVIDIA Jetson series, full hologram processing with RIHVR can still not be performed in near real-time with an on-board computer.

We propose using machine learning to approximate the full holographic processing, enabling concentration measurements to be performed rapidly and communicated to the Aquapod for navigation. The recorded holograms can be retained and processed offline to confirm the results of the machine learning approximation.

We use a simple convolutional neural network (CNN) as the predictive model 7.1. This architecture demonstrated better test performance than alternative models such as MobileNetV3 [215] which was developed for classification of images from the ImageNet database. The simple CNN ran faster and achieved a higher correlation between the predicted values and RIHVR measurements.

Table 7.1: The CNN architecture used for prediction.

Input	Operation	Stride	# Filters
$128^2 \times 3$	conv2d, 3×3	2	16
$64^2 \times 16$	conv2d, 3×3	2	40
$32^2 \times 40$	conv2d, 3×3	2	40
$16^2 \times 40$	conv2d, 3×3	2	64
$8^2 \times 64$	conv2d, 3×3	2	64
$4^2 \times 64$	conv2d, 3×3	2	128
$2^2 \times 128$	conv2d, 3×3	2	128
$1^2 \times 128$	avg pooling	na	na
$1^2 \times 128$	dense	na	1

The model is trained and evaluated using data from the laboratory experiment (Section 7.4.1). Two of the experimental configurations are used as the training data (2039 images) with the third case used as test data (649 images). The recorded images (2048×2048 pixels) were enhanced by removing the 5 frame median background and resized to 128×128 in order to increase the computational speed. This size is too small to perform conventional hologram reconstruction but most objects can still be detected manually. The model was trained for 1000 epochs with a batch size of 32 and the Adam optimizer with the default learning rate.

The average per-image prediction time on a Raspberry Pi Zero W is 240 ms. By comparison, the execution time of MobileNetV3-Small is 2300 ms. This substantial reduction in execution time means that results from the image can be produced within the time required to capture and store an image (1000 ms).

The fidelity of the model could be improved by increasing the complexity of the network. However, this will also lead to an increase in the computational time. This is unavoidable for more complicated tasks such as species identification. For these applications, a more powerful processor (such as the NVIDIA Jetson Nano) will be needed which will also lead to a larger size and increased power consumption.

7.3.3 Aquapod

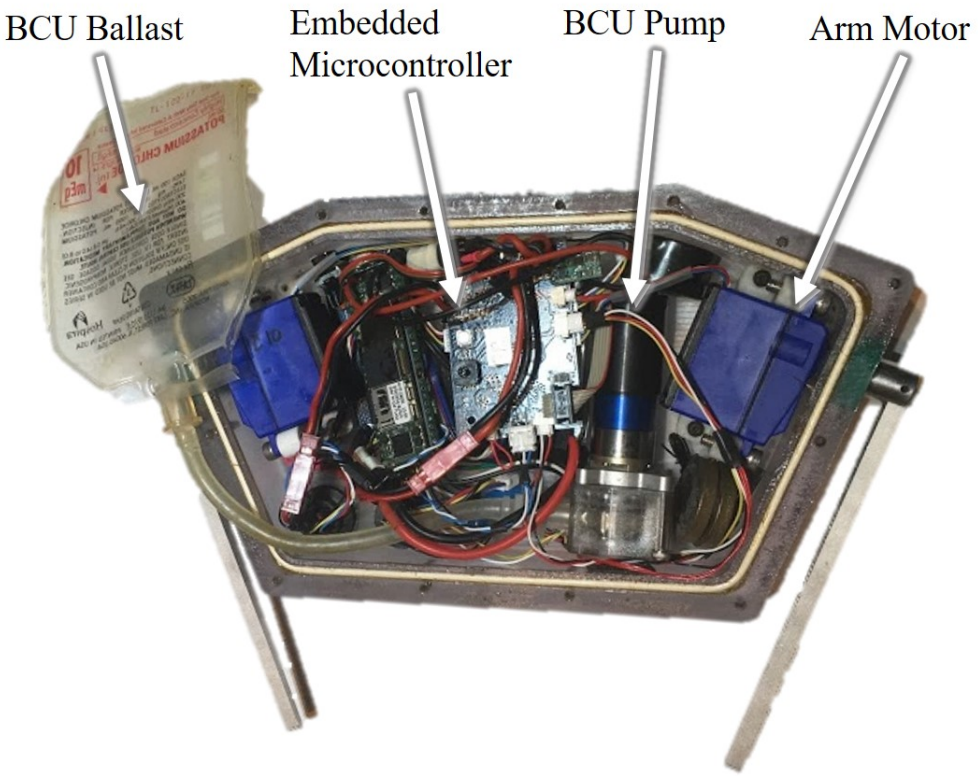

Figure 7.5: Aquapod and its buoyancy control unit (BCU). Image credit: Dario Canelon

The Aquapod [216] is an amphibious robotic platform developed by the lab of Nikolaos Papanikolopoulos. It is designed to be submersible at depths of up to 10 m and

utilizes multiple modes of locomotion including tumbling and screwdrive propulsion. These unique features enable this platform to operate in environments that are difficult for conventional robots, such as snow, sand, or muddy terrains and overcome unforeseen obstacles.

The robot can be configured with a buoyancy control unit (BCU) and screwdrive propulsion. The BCU (Fig. 7.5) uses a peristaltic pump to fill a small bladder with fluid from the surrounding environment. This allows the robot to control its density to ascend and descend in an aquatic environment. External and internal pressure sensors are used to measure the depth of the system and the current volume of ingested fluid [216].

The screwdrive propulsion system (Fig. 7.6) is used because it is able to traverse both terrestrial and aquatic environments. The system consists of a pair of independently-powered counter-rotating screws that act as propellers to drive the robot. Similar propulsion mechanisms have been used for several military, scientific, and recreational vehicles for propulsion in variable terrain including snow, sand, and water [217, 218, 219]. Unlike the more efficient BCU, the screwdrive is capable of lateral locomotion. In order to reduce the effects of high-speed fluid entrainment into the DIHM sensor volume, the screws are placed as far as possible from the sensor (see Fig. 7.1).

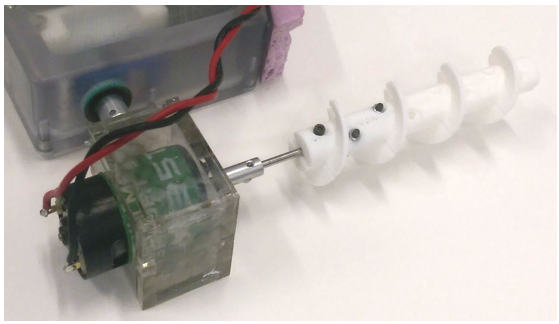

Figure 7.6: Aquapod equipped with the screwdrive propulsion system.

7.4 Experiments

Two experiments were designed to demonstrate the capabilities of the Aquapod-based DIHM system. First, a laboratory validation experiment was used to demonstrate

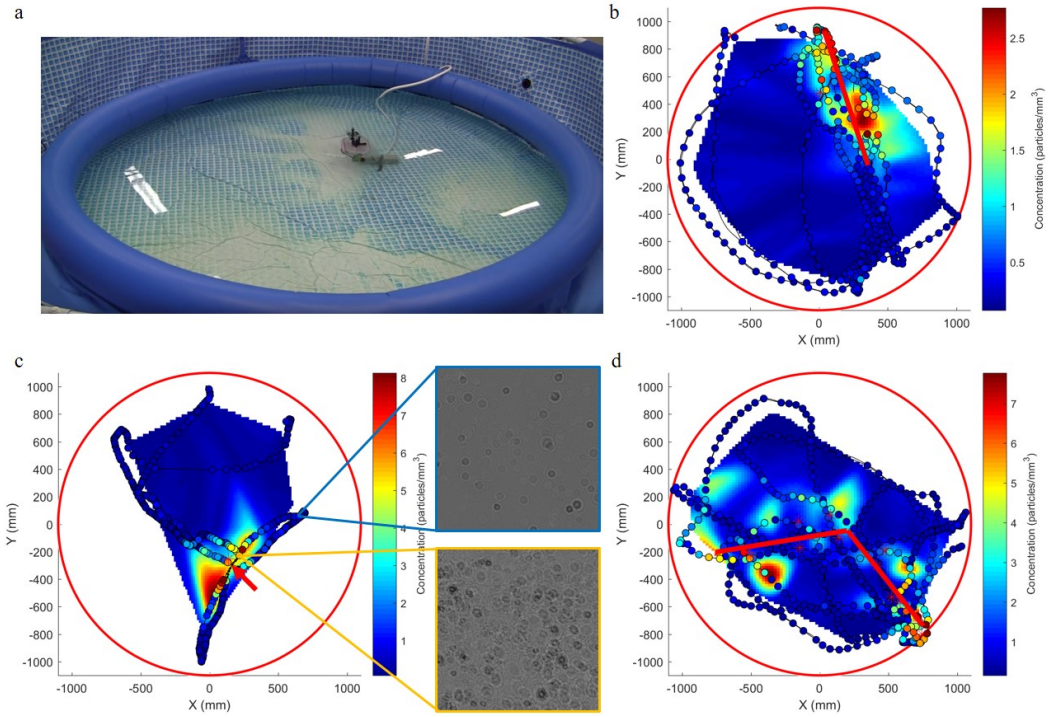

Figure 7.7: (a) The Aquapod with DIHM exploring the point source. (b) Mapped concentration of a linear arrangement of sources. Red line indicates expected source location. (c) Mapped concentration of bubbles near a point source. Red arrow indicates expected source location. Insets are enhanced holograms recorded at the marked positions. (d) Mapped concentration of sources arranged in the bent shape indicated by the red line.

.

that the system is able to map a concentration field. Second, a field experiment was performed demonstrating the ability of the combined system to measure *in situ* particle concentrations and image aquatic microorganisms in a real-world scenario.

7.4.1 Experiment 1: Laboratory Validation

Applications of the autonomous DIHM measurement may include concentration mapping to identify the source of an oil leak or the extent of an HAB. To demonstrate the ability of the robotic DIHM system to map spatial variations in particle concentration, we measured the distribution of bubbles from several source arrangements in a pool.

The test volume was a 3 m diameter, 3800 L pool with aerated water sources producing microbubbles to serve as the measured particles (Fig. 7.7(a)). Because the flow rate from the source was constant, the concentration of bubbles is assumed to be steady for the duration of the experiment. The Aquapod was manually driven throughout the pool in a manner which simulated some imprecise knowledge of the source location. The location of the system was tracked using a Vicon Vantage Motion Capture system capable of recording the full attitude of a rigid-object to within 0.1 mm at 100 Hz. Markers for the Vicon can be seen in Figure 7.1. Three source configurations were measured. The first was a point source near the center of the pool. The second was a series of five point sources arranged in a line. Finally, six points were arranged in a bent elbow shape.

The 2D path of the Aquapod on the water's surface is shown for each configuration in Fig. 7.7 along with the mapped concentration. The colored circles identify the locations where the holographic images were recorded and are colored according to the measured particle concentration. A 2D map of the concentration is estimated using a cubic interpolation from the measured points and spatially filtered with a Gaussian filter with a standard deviation of 2. Also shown are several of the recorded holographic images. These images showcase that differences in particulate concentration can be clearly identified even from the unprocessed images. They also exemplify the range of spatial scales which can be measured only using a mobile DIHM system as the holograms show local spatial variations on the sub-millimeter scale while the macro variations are mapped on the meter scale.

The measured concentrations from the three source configurations are used to validate the onboard processing approach described in Section 7.3.2. The trials with the linear and bent elbow sources were used as the training data while the point source case was used as unseen test data. The predicted particle counts for the test set are plotted in Fig. 7.8. The correlation coefficient between the prediction and the RIHVR results is 0.95.

While the model does not perfectly reproduce the RIHVR results, it is suitable for navigation feedback, given that the timescale of harmful algal blooms is hours or days (much longer than the recording duration). Complete offline processing of the recorded holograms to confirm the results of the machine learning model will still be necessary in practical applications.

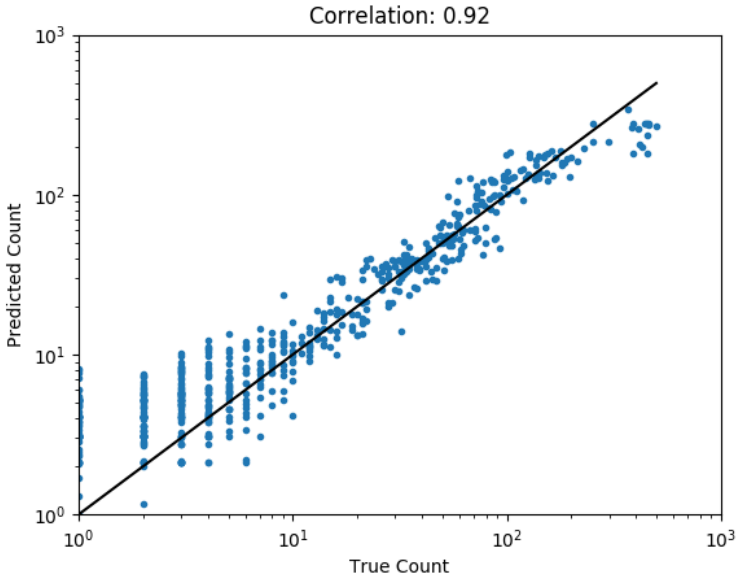

Figure 7.8: The predicted and true particle count for each image in the test set. Black line represents the optimal 1:1 match.

7.4.2 Experiment 2: *In situ* Measurement

In order to demonstrate the utility of the system in a real-world scenario, we conducted an *in situ* measurement of particle concentrations in a lake. South Center Lake in Chisago, Minnesota has been identified by the Minnesota Department of Natural Resources as a target of long-term monitoring for trends in biological, chemical, and physical features as a result of human development, climate change, and natural weather patterns. An aquatic monitoring station operated by the Saint Anthony Falls Laboratory was anchored in the lake to record the formation of algal blooms for a full growing season [37]. The monitoring station utilizes a data sonde (OTT Hydromet, Hydrolab DS5X) which measures water temperature, solar radiation, phycocyanin (a pigment found in some HAB-forming algae), and other properties at 0.5 m depth intervals. Measurements reported by the Sonde are 2 minute averages, recorded every 2 hours. Since the monitoring station is fixed, it is unable to evaluate lateral heterogeneity in the lake. A mobile robotic system capable of approximating some of the measurements of this station would be a valuable addition to these field experiments.

The Aquapod with DIHM was deployed near the monitoring station to profile the particulate concentration. With the DIHM recording holograms, the Aquapod was commanded to dive to a depth of 5.5 m, remain at that depth, and return to the surface.

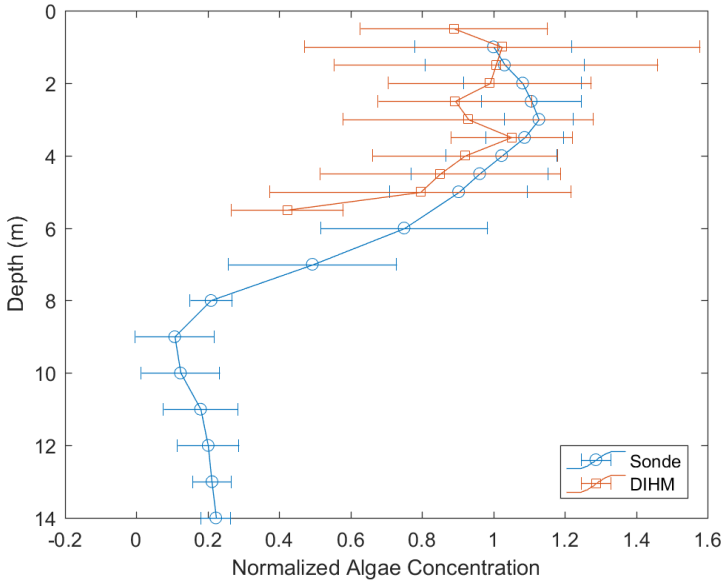

Figure 7.9: Depth profiles of algae concentration from the sonde and DIHM. Data is normalized by the surface concentration.

The concentration profiles measured by both the DIHM and the sonde are shown in Fig. 7.9. The concentration measurements of the DIHM are binned in 0.5 m increments to match the locations of the sonde measurements. The mean and standard deviation within each of the bins is plotted. The sonde profile is the 7-day average and standard deviation at each depth. All data is normalized using the concentration at the surface and the lake bed (assumed 0 for DIHM). The sonde shows a decrease in algae concentration with depth corresponding to the thermocline – the region in lakes and oceans characterized by a rapid drop in temperature with depth which also impacts the distribution of microorganisms. The DIHM profile identifies the beginning of this region. The sonde has smaller standard deviations than the DIHM due to the inherent temporal resolution discrepancy between the methods (sonde is 2 minute average,

DIHM is instantaneous). The DIHM is sensitive to small scale spatial and temporal fluctuations in the concentration which the sonde does not record.

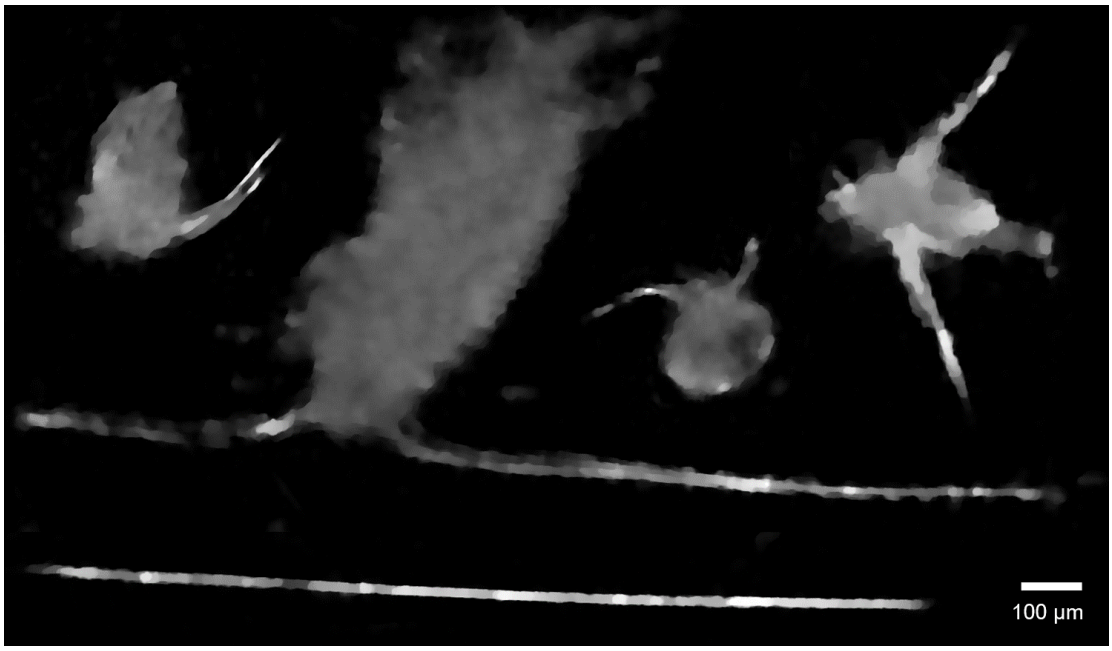

Figure 7.10: Selection of microorganisms imaged during the depth profile.

A selection of some of the microorganisms seen during the profile are shown in Fig. 7.10. Each object is shown at the manually identified in-focus plane. Note that morphological features as well as size allow for differentiation between different species.

7.5 Discussion and Conclusions

We have demonstrated a robotic system for *in situ* particle measurements in large water regions at various depths and scales. The DIHM is capable of imaging microscopic particles while the Aquapod is able to traverse areas of interest. Compared to the existing state-of-the-art, our DIHM is substantially less expensive and smaller – enabling a broad range of applications including those which utilize multiple DIHMs. Integrated with the inexpensive Aquapod in a comprehensive design, the system is able to measure at the full range of scales necessary for studies of microorganisms and particulate contaminants and do so inexpensively relative to other systems. System capabilities were

demonstrated in a laboratory experiment mapping bubble concentrations in a pool and *in situ* measurement of microorganisms in a lake.

While not demonstrated in this work, automatic classification of aquatic species using a DIHM has been successful both in the laboratory [5] and in the field using the 4Deep commercial DIHM. However, *in situ* species identification using a low-cost DIHM has not been demonstrated. Developing this capability requires increasing the computational power of the presented DIHM and collecting a corpus of classified holograms. The 3D nature of holographic reconstructions (see Fig. 7.4(b)) was not leveraged for the concentration measurements discussed in this paper. Future studies can examine heterogeneous particle distributions on the micrometer scale as well as examining swimming microorganisms using a faster image capture rate.

The full benefits of the low-cost system presented here can be best utilized by a swarm of DIHM-equipped Aquapods linked to a central mothership. This would enable rapid and autonomous reconnaissance of large bodies of water with the microscopic precision required to detect rare and harmful species or particulates.

Part IV

Conclusion

Chapter 8

Summary and Future Work

8.1 Summary

Digital inline holography (DIH) is a powerful tool for many types of particle measurements. The single-camera 3D imaging provided by DIH is desirable for autonomous underwater detection of microbes, long-term studies of algal motion, and 3D particle tracking velocimetry (PTV) among many other applications. However, traditional DIH has been limited by a number of challenges related to the processing of the recorded holograms. These challenges include limited depth resolution, low signal-to-noise ratio, and particle concentration limitations. Furthermore, computational approaches used to solve the issues are often computationally demanding. In this thesis, I first presented technical developments used to improve the accuracy of hologram reconstruction, track dense particle fields over time, and ensure that said processing can operate efficiently on large data sets. I then presented applications of DIH to measure the behavior of the algae species *Microcystis aeruginosa* and *Dunaliella primolecta* as well as a method for *in situ* aquatic measurements using a robotic platform.

The Regularized Inverse Holographic Volume Reconstruction (RIHVR) method was presented in Chapter 2 as a means to improve the accuracy of holographic reconstruction. RIHVR uses an iterative inverse approach to solve for the complex optical field that could produce the observed hologram. Physical knowledge and assumptions about this solution are used to ensure that a unique and accurate optimum exists. In particular, fused lasso regularization was applied which ensures that the volume is both

sparse (particle volume ratio is very low) and smooth (low noise in the reconstruction). The performance of RIHVR was demonstrated with several test cases. A hologram of a suspended nanowire was used to visualize the effects of both the sparse and smooth regularization in comparison to traditional reconstruction. Synthetic holograms were used to show that the extraction rate and accuracy of RIHVR exceed those of prior approaches. The rotation rates of SiC rods in a T-junction flow was directly measured, demonstrating that RIHVR enables a new type of particle-based flow measurements.

The increased particle concentrations enabled by RIHVR led to another challenge – the particles must be accurately tracked over time. Traditional tracking algorithms are limited by the particle displacement ratio. If the particle displacement exceeds the the distance between particles, PTV becomes very challenging. This was addressed in Chapter 3 by using machine learning to develop a model-based predictor that is able to learn how to predict future motion from a particle's location and history The predictor uses an LSTM which is trained using trajectories that demonstrate the range of expected particle motion patterns. Two methods were proposed to train the LSTM. The first method uses supplemental experiments with a low particle displacement ratio (but the same fundamental motion) to collect reliable particle trajectories. The second method uses traditional tracking methods with manual intervention to identify trajectories suitable for training. Both methods were demonstrated on experimental data including T-junction flow and swimming algae. The results illustrate that the learned predictor is superior to other tracking approaches.

A simple application of DIH-PTV towards the measurement of the the buoyant rising velocities of *Microcystis aeruginosa* colonies was presented in Chapter 5. *Microcystis* is a colonial alga that can form toxic harmful algal blooms (HABs). These HABs are known to form predominantly in warm temperatures, although precise models for how temperature affects the growth and buoyancy of the *Microcystis* colonies are unknown. Using DIH-PTV, we measured the buoyant velocities of *Microcystis* colonies in a laboratory setting. Using Stokes' Law, we were able to determine that temperature drives a significant change in the average colony density.

The swimming behaviors of the motile alga *Dunaliella primolecta* were studied in Chapter 6. *D. primolecta* can be farmed to produce nutritional supplements and lipids for biodiesel production. However, optimizing this production requires identifying the

correct time to harvest the culture. Current methods for the analysis of lipid content are complex and slow; DIH-PTV could provide a faster method for identifying the optimal harvest time. Prior research has suggested that lipid production is linked to the metabolic stress on the cells which may also may also be indicated by changes in behavior. DIH-PTV was used to record and and track the motions of thousands of *D. primolecta* cells at three different stages of culture growth. A decision tree was used to identify each trajectory as belonging to one of five categories: linear, meandering, random walk, helical, and circular. These were further described as representing either gross or fine motions. We found that the ratio of gross to fine motions increased when the cells were under stress caused by nutrient deficiency. The same stress was also seen to coincide with the peak lipid content. This discovery could enable better optimization of biodiesel production pipelines.

Finally, a miniature underwater DIHM for *in situ* measurements of HABs and other aquatic particulates is described in Chapter 7. The extremely low-cost and compact DIHM is paired with a robotic platform to enable autonomous measurements of microscopic particles at the scale of a lake or other body of water. Despite the simplified and low-cost components required to miniaturize the sensor, the results are suitable for measuring particle concentration and identifying classes of organisms. A convolutional neural network (CNN) was trained in order to process the recorded holograms in real time on-board the low-power Raspberry Pi Zero used in the sensor. Laboratory experiments with various configurations of bubble generators in a pool were used to demonstrate the ability of the combined robotic platform to generate a spatial map of the bubble concentration. An *in situ* deployment in a local lake demonstrated that the DIHM can measure the vertical particle distribution while also capturing images that can be used to identify the types of microorganisms that are present.

8.2 Future Work

The measurements of rod rotation in flow that were presented in Chapter 2 inspire a new type of flow measurement: direct vorticimetry. While the rotation rate of rods is a function of both flow vorticity and shear rate, a spherical particle will rotate at a rate equal to the half the flow vorticity [115]. Preliminary work has sought to synthesize

transparent particles that contain embedded opaque tracers. Particles with a diameter of 120 μm containing 6 μm microbeads have been synthisized by Dang et al. [220]. However, reproduction of these particles with monodisperse size distribution and excellent optical clarity has proven difficult. Attempts at synthesizing such particles and applying them to flow vorticimetry are ongoing.

While the RIHVR method presented in Chapter 2 is highly accurate, it still has its limitations. For excessively noisy or dense holograms, accurate reconstruction may not be feasible. Furthermore, while GPU acceleration does make RIHVR practical, it does not come close to real-time processing. Achieving such extreme speeds may be possible using CNNs which are often able to process images in less than a second.

Recent work not presented in this thesis has explored using machine learning to completely replace physics-based hologram reconstruction [221]. This approach has shown the ability to accurately extract particle positions from extremely dense holograms for simulations and experimental cases where ground truth particle locations can be identified for training. However, applying this approach to useful experimental cases is challenging. Ongoing work seeks to use simulated images to train a CNN that can accurately process real images.

A timely application that bears special mention is the application of DIH to measure the particles produced by humans as they breath or speak. At the time of this writing, the global COVID-19 outbreak has caused a near total shutdown of the global economy. Recent research has suggested that the extreme transmissibility of the virus may be due to airborne transmission [222, 20, 223]. Current methods for measuring exhaled aerosols do not produce measurements suitable for estimating the spreading capability of these particles; they often cannot measure at low concentrations and do not measure *in situ*. Holographic imaging is well suited to these measurements as it is non-invasive and capable of accurately measuring particles at low concentrations and across a broad size range. Ongoing measurements using DIH may provide a clearer understanding of COVID-19 transmission and lead to improved evidence-based social distancing policies.

References

[1] Joseph Katz and Jian Sheng. Applications of holography in fluid mechanics and particle dynamics. *Annual Review of Fluid Mechanics*, 42(1):531–555, 2010.

[2] Scott M Spuler and Jacob Fugal. Design of an in-line, digital holographic imaging system for airborne measurement of clouds. *Applied optics*, 50(10):1405–1412, 2011.

[3] S Talapatra, Jiarong Hong, M McFarland, Ar Nayak, C Zhang, Joseph Katz, J Sullivan, M Twardowski, J Rines, and P Donaghay. Characterization of biophysical interactions in the water column, using in situ digital holography. *Marine Ecology Progress Series*, 473:29–51, 2012.

[4] Lina Rotermund, John Samson, and Jürgen Kreuzer. A Submersible Holographic Microscope for 4-D In-Situ Studies of Micro-Organisms in the Ocean with Intensity and Quantitative Phase Imaging. *Journal of Marine Science: Research & Development*, 06(01):1–5, 2015.

[5] Ahmed El Mallahi, Christophe Minetti, and Frank Dubois. Automated three-dimensional detection and classification of living organisms using digital holographic microscopy with partial spatial coherent source: application to the monitoring of drinking water resources. *Applied Optics*, 52(1):A68–80, 2013.

[6] Christian A. Lindensmith, Stephanie Rider, Manuel Bedrossian, J. Kent Wallace, Eugene Serabyn, G. Max Showalter, Jody W. Deming, and Jay L. Nadeau. A submersible, off-axis holographic microscope for detection of microbial motility and morphology in aqueous and icy environments. *Plos One*, 11(1):e0147700, 2016.

[7] Dan Allan, Casper van der Wel, Nathan Keim, Thomas A Caswell, Devin Wieker, Ruben Verweij, Chaz Reid, Thierry, Lars Grueter, Kieran Ramos, Apiszcz, Zoeith, Rebecca W Perry, François Boulogne, Prashant Sinha, Pfigliozzi, Nicolas Bruot, Leonardo Uieda, Jan Katins, Hadrien Mary, and Aron Ahmadia. soft-matter/trackpy: Trackpy v0.4.2. oct 2019.

[8] David Kirk and Wen-mei Hwu. *Programming Massively Parallel Processors: A Hands-on Approach*. 2nd edition, 2012.

[9] E N Jacobsen, A Pfaltz, H Yamamoto, D W C Macmillan, and X Shi. References and Notes 1. 340(May), 2013.

[10] U.S. Environmental Protection Agency. A Compilation of Cost Data Associated with the Impacts and Control of Nutrient Pollution. Technical Report May, U.S. Environmental Protection Agency, 2015.

[11] Hans W Paerl, Rolland S Fulton, Pia H Moisander, and Julianne Dyble. Harmful Freshwater Algal Blooms, With an Emphasis on Cyanobacteria. *Paerl: Harmful Freshwater Algal Blooms TheScientificWorld Harmful Freshwater Algal Blooms TheScientificWorld*, 1(1):76–113, 2001.

[12] G. T. Csanady. Turbulent Diffusion of Heavy Particles in the Atmosphere, 1963.

[13] Balaji Gopalan, Edwin Malkiel, and Joseph Katz. Experimental investigation of turbulent diffusion of slightly buoyant droplets in locally isotropic turbulence. *Physics of Fluids*, 20(9), 2008.

[14] Ville A. Kaikkonen, Dmitry Ekimov, and Anssi J. Makynen. A holographic in-line imaging system for meteorological applications. *Conference Record - IEEE Instrumentation and Measurement Technology Conference*, 63(5):1630–1635, 2013.

[15] George Graham and Alex Nimmo-Smith. The application of holography to the analysis of size and settling velocity of suspended cohesive sediments. *Limnology and Oceanography: Methods*, pages 1–15, 2010.

[16] B. Bake, P. Larsson, G. Ljungkvist, E. Ljungström, and A. C. Olin. Exhaled particles and small airways. *Respiratory Research*, 20(1):1–14, 2019.

[17] Jonathan S. Yoder, Courtney Harral, and Michael J. Beach. Giradiasis surveillance - United States, 2006-2008. *Morbidity and Mortality Weekly Report*, 59(SS-6):1–14, 2010.

[18] Alfred P. Dufour, Otis Evans, Thomas D. Behymer, and Ricardo Cantú. Water ingestion during swimming activities in a pool: A pilot study. *Journal of Water and Health*, 4(4):425–430, dec 2006.

[19] Sima Asadi, Anthony S. Wexler, Christopher D. Cappa, Santiago Barreda, Nicole M. Bouvier, and William D. Ristenpart. Aerosol emission and superemission during human speech increase with voice loudness. *Scientific Reports*, 9(1):1–10, 2019.

[20] Dyani Lewis. Is the coronavirus airborne? Experts can't agree. *Nature*, 2020.

[21] G. E. Elsinga, F. Scarano, B. Wieneke, and B. W. Van Oudheusden. Tomographic particle image velocimetry. *Experiments in Fluids*, 41(6):933–947, 2006.

[22] P. Sarder and A. Nehorai. Deconvolution methods for 3-D fluorescence microscopy images. *IEEE Signal Processing Magazine*, 23(3), 2006.

[23] J M Coupland and J Lobera. Holography, tomography and 3D microscopy as linear filtering operations. *Measurement Science and Technology*, 19(7):074012, 2008.

[24] Mostafa Toloui, Sean Riley, Jiarong Hong, K. Howard, L. P. Chamorro, Michele Guala, and J. Tucker. Measurement of atmospheric boundary layer based on super-large-scale particle image velocimetry using natural snowfall. *Experiments in Fluids*, 55(5):1–14, 2014.

[25] Christian J. Kähler, Tommaso Astarita, Pavlos P. Vlachos, Jun Sakakibara, Rainer Hain, Stefano Discetti, Roderick La Foy, and Christian Cierpka. Main results of the 4th International PIV Challenge. *Experiments in Fluids*, 57(6):1–71, 2016.

[26] Jerry Westerweel, Gerrit E. Elsinga, and Ronald J. Adrian. Particle Image Velocimetry for Complex and Turbulent Flows. *Annual Review of Fluid Mechanics*, 45(1):409–436, jan 2013.

[27] Dana Dabiri and Charles Pecora. *Particle Tracking Velocimetry*. IOP Publishing, nov 2019.

[28] N. A. Malik, T Dracos, and D. A. Papantoniou. Particle Tracking Velocimetry in 3-Dimensional Flows .2. Particle Tracking. *Experiments in Fluids*, 15(4-5):279–294, 1993.

[29] S. J. Baek and S. J. Lee. A new two-frame particle tracking algorithm using match probability. *Experiments in Fluids*, 22(1):23–32, 1996.

[30] Fujio Yamamoto, Tomomasa Uemura, Zhang Huai Tian, and Kazuo Ohmi. Three-Dimensional PTV Based on Binary Cross-Correlation Method. Algorithm of Particle Identification. *JSME International Journal Series B*, 36(2):279–284, 1993.

[31] Daniel Schanz, Sebastian Gesemann, and Andreas Schröder. Shake-The-Box: Lagrangian particle tracking at high particle image densities. *Experiments in Fluids*, 57(5):1–27, 2016.

[32] Christine Mounaïm-Rousselle and Olivier Pajot. Droplet sizing by Mie scattering interferometry in a spark ignition engine. *Particle and Particle Systems Characterization*, 16(4):160–168, 1999.

[33] W. D. Bachalo and M. J. Houser. Phase/Doppler Spray Analyzer For Simultaneous Measurements Of Drop Size And Velocity Distributions. *Optical Engineering*, 23(5):583–590, 1984.

[34] W. D. Griffiths, S. Patrick, and A. P. Rood. Aerodynamic Particle Size Analyser Tested With Spheres, Compact Particles and Fibres Having a Common Settling Rate Under Gravity. 15(4):238–240, 1984.

[35] Robert K. Vincent, Xiaoming Qin, R. Michael L McKay, Jeffrey Miner, Kevin Czajkowski, Jeffrey Savino, and Thomas Bridgeman. Phycocyanin detection from

LANDSAT TM data for mapping cyanobacterial blooms in Lake Erie. *Remote Sensing of Environment*, 89(3):381–392, 2004.

[36] Timothy T Wynne, Richard P Stumpf, Michelle C Tomlinson, and Julianne Dyble. Characterizing a cyanobacterial bloom in western Lake Erie using satellite imagery and meteorological data. *Limnology and Oceanography*, 55(5):2025–2036, 2010.

[37] A. A. Wilkinson, M. Hondzo, and M. Guala. Vertical heterogeneities of cyanobacteria and microcystin concentrations in lakes using a seasonal In situ monitoring station. *Global Ecology and Conservation*, 21:e00838, 2020.

[38] Ting-Chung Poon and Jung-Ping Liu. *Introduction to modern Digital holography with MATLAB*. Cambridge University, 2014.

[39] Xiao Yu, Jisoo Hong, Changgeng Liu, and Myung K. Kim. Review of digital holographic microscopy for three-dimensional profiling and tracking. *Optical Engineering*, 53(11):112306, 2014.

[40] Mostafa Toloui, Kevin Mallery, and Jiarong Hong. Improvements on digital inline holographic PTV for 3D wall-bounded turbulent flow measurements. *Measurement Science and Technology*, 28(4):044009, apr 2017.

[41] Matthew J Beals, Jacob P Fugal, Raymond A Shaw, Jiang Lu, Scott M Spuler, and Jeffrey L Stith. Holographic measurements of inhomogeneous cloud mixing at the centimeter scale. *Science*, 350(6256):87–90, 2015, arXiv:1011.1669v3.

[42] Aydogan Ozcan and Euan Mcleod. Lensless imaging and sensing. *Annual Review of Biomedical Engineering*, 18(January):77–102, 2016.

[43] Yi-chen Wu, Ashutosh Shiledar, Yi-cheng Li, Jeffrey Wong, Steve Feng, Xuan Chen, Christine Chen, Kevin Jin, Zhe Yang, Zachary Scott Ballard, Zoltán Göröcs, Xuan Chen, Christine Chen, Kevin Jin, Saba Janamian, Zhe Yang, and Zachary Scott. Air Quality Monitoring Using Mobile Microscopy and Machine Learning Yi-Chen. (March), 2017.

[44] D Gabor. A new microscopic principle. *Nature*, 161(4098):777–778, 1948.

[45] J. D. Trolinger, R. A. Belz, and W. M. Farmer. Holographic Techniques for the Study of Dynamic Particle Fields. *Applied Optics*, 8(5):957, 1969.

[46] Hui Meng and Fazle Hussain. Holographic particle velocimetry: a 3D measurement technique for vortex interactions, coherent structures and turbulence. *Fluid Dynamics Research*, 8(1-4):33–52, 1991.

[47] Scott Simmons, Hui Meng, Fazle Hussain, and David Liu. Advances in holographic particle velocimetry. In Soyoung S. Cha and James D. Trolinger, editors, *Optical Diagnostics in Fluid and Thermal Flow*, volume 2005, pages 306–317, dec 1993.

[48] U Schnars and W Jüptner. Direct recording of holograms by a CCD target and numerical reconstruction. 33(2):179–181, 1994.

[49] Jian Sheng, E. Malkiel, and Joseph Katz. Buffer layer structures associated with extreme wall stress events in a smooth wall turbulent boundary layer. *Journal of Fluid Mechanics*, 633:17–60, 2009.

[50] Mozhdeh Seifi, Corinne Fournier, Nathalie Grosjean, Loic Méès, Jean-Louis Marié, and Loic Denis. Accurate 3D tracking and size measurement of evaporating droplets using in-line digital holography and "inverse problems" reconstruction approach. *Optics Express*, 21(23):27964, nov 2013.

[51] Mehdi Molaei, Michael Barry, Roman Stocker, and Jian Sheng. Failed escape: solid surfaces prevent tumbling of Escherichia coli. *Physical Review Letters*, 113(6):1–6, 2014.

[52] Cao Zhang, Rinaldo Miorini, and Joseph Katz. Integrating Mach-Zehnder interferometry with TPIV to measure the time-resolved deformation of a compliant wall along with the 3D velocity field in a turbulent channel flow. *Experiments in Fluids*, 56(11):1–22, 2015.

[53] Mostafa Toloui, Aliza Abraham, and Jiarong Hong. Experimental investigation of turbulent flow over surfaces of rigid and flexible roughness. *Experimental Thermal and Fluid Science*, 101(August 2018):263–275, 2019.

[54] Dhananjay Kumar Singh and P. K. Panigrahi. Threedimensional investigation of liquid slug taylor flow inside a microcapillary using holographic velocimetry. *Experiments in Fluids*, 56(1), 2015.

[55] Hangjian Ling, Siddarth Srinivasan, Kevin Golovin, Gareth H. McKinley, Anish Tuteja, and Joseph Katz. High-resolution velocity measurement in the inner part of turbulent boundary layers over super-hydrophobic surfaces. *Journal of Fluid Mechanics*, 801:670–703, 2016.

[56] Matthew J Beals, Jacob P Fugal, Raymond A Shaw, Jiang Lu, Scott M Spuler, and Jeffrey L Stith. Holographic measurements of inhomogeneous cloud mixing at the centimeter scale. *Science*, 350(6256):87–90, oct 2015.

[57] Cathy Wu, Aboudy Kreidieh, Eugene Vinitsky, and Alexandre M Bayen. Emergent Behaviors in Mixed-Autonomy Traffic. *Proceedings of the 1st Annual Conference on Robot Learning*, 78(CoRL):398–407, 2017.

[58] S. Santosh Kumar, Yaning Sun, Sige Zou, and Jiarong Hong. 3D Holographic Observatory for Long-term Monitoring of Complex Behaviors in Drosophila. *Scientific Reports*, 6(August):33001, 2016.

[59] A. Chengala, M. Hondzo, and D. G. Mashek. Fluid motion mediates biochemical composition and physiological aspects in the green alga Dunaliella primolecta Butcher. *Limnology & Oceanography: Fluids & Environments*, 3(0):74–88, 2013.

[60] Laszlo Orzo, Balazs Wittner, and Szabolcs Tokes. High speed water monitoring systems based on Digital Holographic Microscopy. *Ninth International Conference on Computer Science and Information Technologies Revised Selected Papers*, pages 1–9, 2013.

[61] Zoltán Grcs, Miu Tamamitsu, Vittorio Bianco, Patrick Wolf, Shounak Roy, Koyoshi Shindo, Kyrollos Yanny, Yichen Wu, Hatice Ceylan Koydemir, Yair Rivenson, and Aydogan Ozcan. A deep learning-enabled portable imaging flow cytometer for cost-effective, high-throughput, and label-free analysis of natural water samples. *Light: Science & Applications*, 7(1):66, 2018.

[62] Tinghua Zhang and Kun Gao. MAP-MRF-Based Super-Resolution Reconstruction Approach for Coded Aperture Compressive Temporal Imaging. *Applied Sciences*, 8(3):338, 2018.

[63] Yuan Fang, Ningmei Yu, Yuquan Jiang, and Chaoliang Dang. High-precision lens-less flow cytometer on a chip. *Micromachines*, 9(5):1–13, 2018.

[64] Mohendra Roy, Dongmin Seo, Chang Hyun Oh, Myung Hyun Nam, Young Jun Kim, and Sungkyu Seo. Low-cost telemedicine device performing cell and particle size measurement based on lens-free shadow imaging technology. *Biosensors and Bioelectronics*, 67:715–723, 2015.

[65] Yong-Seok Choi and Sang-Joon Lee. Three-dimensional volumetric measurement of red blood cell motion using digital holographic microscopy. *Applied optics*, 48(16):2983–2990, 2009.

[66] Ting-Wei Su, Liang Xue, and Aydogan Ozcan. High-throughput lensfree 3D tracking of human sperms reveals rare statistics of helical trajectories. *Proceedings of the National Academy of Sciences of the United States of America*, 109(40):16018–22, 2012.

[67] Mustafa Ugur Daloglu, Wei Luo, Faizan Shabbir, Francis Lin, Kevin Kim, Inje Lee, Jia Qi Jiang, Wen Jun Cai, Vishwajith Ramesh, Meng Yuan Yu, and Aydogan Ozcan. Label-free 3D computational imaging of spermatozoon locomotion, head spin and flagellum beating over a large volume. *Light: Science and Applications*, 7(1):17111–17121, 2018.

[68] Divya Pathania, Christian Landeros, Lucas Rohrer, Victoria D Agostino, Seonki Hong, Hyungsoon Im, and Cesar M Castro. Theranostics Point-of-care cervical cancer screening using deep learning-based microholography. 9(26), 2019.

[69] Yichen Wu and Aydogan Ozcan. Lensless digital holographic microscopy and its applications in biomedicine and environmental monitoring. *Methods*, 136:4–16, 2018.

[70] Alon Greenbaum and Aydogan Ozcan. Maskless imaging of dense samples using pixel super-resolution based multi-height lensfree on-chip microscopy. *Optics Express*, 20(3):3129, 2012.

[71] Mokrane Malek, D Allano, S Coëtmellec, and D Lebrun. Digital in-line holography: influence of the shadow density on particle field extraction. *Optics Express*, 12(10):2270–2279, 2004.

[72] J. Zhang, B. Tao, and J. Katz. Turbulent flow measurement in a square duct with hybrid holographic PIV. *Experiments in Fluids*, 23(5):373–381, 1997.

[73] V Kebbel, M Adams, H-J Hartmann, and W Jüptner. Digital holography as a versatile optical diagnostic method for microgravity experiments. *Measurement Science and Technology*, 10(10):893–899, 1999.

[74] N. A. Buchmann, C. Atkinson, and J. Soria. Ultra-high-speed tomographic digital holographic velocimetry in supersonic particle-laden jet flows. *Measurement Science and Technology*, 24(2):024005, 2013.

[75] Jian Gao and Joseph Katz. Self-calibrated microscopic dual-view tomographic holography for 3D flow measurements. *Optics Express*, 26(13):16708–16725, 2018.

[76] Daniel Allano, Mokrane Malek, Françoise Walle, Frédéric Corbin, Gilles Godard, Sébastien Coëtmellec, Bertrand Lecordier, Jean-marc Foucaut, and Denis Lebrun. Three-dimensional velocity near-wall measurements by digital in-line holography: calibration and results. *Applied Optics*, 52(1):A9–A17, 2013.

[77] Siddharth Talapatra and Joseph Katz. Three-dimensional velocity measurements in a roughness sublayer using microscopic digital in-line holography and optical index matching. *Measurement Science and Technology*, 24(2):024004, feb 2013.

[78] Lujie Cao, Gang Pan, Jeremy de Jong, Scott Woodward, and Hui Meng. Hybrid digital holographic imaging system for three-dimensional dense particle field measurement. *Applied optics*, 47(25):4501–4508, 2008.

[79] Jonas Kühn, Bimochan Niraula, Kurt Liewer, J. Kent Wallace, Eugene Serabyn, Emilio Graff, Christian Lindensmith, and Jay L. Nadeau. A Mach-Zender digital

holographic microscope with sub-micrometer resolution for imaging and tracking of marine micro-organisms. *Review of Scientific Instruments*, 85(12):123113, 2014.

[80] Nicholas Burns and John Watson. Data extraction from underwater holograms of marine organisms. In *OCEANS 2007 - Europe*, pages 1–6. IEEE, jun 2007.

[81] Laurence Wilson and Rongjing Zhang. 3D localization of weak scatterers in digital holographic microscopy using Rayleigh-Sommerfeld back-propagation. *Optics Express*, 20(15):16735, 2012.

[82] Ferréol Soulez, Loïc Denis, Eric Thiébaut, Corinne Fournier, and Charles Goepfert. Inverse problem approach in particle digital holography: out-of-field particle detection made possible. *Journal of the Optical Society of America A*, 24(12):3708–3716, 2007.

[83] Loic Denis, Corinne Fournier, Thierry Fournel, and Christophe Ducottet. Twin-image noise reduction by phase retrieval in in-line digital holography. In Manos Papadakis, Andrew F. Laine, and Michael A. Unser, editors, *Proceedings of SPIE*, number 5914, page 59140J, aug 2005.

[84] Tatiana Latychevskaia and Hans-Werner Fink. Solution to the Twin Image Problem in Holography. *Physical Review Letters*, 98(23):233901, jun 2007.

[85] Lisa Dixon, Fook Chiong Cheong, and David G. Grier. Holographic deconvolution microscopy for high-resolution particle tracking. *Optics Express*, 19(17):16410, 2011.

[86] Tatiana Latychevskaia and Hans-Werner Fink. Holographic time-resolved particle tracking by means of three-dimensional volumetric deconvolution. *Optics Express*, 22(17):20994, 2014.

[87] Mostafa Toloui and Jiarong Hong. High fidelity digital inline holographic method for 3D flow measurements. *Optics Express*, 23(21):27159, oct 2015.

[88] Kevin Mallery and Jiarong Hong. Regularized inverse holographic volume reconstruction for 3D particle tracking. *Optics Express*, 27(13):18069–18084, 2019.

[89] Ferréol Soulez, Loïc Denis, Corinne Fournier, Eric Thiébaut, and Charles Goepfert. Inverse-problem approach for particle digital holography: accurate location based on local optimization. *Journal of the Optical Society of America A*, 24(4):1164–1171, 2007.

[90] David J Brady, Kerkil Choi, Daniel L Marks, Ryoichi Horisaki, and Sehoon Lim. Compressive holography. *Optics Express*, 17(15):13040–13049, 2009.

[91] N Verrier, N Grosjean, E Dib, L Méès, Corinne Fournier, and J-L Marié. Improvement of the size estimation of 3D tracked droplets using digital in-line holography with joint estimation reconstruction. *Measurement Science and Technology*, 27(4):045001, 2016.

[92] Sang-Hyuk Lee, Yohai Roichman, Gi-Ra Yi, Shin-Hyun Kim, Seung-Man Yang, Alfons van Blaaderen, Peter van Oostrum, and David G. Grier. Characterizing and tracking single colloidal particles with video holographic microscopy. *Optics Express*, 15(26):18275–18282, 2007, 0712.1738.

[93] Fook Chiong Cheong, Bhaskar Jyoti Krishnatreya, and David G. Grier. Strategies for three-dimensional particle tracking with holographic video microscopy. *Optics Express*, 18(13):13563–13573, 2010.

[94] Loïc Denis, Dirk Lorenz, Eric Thiébaut, Corinne Fournier, and Dennis Trede. Inline hologram reconstruction with sparsity constraints. *Optics letters*, 34(22):3475–3477, 2009.

[95] Frédéric Jolivet, Fabien Momey, Loïc Denis, Loïc Méès, Nicolas Faure, Nathalie Grosjean, Frédéric Pinston, Jean-Louis Marié, and Corinne Fournier. Regularized reconstruction of absorbing and phase objects from a single in-line hologram, application to fluid mechanics and micro-biology. *Optics Express*, 26(7):8923, apr 2018, 1705.04286.

[96] Anthony Berdeu, Olivier Flasseur, Loïc Méès, Loïc Denis, Fabien Momey, Thomas Olivier, Nathalie Grosjean, and Corinne Fournier. Reconstruction of in-line holograms: combining model-based and regularized inversion. *Optics Express*, 27(10):14951, 2019.

[97] Yutaka Endo, Tomoyoshi Shimobaba, Takashi Kakue, and Tomoyoshi Ito. GPU-accelerated compressive holography. *Optics Express*, 24(8):8437, 2016.

[98] Amir Beck and Marc Teboulle. Fast gradient-based algorithms for constrained total variation image denoising and deblurring problems. *IEEE Transactions on Image Processing*, 18(11):2419–2434, 2009.

[99] Tom Goldstein, Christoph Studer, and Richard Baraniuk. A field guide to forward-backward splitting with a FASTA implementation. *arXiv:1411.3406*, page 25, 2014, 1411.3406.

[100] Neal Parikh and Stephen Boyd. Proximal algorithms. *Foundations and Trends in Optimization*, 1(3):127–239, 2014, 1502.03175.

[101] Robert Tibshirani, Michael Saunders, Saharon Rosset, Ji Zhu, and Keith Knight. Sparsity and smoothness via the fused lasso. *Journal of the Royal Statiscical Society Series B*, 67(1):91–108, 2005.

[102] Amir Beck and Marc Teboulle. A fast iterative shrinkage-thresholding algorithm. *Society for Industrial and Applied Mathematics Journal on Imaging Sciences*, 2(1):183–202, 2009.

[103] D. Chareyron, J. L. Marié, Corinne Fournier, J. Gire, N. Grosjean, L. Denis, M. Lance, and L. Méès. Testing an in-line digital holography 'inverse method' for the Lagrangian tracking of evaporating droplets in homogeneous nearly isotropic turbulence. *New Journal of Physics*, 14:043039, 2012.

[104] J. L. Marié, T. Tronchin, N. Grosjean, L. Méès, O. Can Öztürk, Corinne Fournier, B. Barbier, and M. Lance. Digital holographic measurement of the Lagrangian evaporation rate of droplets dispersing in a homogeneous isotropic turbulence. *Experiments in Fluids*, 58(2):11, 2017.

[105] Gang Pan and Hui Meng. Digital holography of particle fields : reconstruction by use of complex amplitude. *Applied Optics*, 42(5):827–833, 2003.

[106] Michel Kempkes, Emmanouil Darakis, Taslima Khanam, Arvind Rajendran, Vinay Kariwala, Marco Mazzotti, Thomas J Naughton, and Anand K Asundi.

Three dimensional digital holographic profiling of micro-fibers. *Optics Express*, 17(4):2938–2943, 2009.

[107] Yi Li, Eric Perlman, Minping Wan, Yunke Yang, Charles Meneveau, Randal Burns, Shiyi Chen, Alexander Szalay, and Gregory Eyink. A public turbulence database cluster and applications to study Lagrangian evolution of velocity increments in turbulence. *Journal of Turbulence*, 9(November 2016):N31, 2008, 0804.1703.

[108] Eric Perlman, Randal Burns, Yi Li, and Charles Meneveau. Data exploration of turbulence simulations using a database cluster. In *Proceedings of the 2007 ACM/IEEE Conference on Supercomputing (SC '07)*, Reno, Nevada, USA, 2007.

[109] Huidan Yu, Kalin Kanov, Eric Perlman, Jason Graham, Edo Frederix, Randal Burns, Alexander Szalay, Gregory Eyink, and Charles Meneveau. Studying Lagrangian dynamics of turbulence using on-demand fluid particle tracking in a public turbulence database. *Journal of Turbulence*, 13(May):1–29, 2012.

[110] John C. Crocker and David G. Grier. Methods of digital video microscopy for colloidal studies. *Journal of Colloid and Interface Science*, 179(1):298–310, 1996, 96.

[111] Helena M. Amaro, A. Catarina Guedes, and F. Xavier Malcata. Advances and perspectives in using microalgae to produce biodiesel. *Applied Energy*, 88(10):3402–3410, 2011.

[112] Anwar Chengala, Miki Hondzo, and Jian Sheng. Microalga propels along vorticity direction in a shear flow. *Physical Review E*, 87(5):052704, 2013.

[113] Daniele Vigolo, Stefan Radl, and Howard A. Stone. Unexpected trapping of particles at a T junction. *Proceedings of the National Academy of Sciences*, 111(13):4770–4775, 2014.

[114] E. Katz, A. L. Yarin, W. Salalha, and E. Zussman. Alignment and self-assembly of elongated micronsize rods in several flow fields. *Journal of Applied Physics*, 100(3):034313, 2006.

[115] Shima Parsa, Jeffrey S. Guasto, Monica Kishore, Nicholas T. Ouellette, J. P. Gollub, and Greg A. Voth. Rotation and alignment of rods in two-dimensional chaotic flow. *Physics of Fluids*, 23(4):043302, 2011.

[116] Shima Parsa, Enrico Calzavarini, Federico Toschi, and Greg A. Voth. Rotation rate of rods in turbulent fluid flow. *Physical Review Letters*, 109(13):134501, 2012, 1205.0219.

[117] Guy G. Marcus, Shima Parsa, Stefan Kramel, Rui Ni, and Greg A. Voth. Measurements of the solid-body rotation of anisotropic particles in 3D turbulence. *New Journal of Physics*, 16:102001, 2014.

[118] E. A. Cowen and S. G. Monismith. A hybrid digital particle tracking velocimetry technique. *Experiments in Fluids*, 22(3):199–211, 1997.

[119] Matteo Novara, Daniel Schanz, Nico Reuther, Christian J. Kähler, and Andreas Schröder. Lagrangian 3D particle tracking in high-speed flows: Shake-The-Box for multi-pulse systems. *Experiments in Fluids*, 57(8):128, 2016.

[120] Greg A. Voth, A. La Porta, Alice M. Crawford, Jim Alexander, and Eberhard Bodenschatz. Measurement of particle accelerations in fully developed turbulence. *Journal of Fluid Mechanics*, 469:121–160, 2002, 0110027.

[121] I. Grant and X. Pan. An investigation of the performance of multi layer, neural networks applied to the analysis of PIV images. *Experiments in Fluids*, 19(3):159–166, 1995.

[122] G. Labonté. Neural network reconstruction of fluid flows from tracer-particle displacements. *Experiments in Fluids*, 30(4):399–409, 2001.

[123] Shuo Hong Wang, Jingwen Zhao, Xiang Liu, Zhi Ming Qian, Ye Liu, and Yan Qiu Chen. 3D tracking swimming fish school with learned kinematic model using LSTM network. *ICASSP, IEEE International Conference on Acoustics, Speech and Signal Processing - Proceedings*, (July 2018):1068–1072, 2017.

[124] Zhehui Wang, Jiayi Xu, Yao E. Kovach, Bradley T. Wolfe, Edward Thomas, Hanqi Guo, John E. Foster, and Han-Wei Shen. Microparticle cloud imaging and

tracking for data-driven plasma science. *Physics of Plasmas*, 27:033703, 2020, 1911.01000.

[125] Adam A.S. Green, Evan Dutch, Zhiyuan Qi, Corrina Briggs, Cheol S. Park, Matthew A. Glaser, Joseph E. Maclennan, and Noel A. Clark. A gas flow meter with linear sensitivity based on freely-suspended nanofilms of smectic liquid crystal. *Applied Physics Letters*, 114(16), 2019.

[126] Rasmus P. Thomsen, Mette Galsgaard Malle, Anders Hauge Okholm, Swati Krishnan, Søren S.R. Bohr, Rasmus Schøler Sørensen, Oliver Ries, Stefan Vogel, Friedrich C. Simmel, Nikos S. Hatzakis, and Jørgen Kjems. A large size-selective DNA nanopore with sensing applications. *Nature Communications*, 10(1):1–10, 2019.

[127] Jiaqi You, Kevin Mallery, Douglas G. Mashek, Mark Sanders, Jiarong Hong, and Miki Hondzo. Microalgal swimming signatures and neutral lipids production across growth phases. *Biotechnology and Bioengineering*, 117(4), 2020.

[128] Klaus Greff, Rupesh K. Srivastava, Jan Koutnik, Bas R. Steunebrink, and Jurgen Schmidhuber. LSTM: A Search Space Odyssey. *IEEE Transactions on Neural Networks and Learning Systems*, 28(10):2222–2232, 2017, 1503.04069.

[129] Sepp Hochreiter and Jürgen Schmidhuber. Long Short-Term Memory. *Neural Computation*, 9(8):1735–1780, nov 1997.

[130] Ronny Hug, Stefan Becker, Wolfgang Hübner, and Michael Arens. Particle-based Pedestrian Path Prediction using LSTM-MDL Models. *IEEE Conference on Intelligent Transportation Systems, Proceedings, ITSC*, 2018-Novem:2684–2691, 2018, 1804.05546.

[131] Aristeidis Tsaris, Dustin Anderson, Josh Bendavid, Paolo Calafiura, Giuseppe Cerati, Julien Esseiva, Steven Farrell, Lindsey Gray, Keshav Kapoor, Jim Kowalkowski, Mayur Mudigonda, Prabhat, Panagiotis Spentzouris, Maria Spiropoulou, Jean Roch Vlimant, Stephan Zheng, and Daniel Zurawski. The HEP.TrkX Project: Deep Learning for Particle Tracking. *Journal of Physics: Conference Series*, 1085(4), 2018.

[132] Francois and others Chollet. Keras, 2015.

[133] Diederik P. Kingma and Jimmy Ba. Adam: A Method for Stochastic Optimization. *3rd International Conference on Learning Representations, ICLR 2015 - Conference Track Proceedings*, pages 1–15, dec 2014, 1412.6980.

[134] J. Graham, K. Kanov, X. I.A. Yang, M. Lee, N. Malaya, C. C. Lalescu, R. Burns, G. Eyink, A. Szalay, R. D. Moser, and C. Meneveau. A web services accessible database of turbulent channel flow and its use for testing a new integral wall model for LES. *Journal of Turbulence*, 17(2):181–215, 2016.

[135] F. Huhn, D. Schanz, P. Manovski, S. Gesemann, and A. Schröder. Time-resolved large-scale volumetric pressure fields of an impinging jet from dense Lagrangian particle tracking. *Experiments in Fluids*, 59(5):1–16, 2018.

[136] K. Okamoto, S. Nishio, T. Kobayashi, T. Saga, and K. Takehara. Evaluation of the 3D-PIV Standard Images (PIV-STD Project). *Journal of Visualization*, 3(2):115–123, 2000.

[137] Kazuo Ohmi and Hang Yu Li. Particle-tracking velocimetry with new algorithms. *Measurement Science and Technology*, 11(6):603–616, 2000.

[138] Kazuo Ohmi, Sanjeeb Prasad Panday, and Achyut Sapkota. Particle tracking velocimetry with an ant colony optimization algorithm. *Experiments in Fluids*, 48(4):589–605, 2010.

[139] P. Ruhnau, C. Guetter, T. Putze, and C. Schnörr. A variational approach for particle tracking velocimetry. *Measurement Science and Technology*, 16(7):1449–1458, 2005.

[140] Jesse T. Ault, Andrea Fani, Kevin K. Chen, Sangwoo Shin, François Gallaire, and Howard A. Stone. Vortex-Breakdown-Induced Particle Capture in Branching Junctions. *Physical Review Letters*, 117(8):1–5, 2016.

[141] Matteo Novara, Daniel Schanz, Reinhard Geisler, Sebastian Gesemann, Christina Voss, and Andreas Schröder. Multi-exposed recordings for 3D Lagrangian particle

tracking with Multi-Pulse Shake-The-Box. *Experiments in Fluids*, 60(3):1–19, 2019.

[142] Tomoyoshi Shimobaba, Yoshikuni Sato, Junya Miura, Mai Takenouchi, and Tomoyoshi Ito. Real-time digital holographic microscopy using the graphic processing unit. *Optics express*, 16(16):11776–11781, 2008.

[143] Lukas Ahrenberg, Andrew J. Page, Bryan M. Hennelly, John B. McDonald, and Thomas J. Naughton. Using commodity graphics hardware for real-time digital hologram view-reconstruction. *IEEE/OSA Journal of Display Technology*, 5(4):111–119, 2009.

[144] Yasuyuki Ichihashi, Ryutaro Oi, Takanori Senoh, Kenji Yamamoto, and Taiichiro Kurita. Real-time capture and reconstruction system with multiple GPUs for a 3D live scene by a generation from 4K IP images to 8K holograms. *Optics Express*, 20(19):21645, 2012.

[145] S. Bianchi and R. Di Leonardo. Real-time optical micro-manipulation using optimized holograms generated on the GPU. *Computer Physics Communications*, 181(8):1444–1448, 2010, 0907.4027.

[146] Tomoyoshi Shimobaba, Tomoyoshi Ito, Nobuyuki Masuda, Yasuyuki Ichihashi, and Naoki Takada. Fast calculation of computer-generated-hologram on AMD HD5000 series GPU and OpenCL. *Optics express*, 18(10):9955–9960, 2010, 1002.0916.

[147] Jhen-Si Chen, Daping Chu, and Quinn Smithwick. Rapid hologram generation utilizing layer-based approach and graphic rendering for realistic three-dimensional image reconstruction by angular tiling. *Journal of Electronic Imaging*, 23(2):023016, 2014.

[148] L. Orzo, Z. Gorocs, I. Szatmari, and S. Tokes. GPU implementation of volume reconstruction and object detection in Digital Holographic Microscopy. *Cellular Nanoscale Networks and Their Applications (CNNA), 2010 12th International Workshop on*, pages 8–11, 2010.

[149] László Orzó, Zoltán Göröcs, András Fehér, and Szabolcs Tkés. In-line hologram segmentation for volumetric samples. *Applied optics*, 52(1):A45–55, 2013.

[150] Olaf Ronneberger, Philipp Fischer, and Thomas Brox. U-Net: Convolutional Networks for Biomedical Image Segmentation. *arXiv*, 9351:234–241, may 2015, 1505.04597.

[151] Martin Abadi, Ashish Agarwal, Paul Barham, Eugene Brevdo, Zhifeng Chen, Craig Citro, Greg S. Corrado, DavisAndy, Jeffrey Dean, Matthieu Devin, Sanjay Ghemawat, Ian Goodfellow, Andrew Harp, Geoffrey Irving, Michael Isard, Yangqing Jia, Rafal Jozefowicz, Lukasz Kaiser, Manjunath Kudlur, Josh Levenberg, Dandelion Mané, Rajat Monga, Sherry Moore, Derek Murray, Chris Olah, Mike Schuster, Jonathon Shlens, Benoit Steiner, Ilya Sutskever, Kunal Talwar, Paul Tucker, Vincent Vanhoucke, Vijay Vasudevan, Fernanda Viégas, Oriol Vinyals, Pete Warden, Martin Wattenberg, Martin Wicke, Yuan Yu, and Xiaoqiang Zheng. TensorFlow: Large-Scale Machine Learning on Heterogeneous Systems, 2015.

[152] Jiaqi You, Kevin Mallery, Jiarong Hong, and Miki Hondzo. Temperature effects on growth and buoyancy of Microcystis aeruginosa. *Journal of Plankton Research*, 40(1):16–28, 2018.

[153] Klaus D. Jöhnk, Jef Huisman, Jonathan Sharples, Ben Sommeijer, Petra M. Visser, and Jasper M. Stroom. Summer heatwaves promote blooms of harmful cyanobacteria. *Global Change Biology*, 14(3):495–512, 2008.

[154] Jianming Deng, Boqiang Qin, Hans W. Paerl, Yunlin Zhang, Jianrong Ma, and Yuwei Chen. Earlier and warmer springs increase cyanobacterial (Microcystis spp.) blooms in subtropical Lake Taihu, China. *Freshwater Biology*, 59(5):1076–1085, 2014.

[155] Elena Litchman, Paula de Tezanos Pinto, Christopher A. Klausmeier, Mridul K. Thomas, and Kohei Yoshiyama. Linking traits to species diversity and community structure in phytoplankton. *Hydrobiologia*, 653(1):15–28, 2010.

[156] Hans W. Paerl and Jef Huisman. Climate change: A catalyst for global expansion of harmful cyanobacterial blooms. *Environmental Microbiology Reports*, 1(1):27–37, 2009.

[157] J. Alex Elliott. The seasonal sensitivity of Cyanobacteria and other phytoplankton to changes in flushing rate and water temperature. *Global Change Biology*, 16(2):864–876, 2010.

[158] Zhaosheng Chu, Xiangcan Jin, Norio Iwami, and Yuhei Inamori. The effect of temperature on growth characteristics and competitions of Microcystis aeruginosa and Oscillatoria mougeotii in a shallow, eutrophic lake simulator system. *Hydrobiologia*, 581(1):217–223, 2007.

[159] Ming Li, Philip Nti Nkrumah, and Man Xiao. Biochemical composition of Microcystis aeruginosa related to specific growth rate: Insight into the effects of abiotic factors. *Inland Waters*, 4(4):357–362, 2014.

[160] Colin S Reynolds. *The ecology of phytoplankton*. Cambridge University Press, 2006.

[161] Jef Huisman, Jonathan Sharples, Jasper M. Stroom, Petra M. Visser, W. Edwin A. Kardinaal, Jolanda M.H. Verspagen, and Ben Sommeijer. Changes in turbulent mixing shift competition for light between phytoplankton species. *Ecology*, 85(11):2960–2970, 2004.

[162] A. Howard, A. E. Irish, and C. S. Reynolds. A new simulation of cyanobacterial underwater movement (SCUM'96). *Journal of Plankton Research*, 18(8):1375–1385, 1996.

[163] Petra M. Visser, Jutta Passarge, and Luuc R. Mur. Modelling vertical migration of the cyanobacterium Microcystis. *Hydrobiologia*, 349(1-3):99–109, 1997.

[164] Sophie Rabouille, Marie José Salençon, and Jean Marc Thébault. Functional analysis of Microcystis vertical migration: A dynamic model as a prospecting tool. I - Processes analysis. *Ecological Modelling*, 188(2-4):386–403, 2005.

[165] Basak Guven and Alan Howard. Modelling the growth and movement of cyanobacteria in river systems. *Science of the Total Environment*, 368(2-3):898–908, 2006.

[166] Basak Guven and Alan Howard. Sensitivity Analysis of a Cyanobacterial Growth and Movement Model under Two Different Flow Regimes. *Environmental Modeling and Assessment*, 16(6):577–589, 2011.

[167] Samuel Cirés, Lars Wörmer, David Carrasco, and Antonio Quesada. Sedimentation patterns of toxin-producing Microcystis morphospecies in freshwater reservoirs. *Toxins*, 5(5):939–957, 2013.

[168] R. H. Thomas and A. E. Walsby. The effect of temperature on recovery of buoyancy by Microcystis. *Journal of General Microbiology*, 132(6):1665–1672, 1986.

[169] Zhengwen Liu, Donat P. Häder, and Ruben Sommaruga. Occurrence of mycosporine-like amino acids (MAAs) in the bloom-forming cyanobacterium Microcystis aeruginosa. *Journal of Plankton Research*, 26(8):963–966, 2004.

[170] Y. Hong, H. Y. Hu, A. Sakoda, and M. Sagehashi. Effects of allelochemical gramine on photosynthetic pigments of cyanobacterium Microcystis aeruginosa. *World Academy of Science, Engineering and Technology*, 47(11):831–835, 2010.

[171] Jiarong Hong, Siddharth Talapatra, Joseph Katz, Patricia A. Tester, Rebecca J. Waggett, and Allen R. Place. Algal toxins alter copepod feeding behavior. *PLoS ONE*, 7(5):1–10, 2012.

[172] R. L. Panton. *Incompressible flow*. John Wiley & Sons, 2006.

[173] M. D. Rowe, E. J. Anderson, T. T. Wynne, R. P. Stumpf, D. L. Fanslow, K. Kijanka, H. A. Vanderploeg, J. R. Strickler, and T. W. Davis. Vertical distribution of buoyant Microcystis blooms in a Lagrangian particle tracking model for short-term forecasts in Lake Erie. *Journal of Geophysical Research: Oceans*, pages 1–19, 2016.

[174] Laurent Lardon, Arnaud Hélias, Bruno Sialve, Jean Philippe Steyer, and Olivier Bernard. Life-cycle assessment of biodiesel production from microalgae. *Environmental Science and Technology*, 43(17):6475–6481, 2009.

[175] Teresa M. Mata, António A. Martins, and Nidia S. Caetano. Microalgae for biodiesel production and other applications: A review. *Renewable and Sustainable Energy Reviews*, 14(1):217–232, 2010.

[176] F. G. Acién, J. M. Fernández, J. J. Magán, and E. Molina. Production cost of a real microalgae production plant and strategies to reduce it. *Biotechnology Advances*, 30(6):1344–1353, 2012.

[177] Raphael Slade and Ausilio Bauen. Micro-algae cultivation for biofuels: Cost, energy balance, environmental impacts and future prospects. *Biomass and Bioenergy*, 53(0):29–38, 2013.

[178] Arun K. Vuppaladadiyam, Pepijn Prinsen, Abdul Raheem, Rafael Luque, and Ming Zhao. Sustainability Analysis of Microalgae Production Systems: A Review on Resource with Unexploited High-Value Reserves. *Environmental Science and Technology*, 52(24):14031–14049, 2018.

[179] Kanchan Phadwal and P. K. Singh. Effect of nutrient depletion on β-carotene and glycerol accumulation in two strains of Dunaliella sp. *Bioresource Technology*, 90(1):55–58, 2003.

[180] Meng Chen, Haiying Tang, Hongzhi Ma, Thomas C. Holland, K. Y.Simon Ng, and Steven O. Salley. Effect of nutrients on growth and lipid accumulation in the green algae Dunaliella tertiolecta. *Bioresource Technology*, 102(2):1649–1655, 2011.

[181] Jian Gao, Daniel R. Guildenbecher, Phillip L Reu, Varun Kulkarni, Paul E Sojka, and Jun Chen. Quantitative, three-dimensional diagnostics of multiphase drop fragmentation via digital in-line holography. *Optics letters*, 38(11):1893–5, 2013.

[182] Truc Mai, Phuc Nguyen, Trung Vo, Hieu Huynh, Son Tran, Tran Nim, Dat Tran, Hung Nguyen, and Phung Bui. Accumulation of lipid in Dunaliella salina under Nutrient Starvation Condition. *American Journal of Food and Nutrition*, 5(2):58–61, 2017.

[183] Zhehui Wang, Jiayi Xu, Yao E. Kovach, Bradley T. Wolfe, Edward Thomas, Hanqi Guo, John E. Foster, and Han-Wei Shen. Microparticle cloud imaging and tracking for data-driven plasma science. 2019, 1911.01000.

[184] Ahammed Anwar Chengala, Miki Hondzo, Dan Troolin, and Paul a. Lefebvre. Kinetic responses of Dunaliella in moving fluids. *Biotechnology and Bioengineering*, 107(1):65–75, 2010.

[185] Travis J. Hansen, Miki Hondzo, Mara T. Mashek, Douglas G. Mashek, and Paul A. Lefebvre. Algal swimming velocities signal fatty acid accumulation. *Biotechnology and Bioengineering*, 110(1):143–152, 2013.

[186] Dagmar Zweytick, Karin Athenstaedt, and Günther Daum. Intracellular lipid particles of eukaryotic cells. *Biochimica et Biophysica Acta - Reviews on Biomembranes*, 1469(2):101–120, 2000.

[187] Lital Davidi, Adriana Katz, and Uri Pick. Characterization of major lipid droplet proteins from Dunaliella. *Planta*, 236(1):19–33, 2012.

[188] W.J. Bligh, E.G. and Dyer. A rapid method of total lipid extraction and purification. *Canadian Journal of Biochemistry and Physiology*, 37(8), 1959.

[189] F. Alonzo and P. Mayzaud. Spectrofluorometric quantification of neutral and polar lipids in zooplankton using Nile red. *Marine Chemistry*, 67(3-4):289–301, 1999.

[190] Roy D. Sjoblad, Ilan Chet, and Ralph Mitchell. Chemoreception in the green alga Dunaliella tertiolecta. *Current Microbiology*, 1(5):305–307, 1978.

[191] Julius Adler. Chemotaxis in Bacteria. *Science*, 153(3737):708–716, 1966.

[192] Eunjung S. Lee, Alan J. Lewitus, and Richard K. Zimmer. Chemoreception in a marine cryptophyte: Behavioral plasticity in response to amino acids and nitrate. *Limnology and Oceanography*, 44(6):1571–1574, 1999.

[193] Keith E. Cooksey, James B. Guckert, Scott A. Williams, and Patrik R. Callis. Fluorometric determination of the neutral lipid content of microalgal cells using Nile Red. *Journal of Microbiological Methods*, 6(6):333–345, 1987.

[194] Danielle Elsey, David Jameson, Barry Raleigh, and Michael J. Cooney. Fluorescent measurement of microalgal neutral lipids. *Journal of Microbiological Methods*, 68(3):639–642, 2007.

[195] Michael A Borowitzka and Navid R Moheimani, editors. *Algae for Biofuels and Energy*. Springer Netherlands, Dordrecht, 2013.

[196] Ahmad Farhad Talebi, Masoud Tohidfar, Seyedeh Mahsa Mousavi Derazmahalleh, Alawi Sulaiman, Azhari Samsu Baharuddin, and Meisam Tabatabaei. Biochemical modulation of lipid pathway in microalgae Dunaliella sp. for biodiesel production. *BioMed Research International*, 2015, 2015.

[197] Haijian Yang, Qiaoning He, and Chunxiang Hu. Lipid accumulation by NaCl induction at different growth stages and concentrations in photoautotrophic two-step cultivation of monoraphidium dybowskii LB50. *Bioresource Technology*, 187:221–227, 2015.

[198] Laura Barsanti and Paolo Gualtieri. Is exploitation of microalgae economically and energetically sustainable? *Algal Research*, 31:107–115, apr 2018.

[199] Jesús Ruiz, Giuseppe Olivieri, Jeroen De Vree, Rouke Bosma, Philippe Willems, J. Hans Reith, Michel H.M. Eppink, Dorinde M.M. Kleinegris, René H. Wijffels, and Maria J. Barbosa. Towards industrial products from microalgae. *Energy and Environmental Science*, 9(10):3036–3043, 2016.

[200] Stuart A. Scott, Matthew P. Davey, John S. Dennis, Irmtraud Horst, Christopher J. Howe, David J. Lea-Smith, and Alison G. Smith. Biodiesel from algae: Challenges and prospects. *Current Opinion in Biotechnology*, 21(3):277–286, 2010.

[201] Amar Doshi, Sean Pascoe, Louisa Coglan, and Thomas J. Rainey. Economic and policy issues in the production of algae-based biofuels: A review. *Renewable and Sustainable Energy Reviews*, 64:329–337, 2016.

[202] Léda N. Gerber, Jefferson W. Tester, Colin M. Beal, Mark E. Huntley, and Deborah L. Sills. Target Cultivation and Financing Parameters for Sustainable Production of Fuel and Feed from Microalgae. *Environmental Science and Technology*, 50(7):3333–3341, 2016.

[203] Kevin Mallery, Dario Canelon, Jiarong Hong, and Nikos Papanikolopoulos. Robot-Driven Underwater Holographic Microscope for Low-Cost In-Situ Particle Measurements. *arXiv*, 2019, arXiv:1911.10231v1.

[204] David W. Murphy, Cheng Li, Vincent D'Albignac, David Morra, Joseph Katz, Vincent D'Albignac, David Morra, and Joseph Katz. Splash behaviour and oily marine aerosol production by raindrops impacting oil slicks. *Journal of Fluid Mechanics*, 780:536–577, 2015.

[205] Timothy D. Counihan and Stephen M. Bollens. Early detection monitoring for larval dreissenid mussels: how much plankton sampling is enough? *Environmental Monitoring and Assessment*, 189(3), 2017.

[206] James C Kinsey, Dana R Yoerger, Michael V Jakuba, Rich Camilli, Charles R Fisher, and Christopher R German. Assessing the deepwater horizon oil spill with the sentry autonomous underwater vehicle. In *2011 IEEE/RSJ International Conference on Intelligent Robots and Systems*, pages 261–267. IEEE, 2011.

[207] Keiji Natagani, Seiga Kiribayashi, Yoshito Okada, Kazuki Otake, and Kayuza Yoshida. Emergency Response to the Nuclear Accident at the Fukushima Daiichi Nuclear Power Plants using Mobile Rescue Robots. *IFAC Proc. Vol.*, 7(PART 1):81–86, 2007.

[208] Patrick P Neumann, Sahar Asadi, Achim J Lilienthal, Matthias Bartholmai, and Jochen H Schiller. Autonomous gas-sensitive microdrone: Wind vector estimation and gas distribution mapping. *IEEE Robotics and Automation Magazine*, 2012.

[209] Dianne I Greenfield, Roman Marin, Gregory J Doucette, Christina Mikulski, Kelly Jones, Scott Jensen, Brent Roman, Nilo Alvarado, Jason Feldman, and Chris Scholin. Field applications of the second-generation Environmental Sample Processor (ESP) for remote detection of harmful algae: 2006-2007. *Limnology and Oceanography: Methods*, 6(12):667–679, 2008.

[210] J. Katz, P. L. Donaghay, J. Zhang, S. King, and K. Russell. Submersible holocamera for detection of particle characteristics and motions in the ocean. *Deep-Sea Research Part I: Oceanographic Research Papers*, 46(8):1455–1481, 1999.

[211] John Watson, S Alexander, G Craig, D C Hendry, P R Hobson, R S Lampitt, J M Marteau, H Nareid, M A Player, and K Saw. Simultaneous in-line and off-axis subsea holographic recording of plankton and other marine particles. *Measurement Science and Technology*, 12:L9—-L15, 2001.

[212] John Watson. Submersible digital holographic cameras and their application to marine science. *Optical Engineering*, 50(9):091313, 2011.

[213] A B Bochdansky, M H Jericho, and G J Herndl. Development and deployment of a point-source digital inline holographic microscope for the study of plankton and particles to a depth of 6000 m. *Limnology and Oceanography: Methods*, 11(JAN):28–40, 2013.

[214] Jian Sheng, Edwin Malkiel, Joseph Katz, Jason Adolf, Robert Belas, and Allen R Place. Digital holographic microscopy reveals prey-induced changes in swimming behavior of predatory dinoflagellates. *Proceedings of the National Academy of Sciences of the United States of America*, 104(44):17512–17517, 2007.

[215] Andrew Howard, Mark Sandler, Grace Chu, Liang-chieh Chen, Bo Chen, Mingxing Tan, Weijun Wang, Yukun Zhu, Ruoming Pang, Vijay Vasudevan, Quoc V Le, and Hartwig Adam. Searching for MobileNetV3. *International Conference on Computer Vision*, pages 1314–1324, 2019.

[216] Sandeep Dhull, Dario Canelon, Apostolos Kottas, Justin Dancs, Andrew Carlson, and Nikolaos Papanikolopoulos. Aquapod: A small amphibious robot with sampling capabilities. In *IEEE International Conference on Intelligent Robots and Systems*, 2012.

[217] W K Fales, D W Amick, and B G Schreiner. The Riverine Utility Craft (RUC). *Journal of Terramechanics*, 8(3):23–38, 1972.

[218] Applied Mechanics Group and B N Cole. Inquiry into amphibious screw traction. *Proceedings of the Institution of Mechanical Engineers*, 175(1):919–940, 1961.

[219] Howard Dugoff and I Robert Ehlich. Model tests of bouyant screw rotor configurations. *Journal of Terramechanics*, 4(3):9–22, 1967.

[220] Trung-Dung Dang, Young Ho Kim, Hwan Gon Kim, and Gyu Man Kim. Preparation of monodisperse PEG hydrogel microparticles using a microfluidic flow-focusing device. *Journal of Industrial and Engineering Chemistry*, 18(4):1308–1313, 2012.

[221] Siyao Shao, Kevin Mallery, Santosh Kumar, and Jiarong Hong. Machine Learning Holography for 3D Particle Field Imaging. *Optics Express*, 28(3):2987–2999, 2020, 1911.00805.

[222] Sima Asadi, Nicole Bouvier, Anthony S. Wexler, and William D. Ristenpart. The coronavirus pandemic and aerosols: Does COVID-19 transmit via expiratory particles? *Aerosol Science and Technology*, 54(6):1–4, 2020.

[223] Yuan Liu, Zhi Ning, Yu Chen, Ming Guo, Yingle Liu, Nirmal Kumar Gali, Li Sun, Yusen Duan, Jing Cai, Dane Westerdahl, Xinjin Liu, Ke Xu, Kin-fai Ho, Haidong Kan, Qingyan Fu, and Ke Lan. Aerodynamic analysis of SARS-CoV-2 in two Wuhan hospitals. *Nature*, apr 2020.